



US 20250263855A1

(19) United States

(12) Patent Application Publication

Muhich et al.

(10) Pub. No.: US 2025/0263855 A1

(43) Pub. Date: Aug. 21, 2025

(54) SOLAR THERMOCHEMICAL FUEL PRODUCTION SYSTEM AND METHODS OF USE THEREOF

(71) Applicant: ARIZONA BOARD OF REGENTS ON BEHALF OF ARIZONA STATE UNIVERSITY, Scottsdale, AZ (US)

(72) Inventors: Christopher Muhich, Phoenix, AZ (US); Jayni Hashimoto, Tempe, AZ (US)

(21) Appl. No.: 19/056,619

(22) Filed: Feb. 18, 2025

Related U.S. Application Data

(60) Provisional application No. 63/554,702, filed on Feb. 16, 2024.

Publication Classification

(51) Int. Cl.

C25B 11/077 (2021.01)

C25B 1/02 (2006.01)

C25B 1/23 (2021.01)

C25B 9/09 (2021.01)

C25B 9/70 (2021.01)

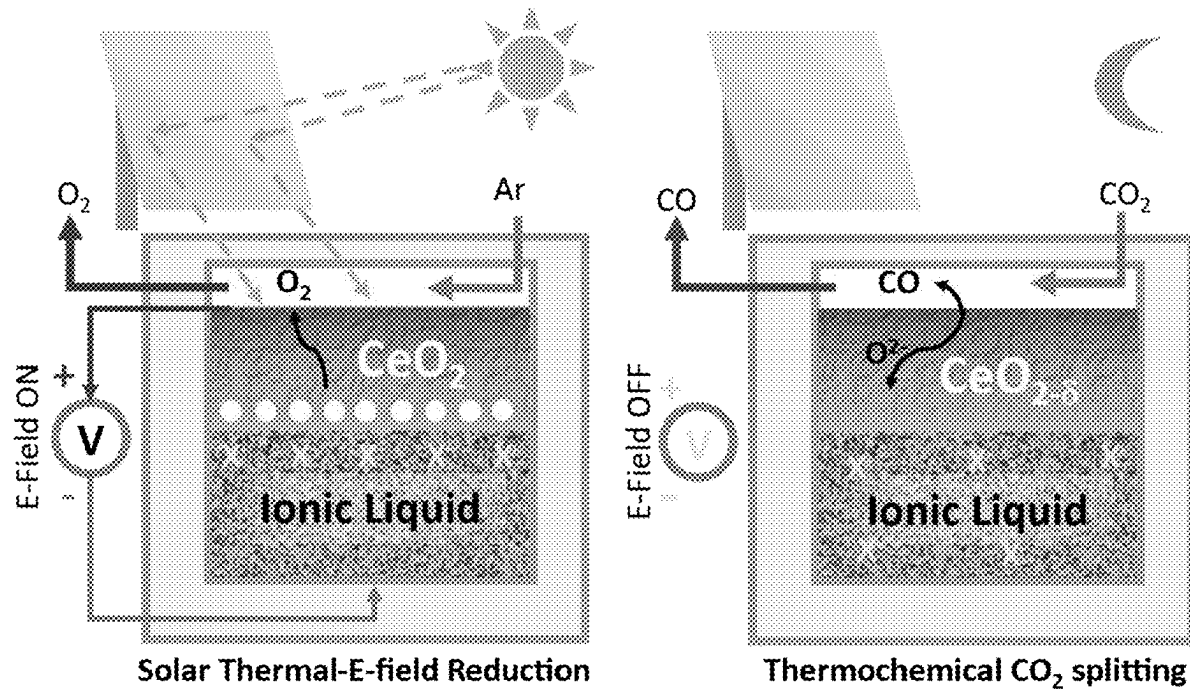
(52) U.S. Cl.

CPC C25B 11/077 (2021.01); C25B 1/02 (2013.01); C25B 1/23 (2021.01); C25B 9/09 (2021.01); C25B 9/70 (2021.01)

(57)

ABSTRACT

The invention relates to solar thermochemical fuel production systems and methods of use thereof.



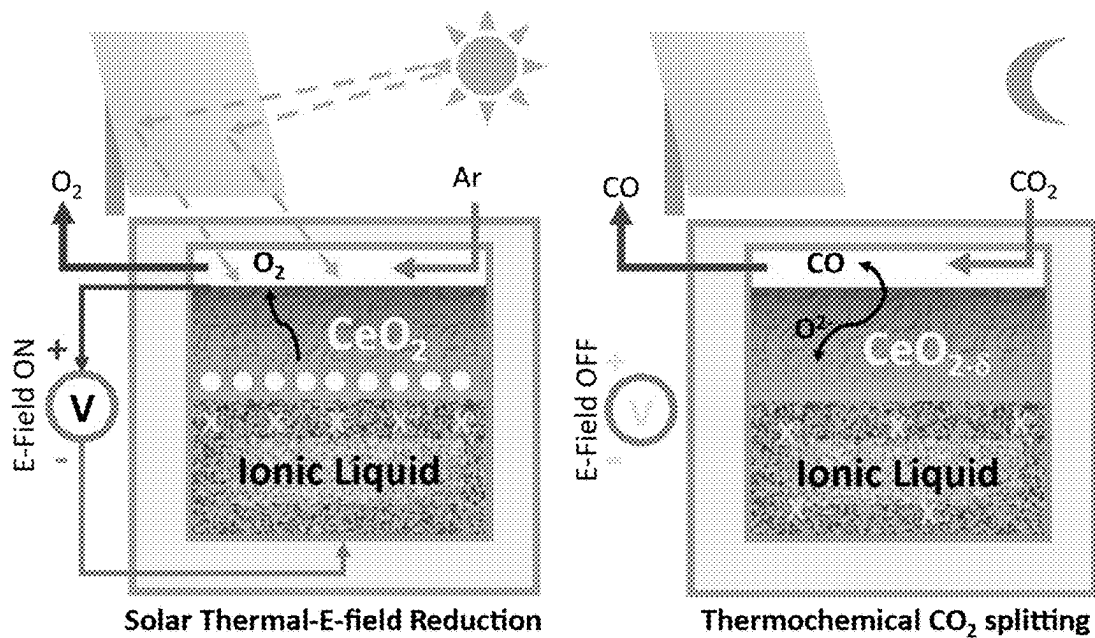


FIG. 1

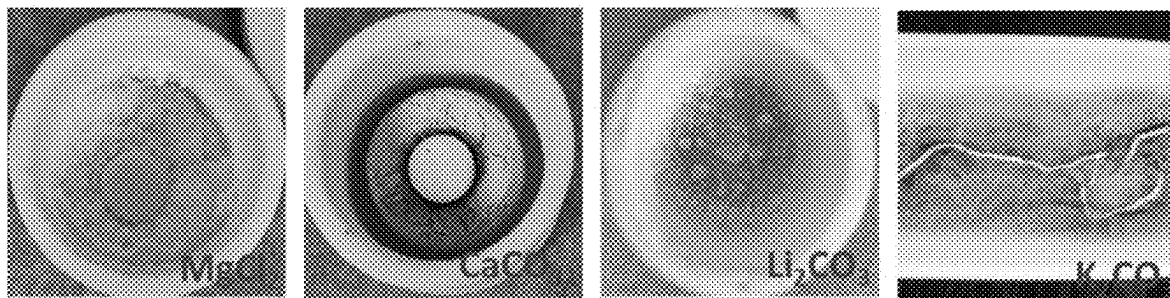


FIG. 2

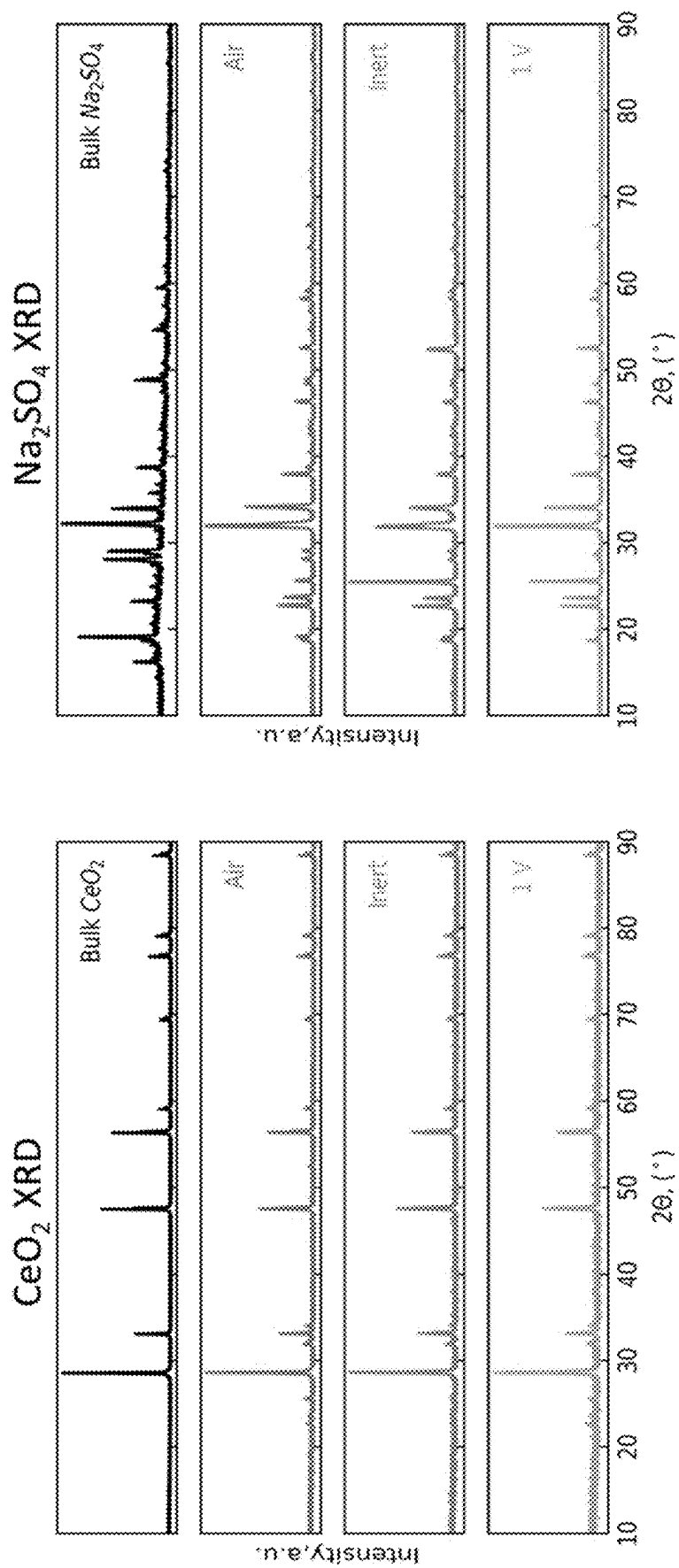


FIG. 3

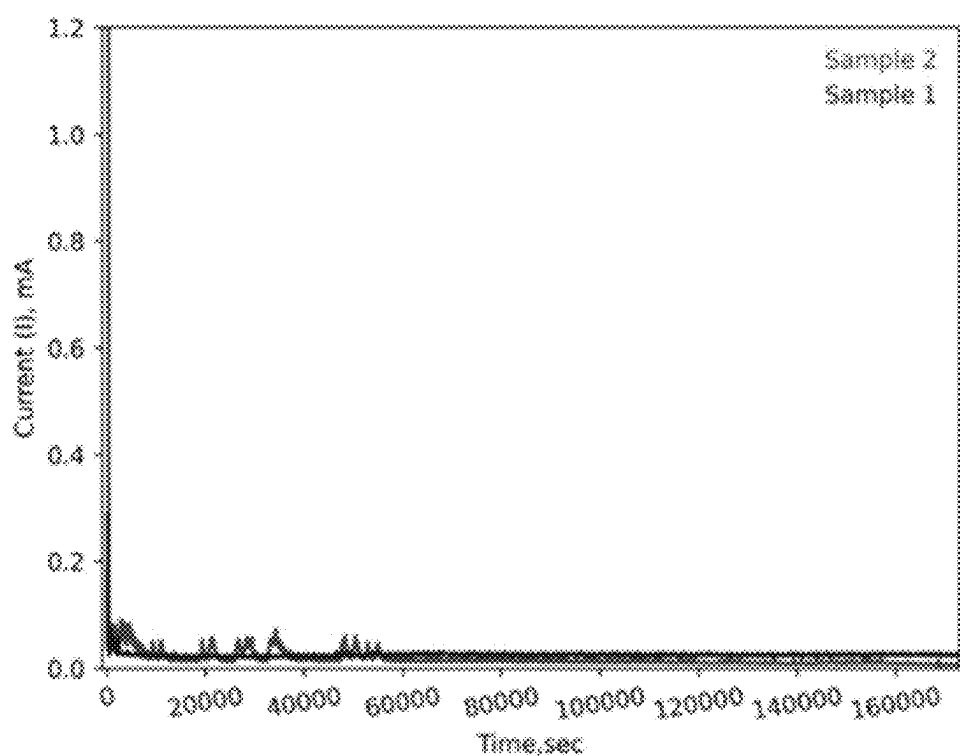
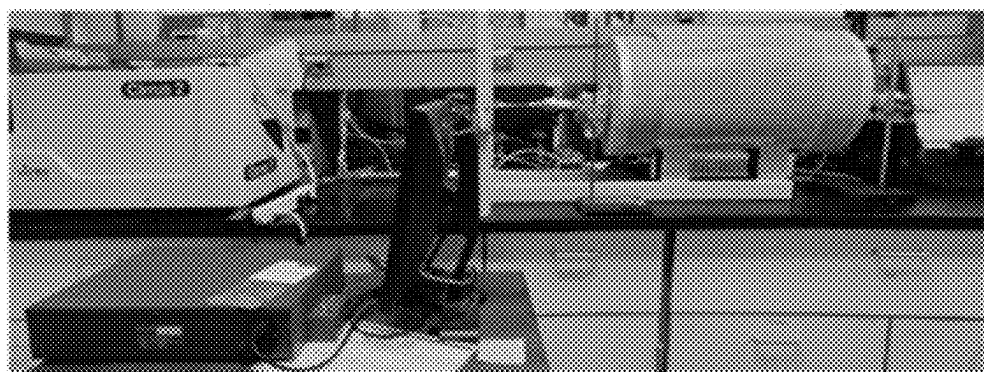
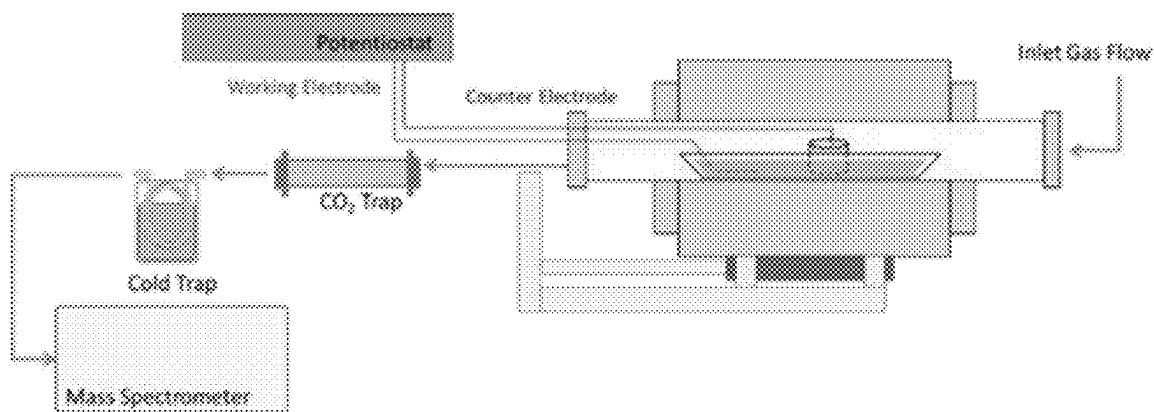


FIG. 4

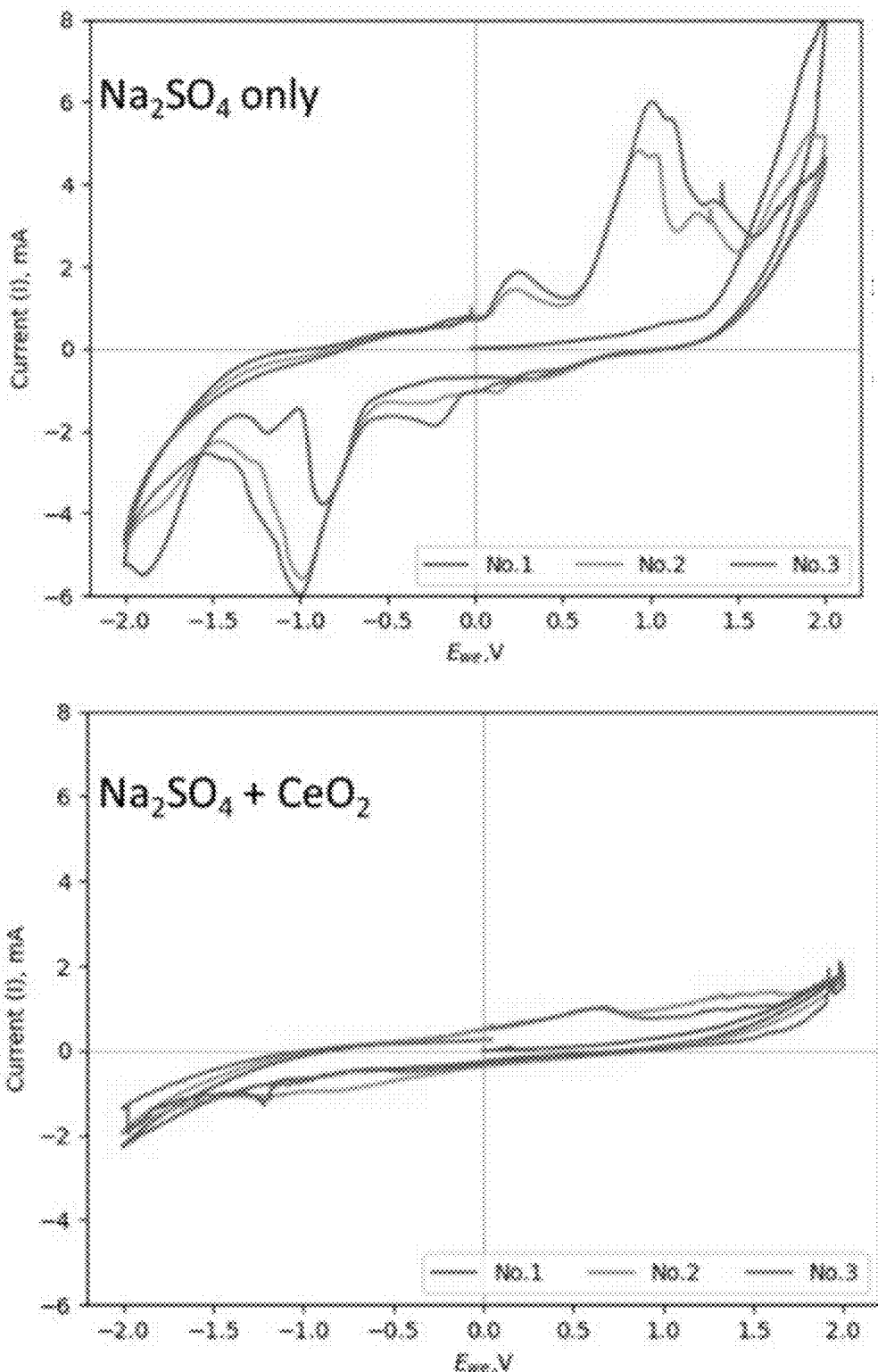


FIG. 5

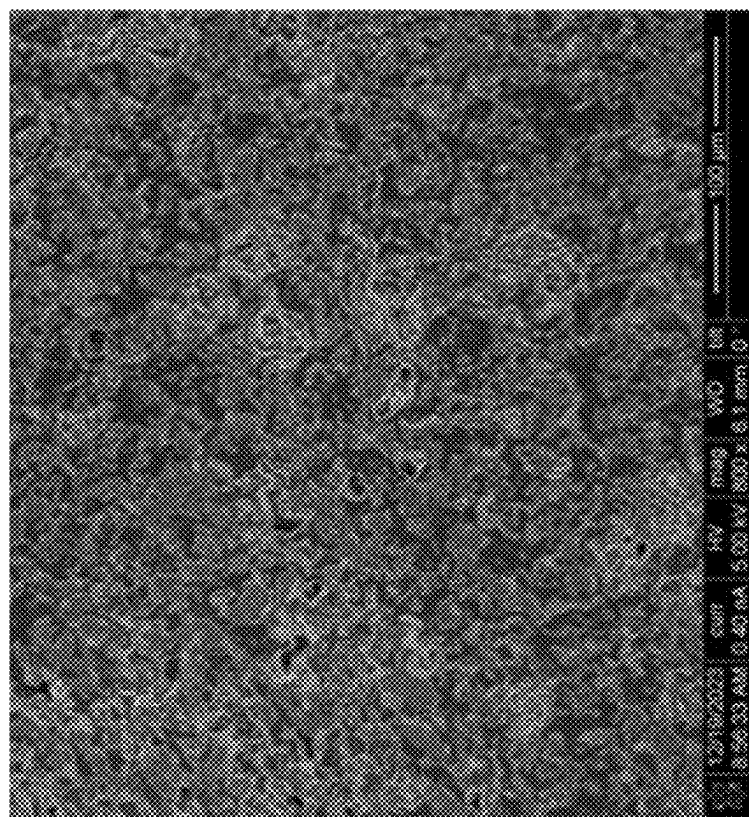
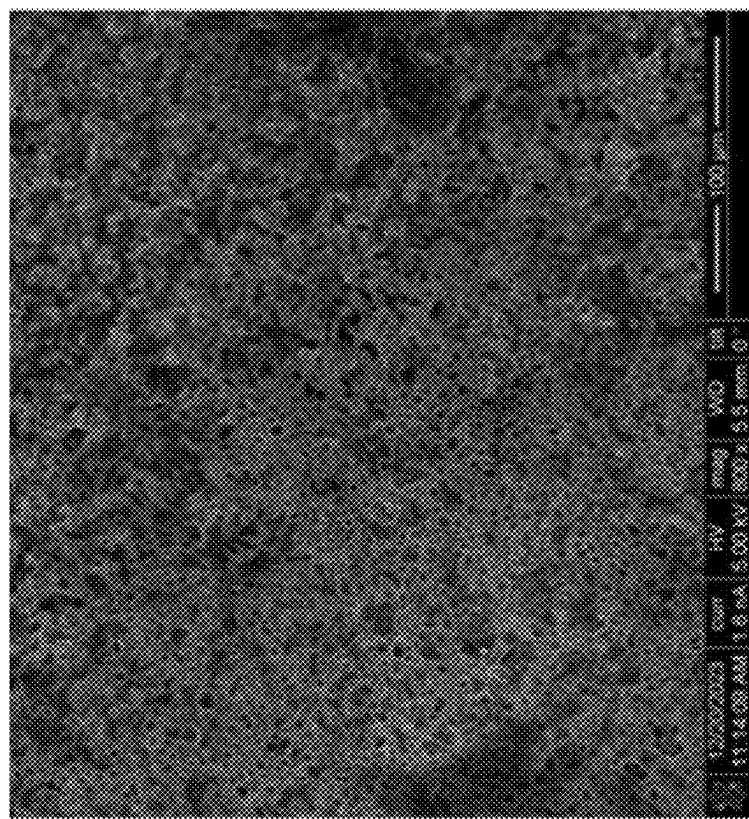


FIG. 6

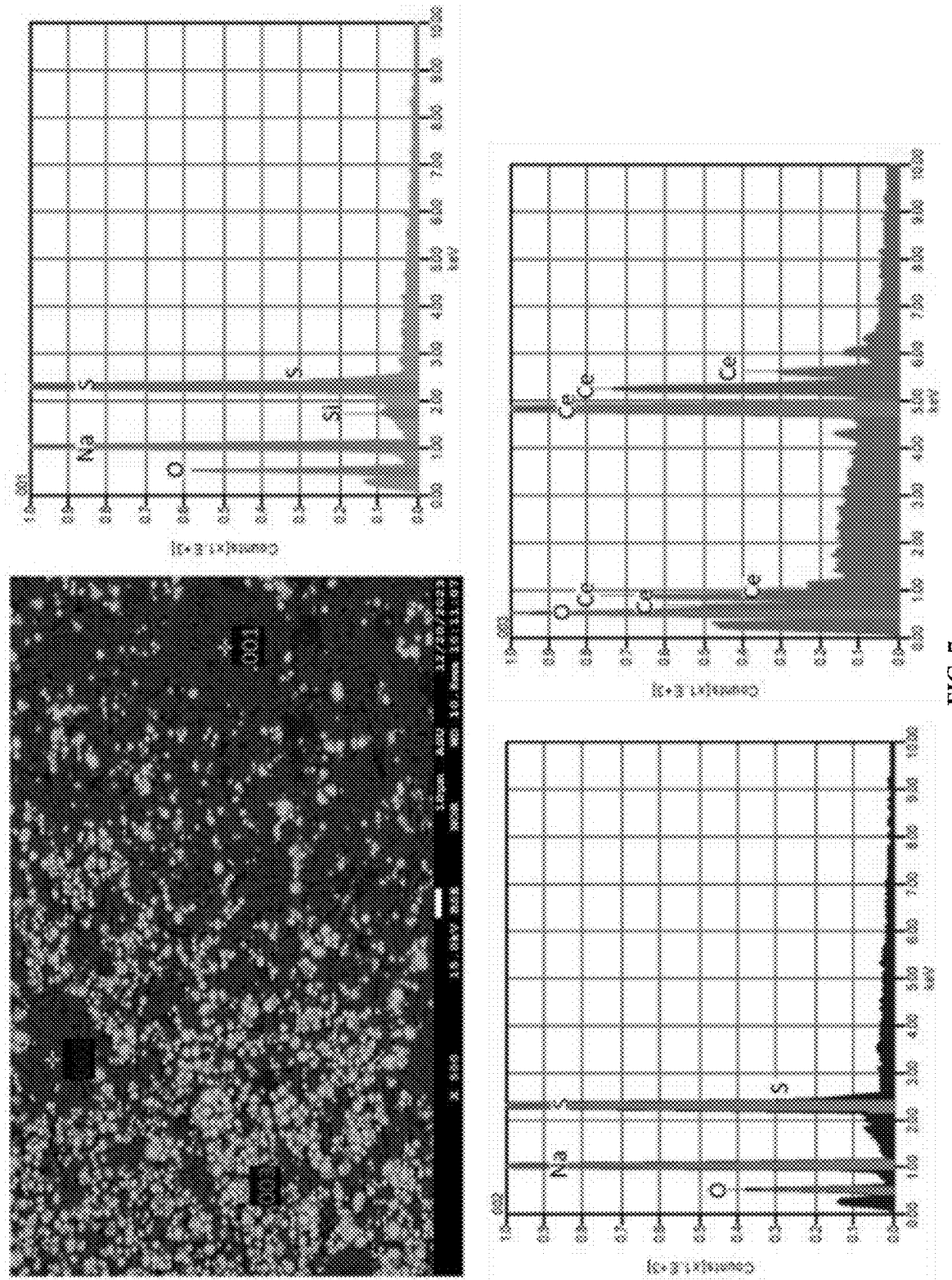


FIG. 7

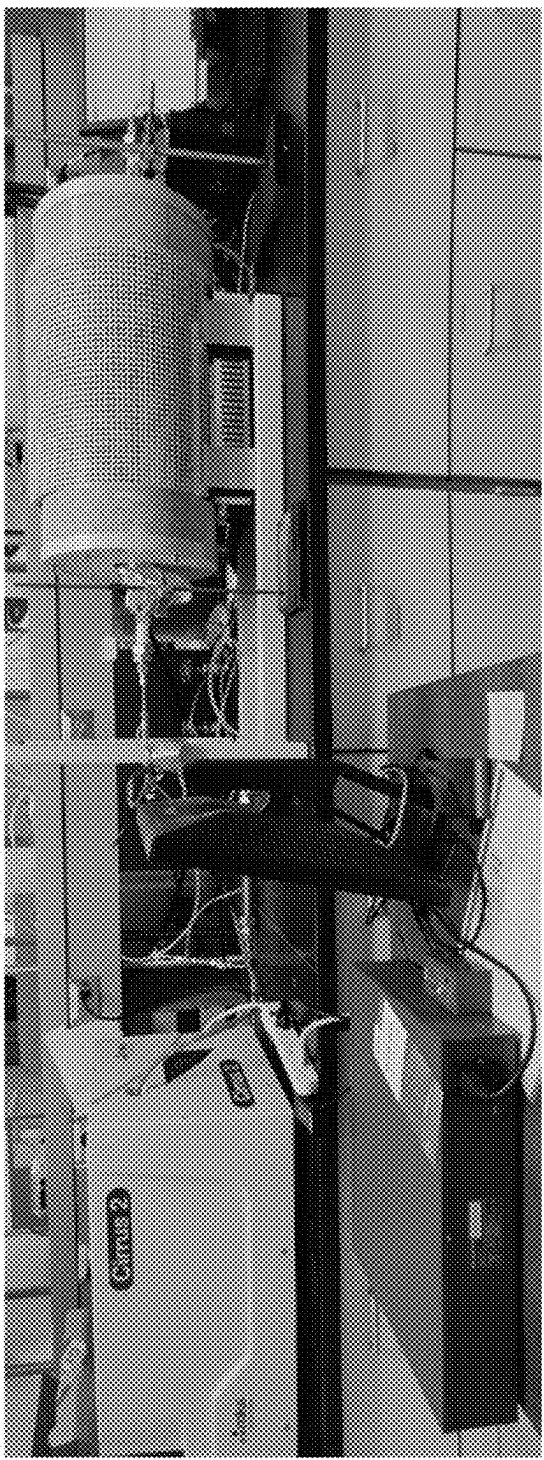
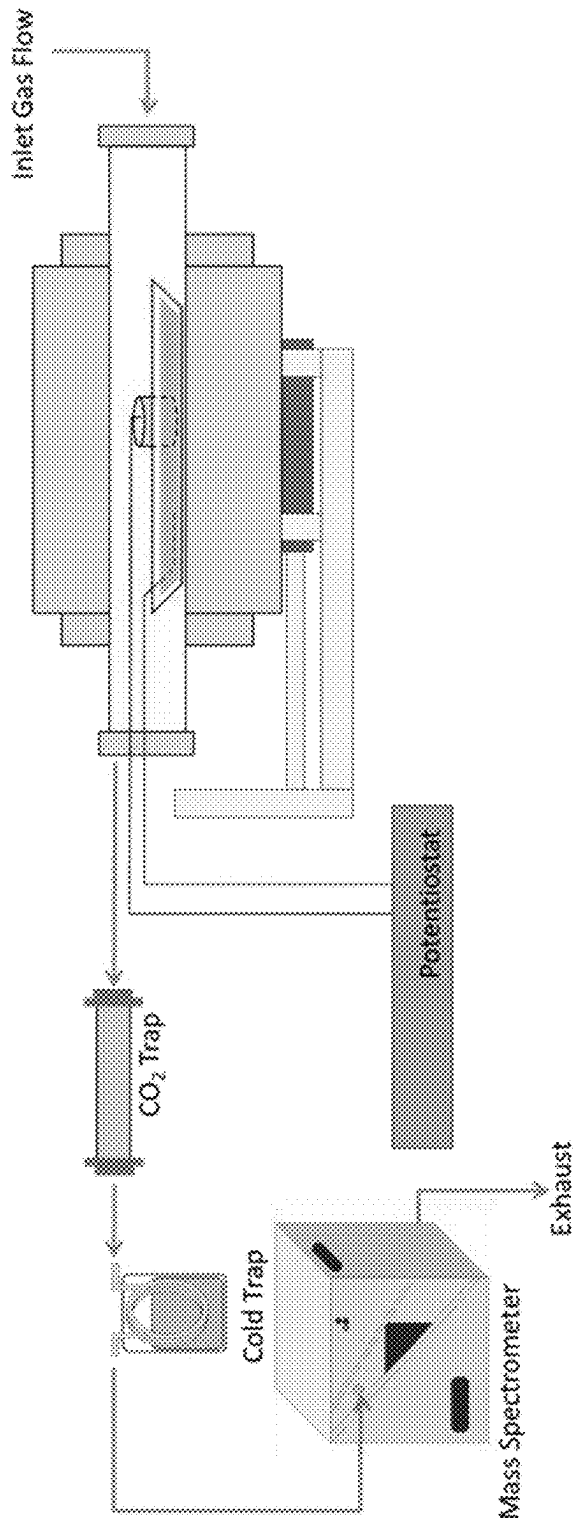


FIG. 8

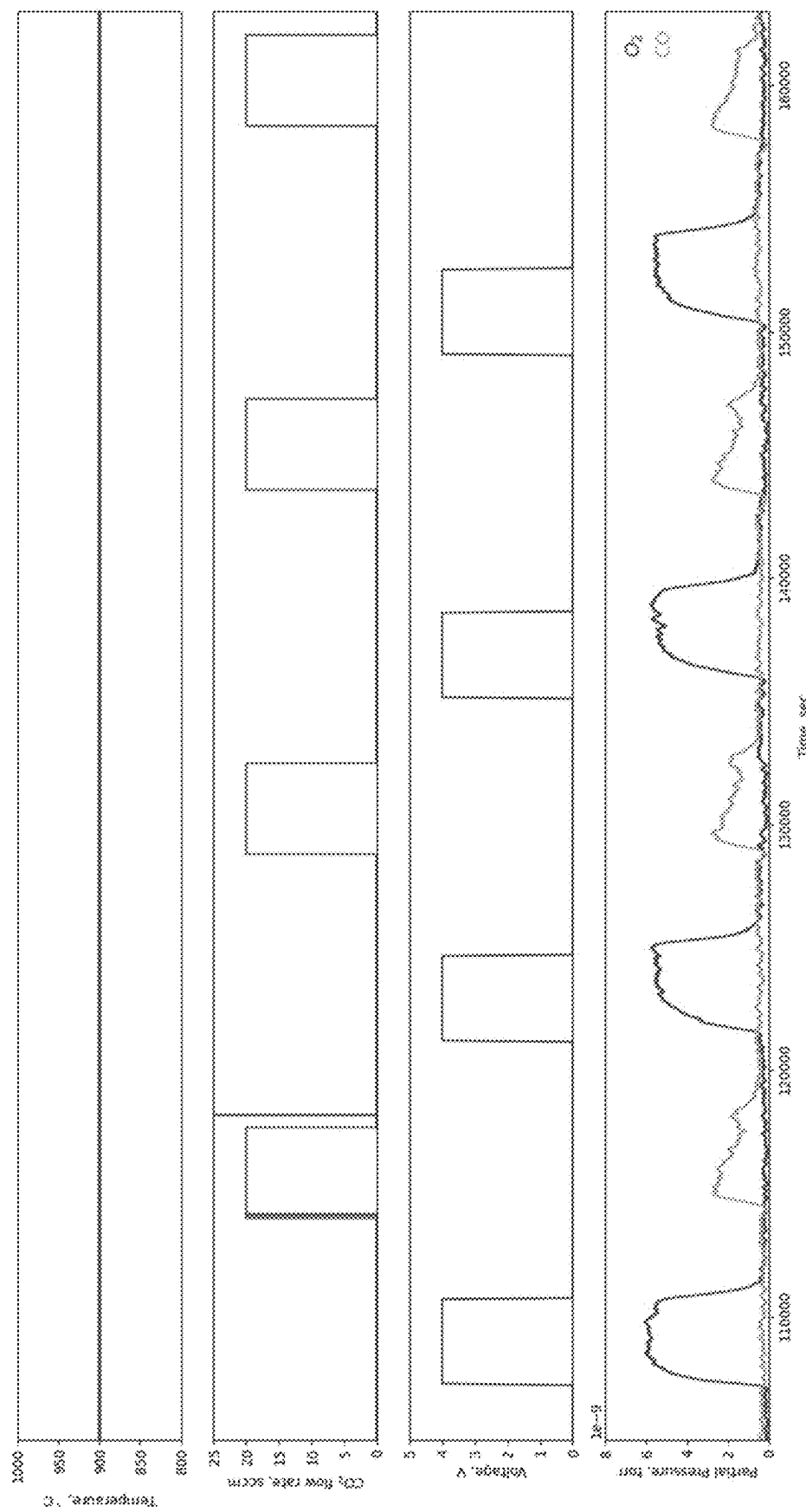


FIG. 9

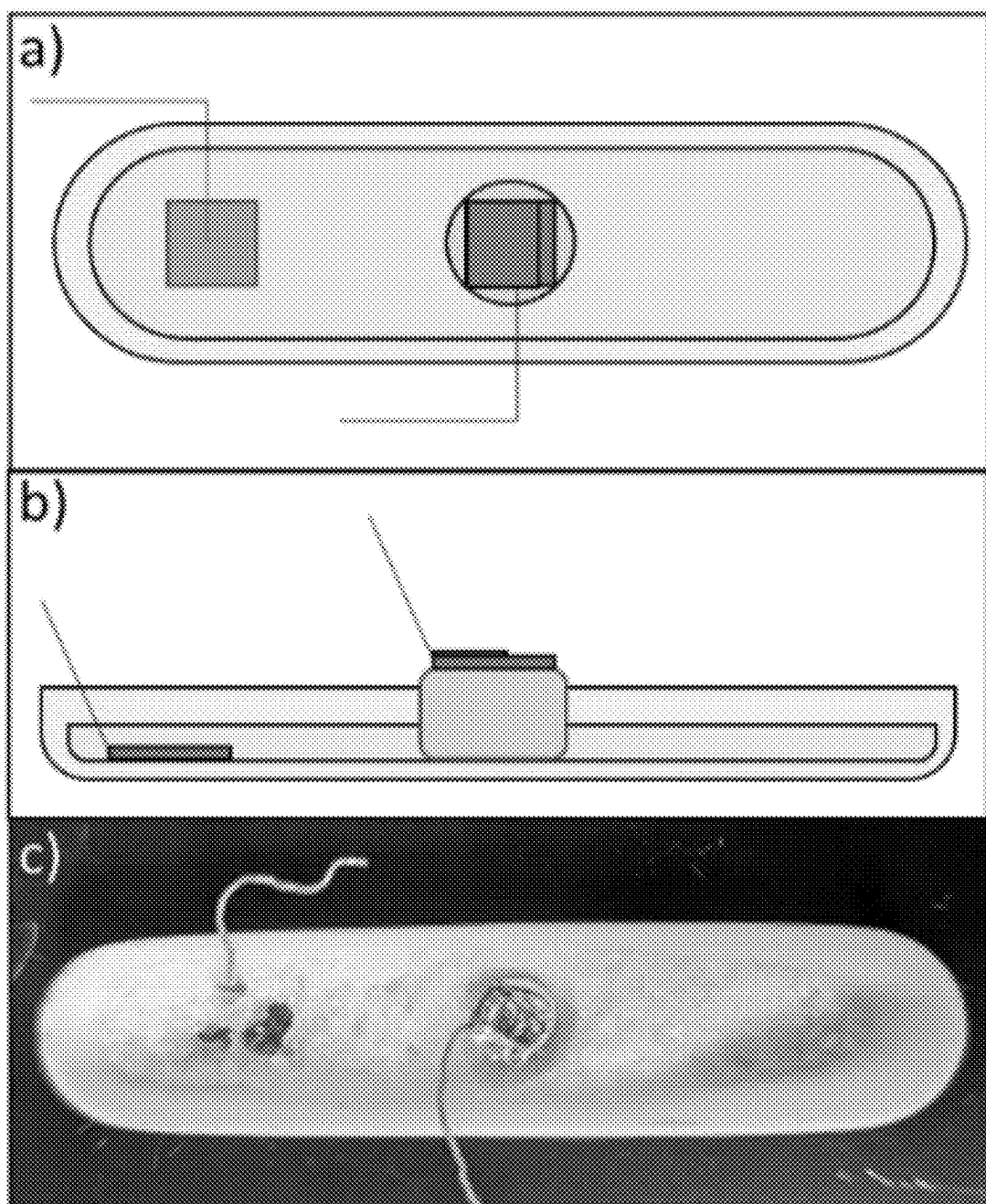


FIG. 10

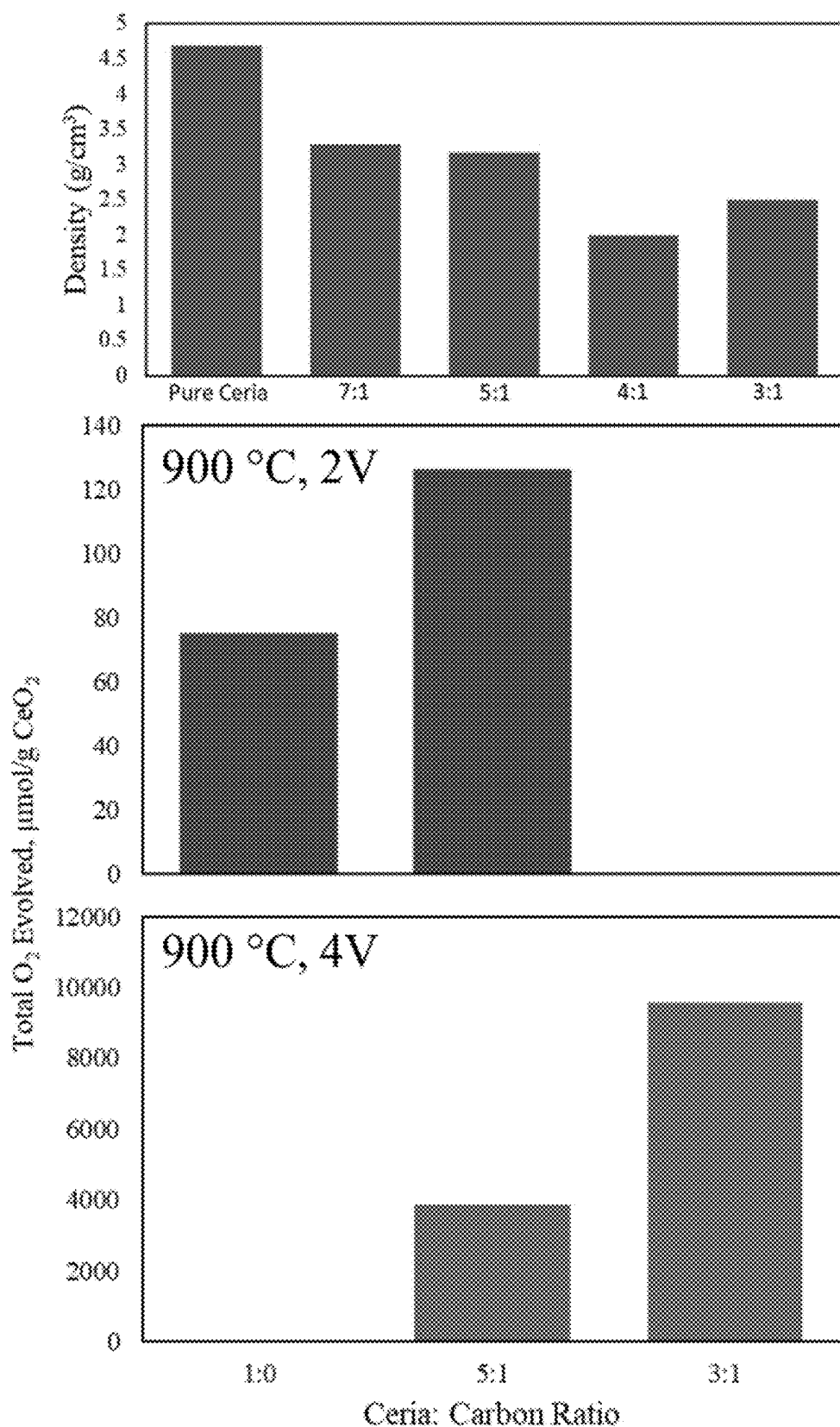


FIG. 11

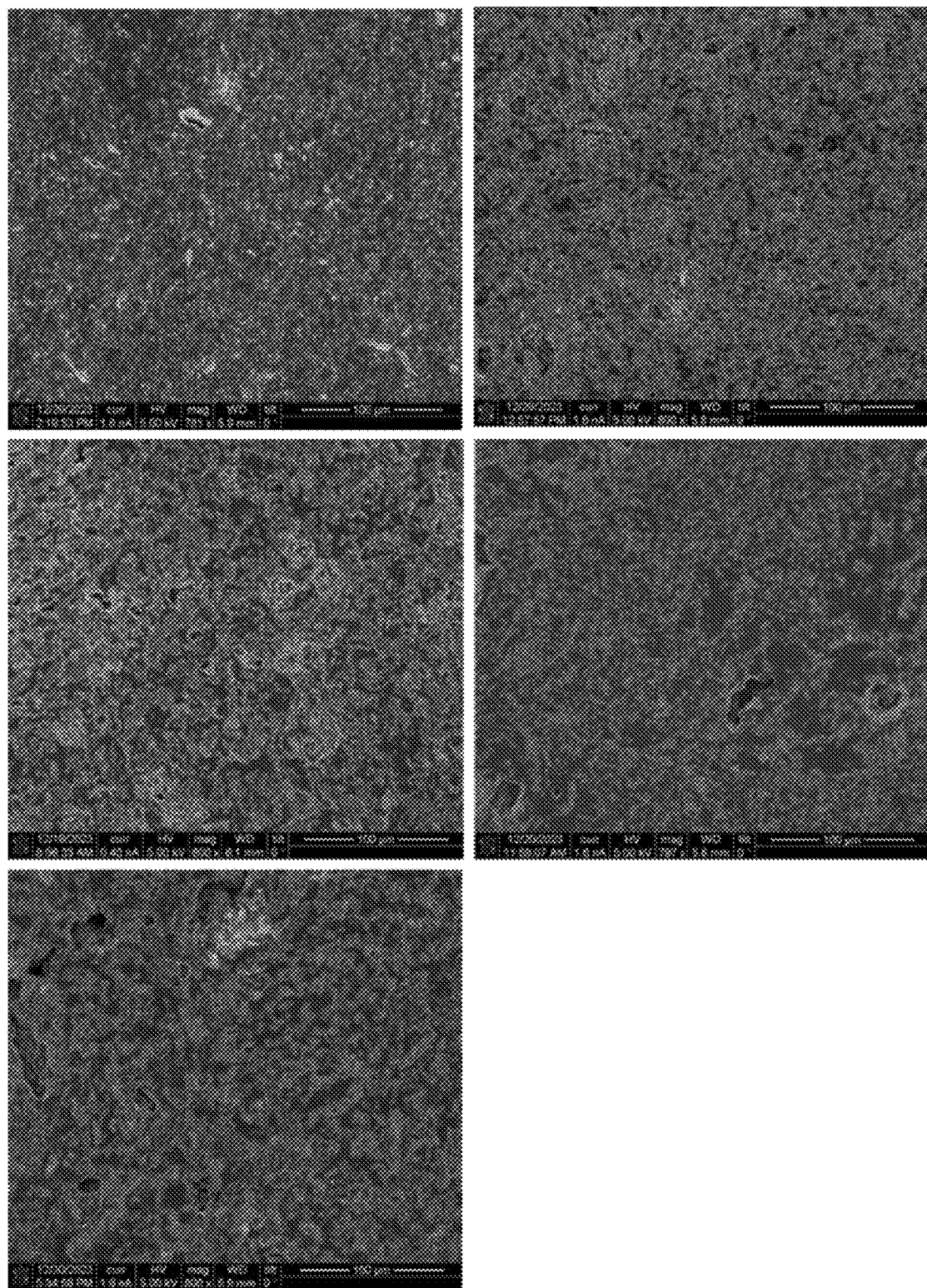


FIG. 12

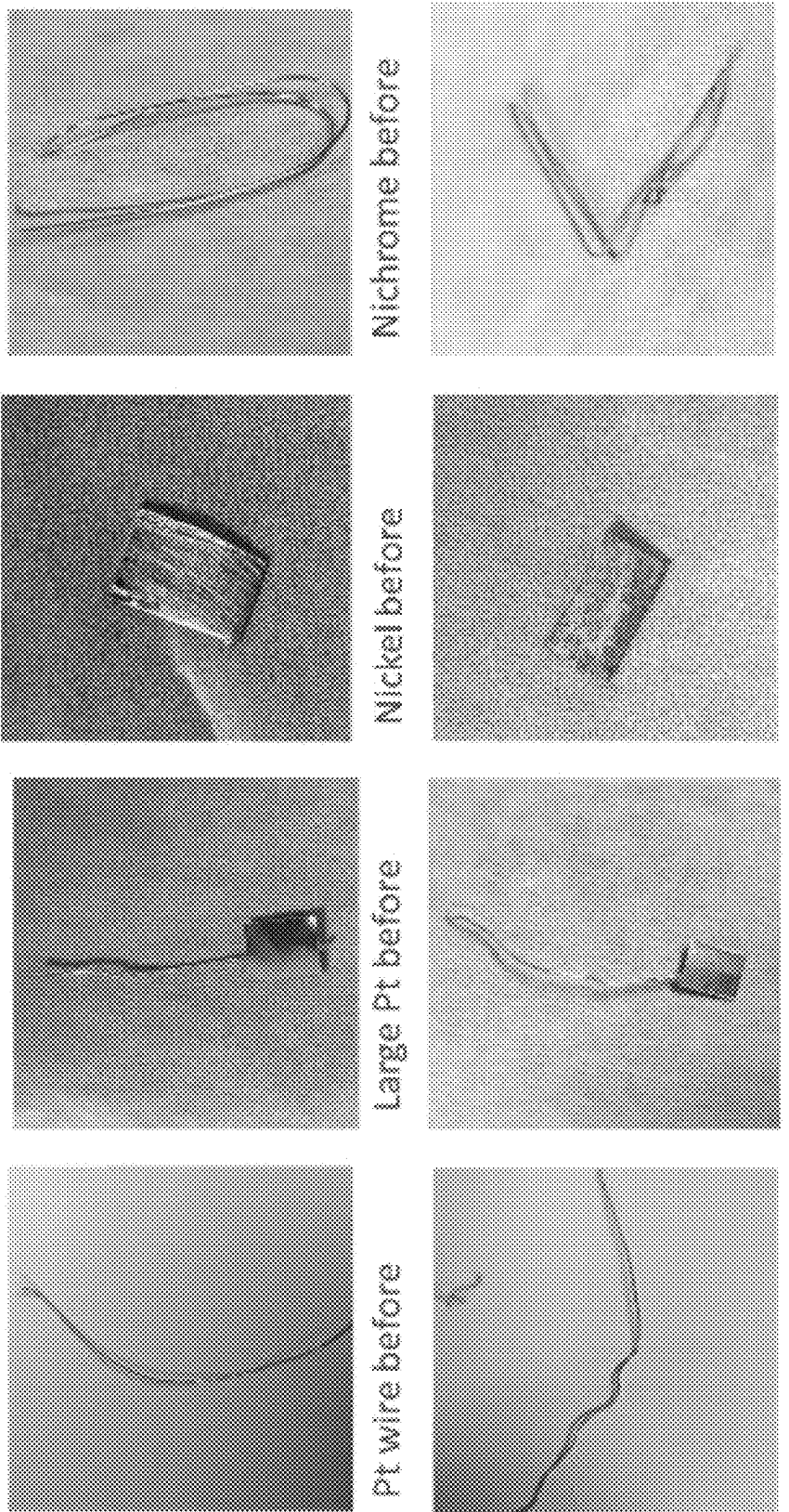


FIG. 13

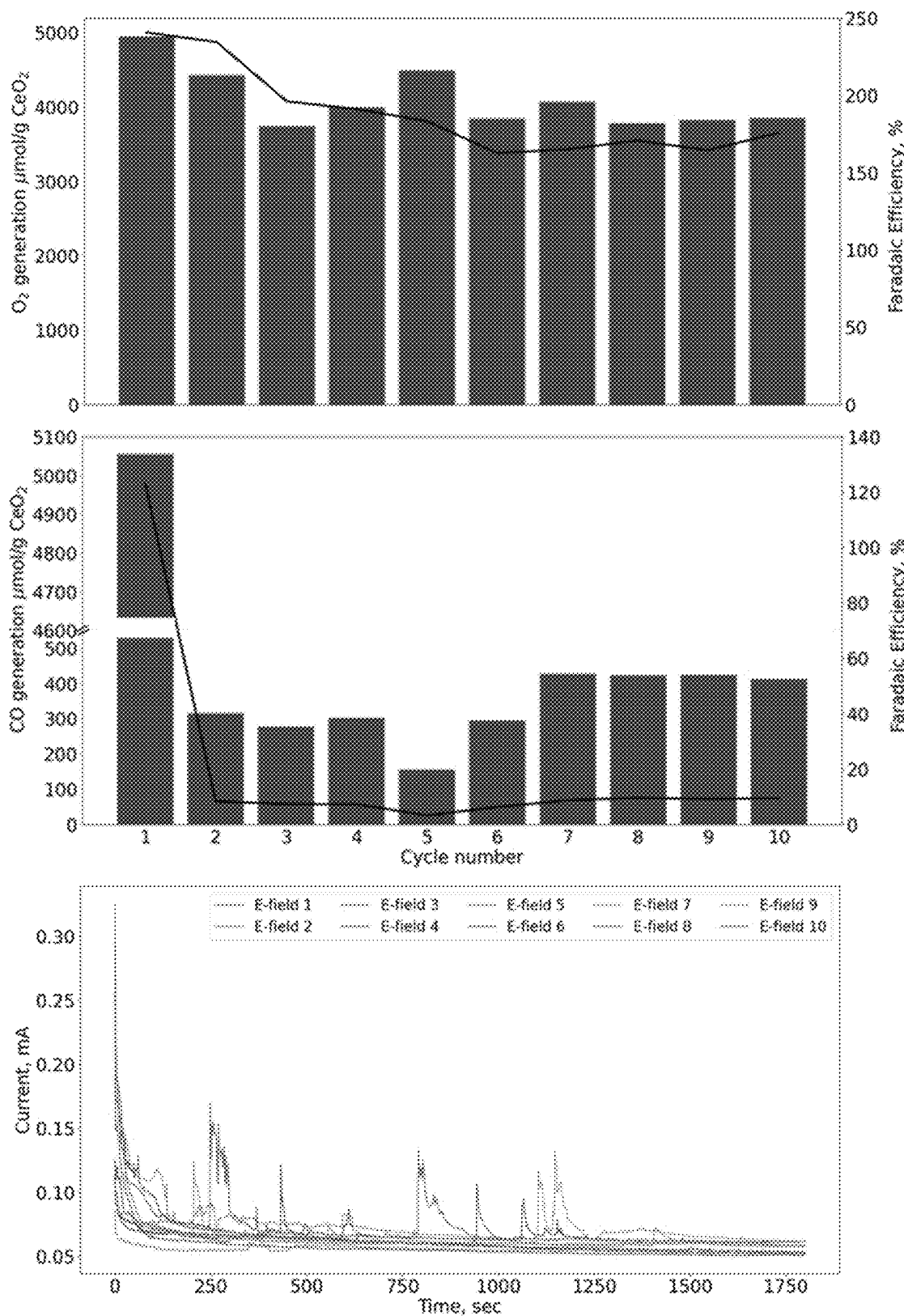


FIG. 14

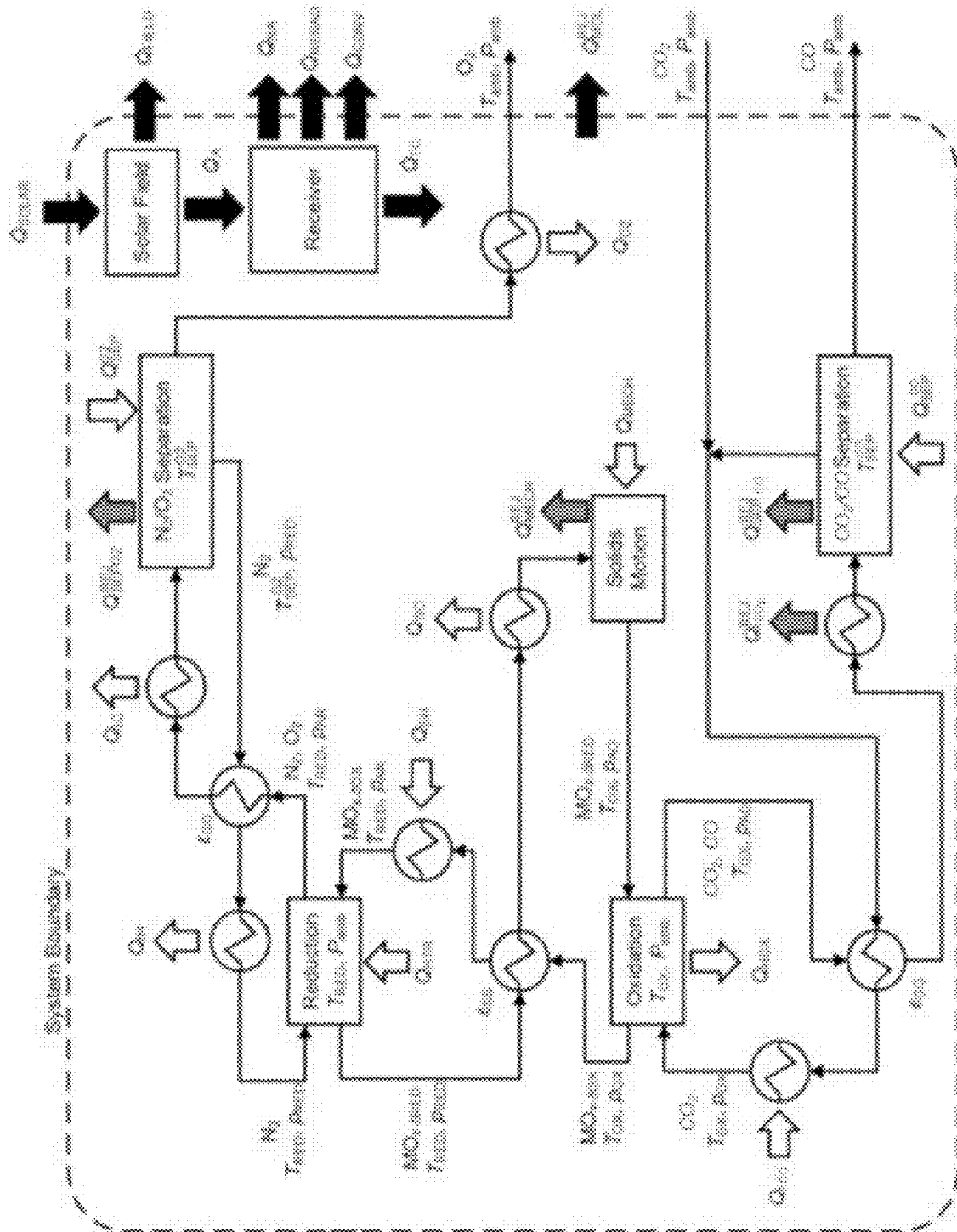


FIG. 15

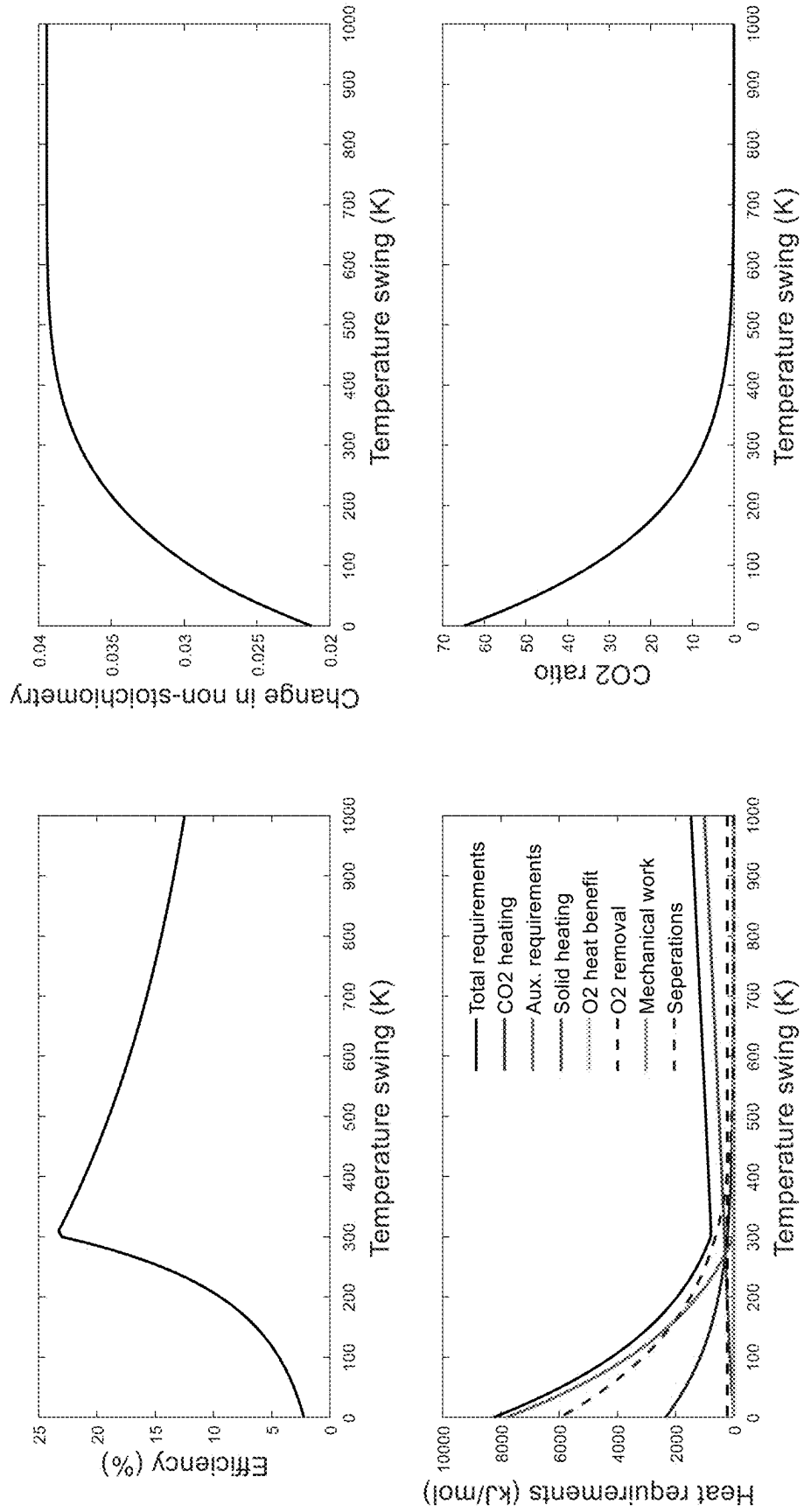


FIG. 16

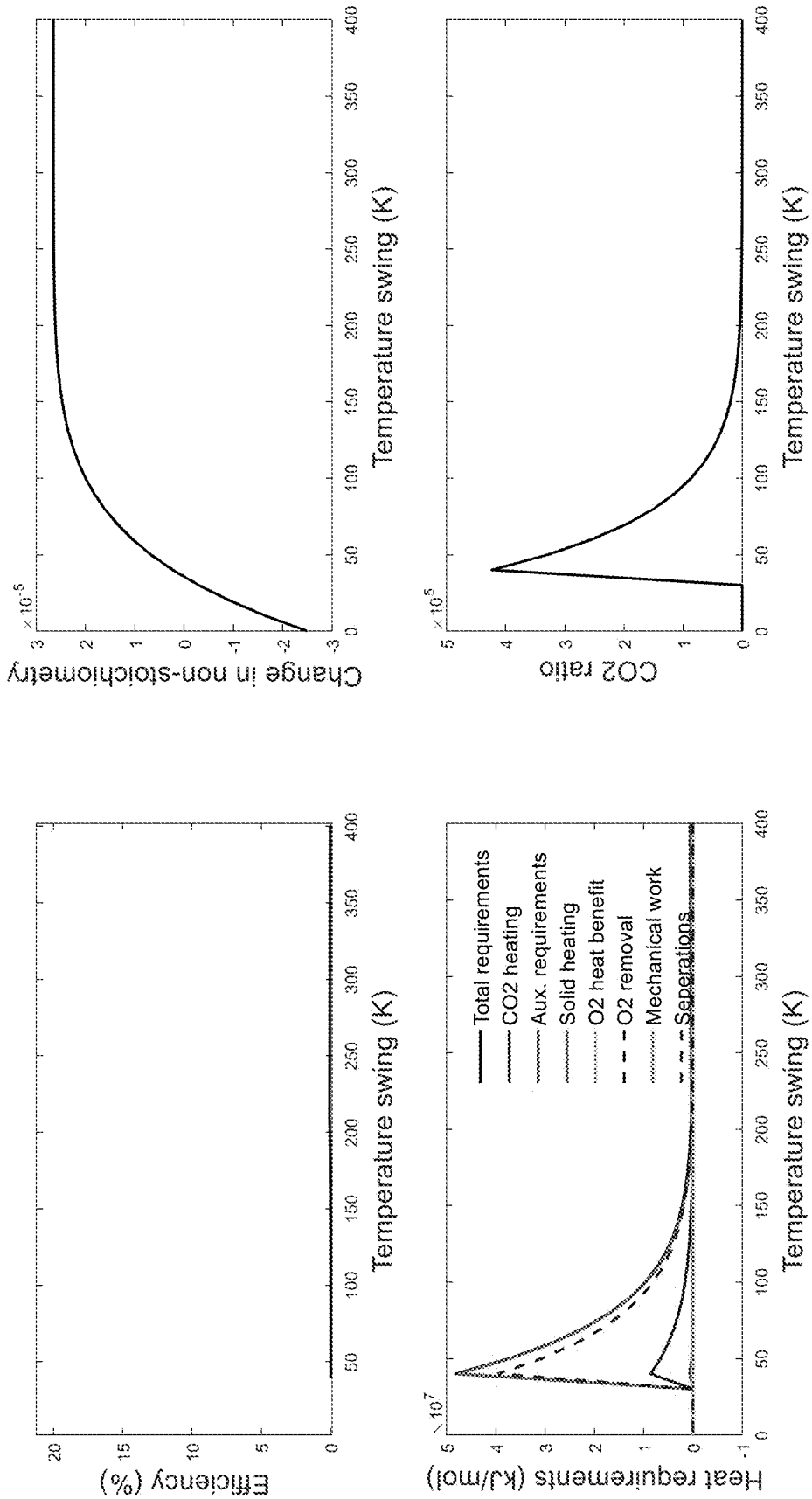


FIG. 17

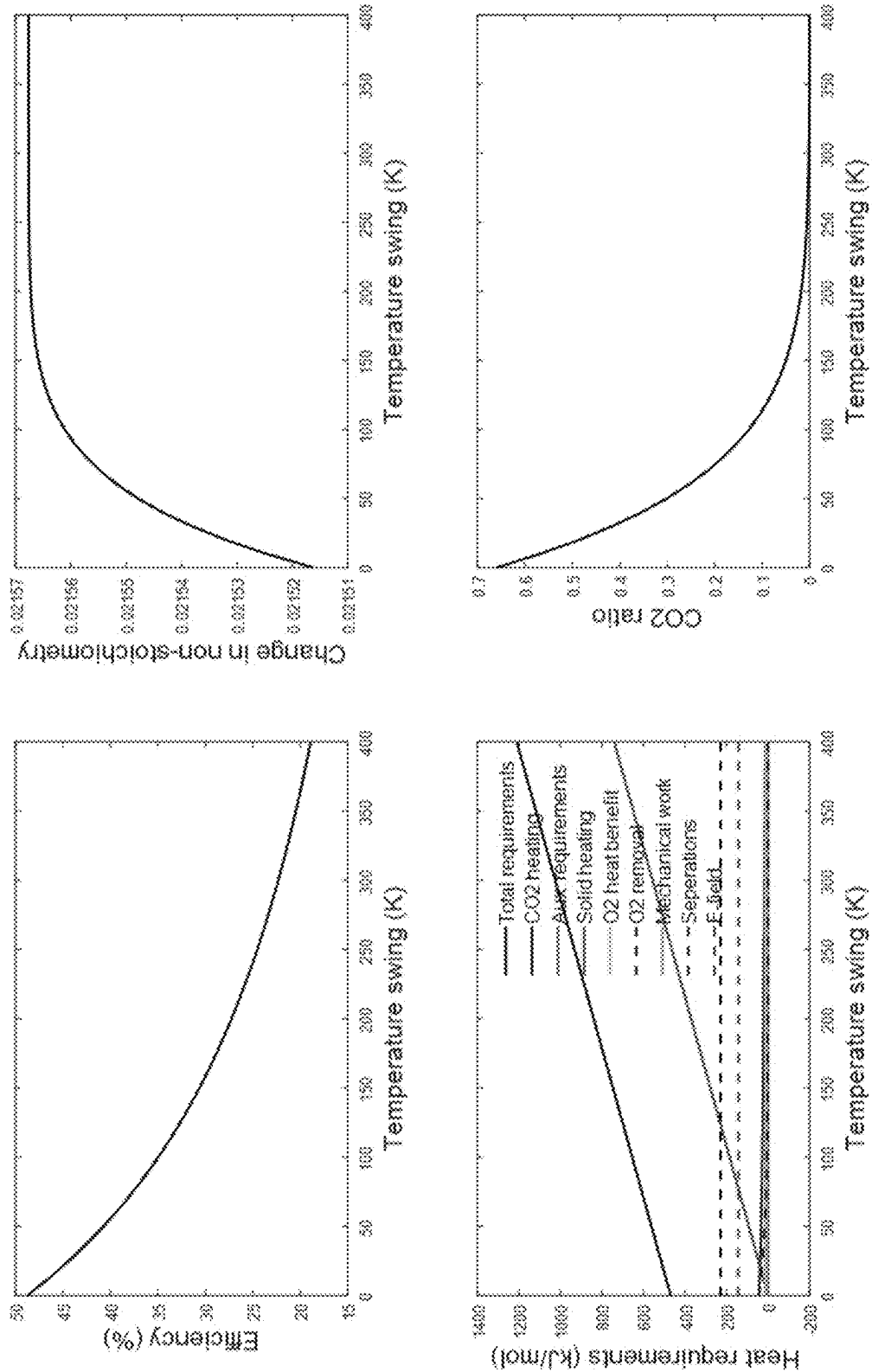


FIG. 18

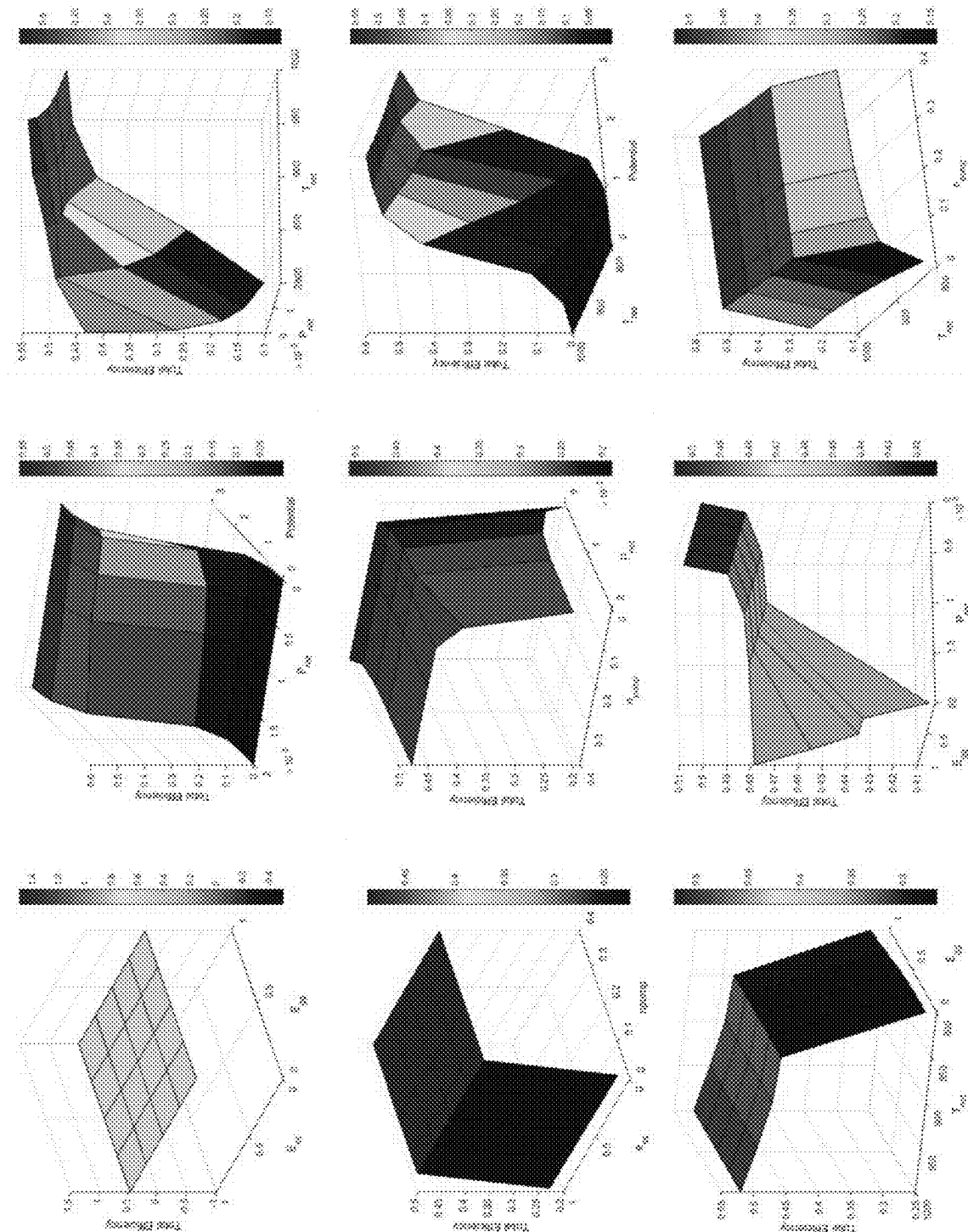


FIG. 19

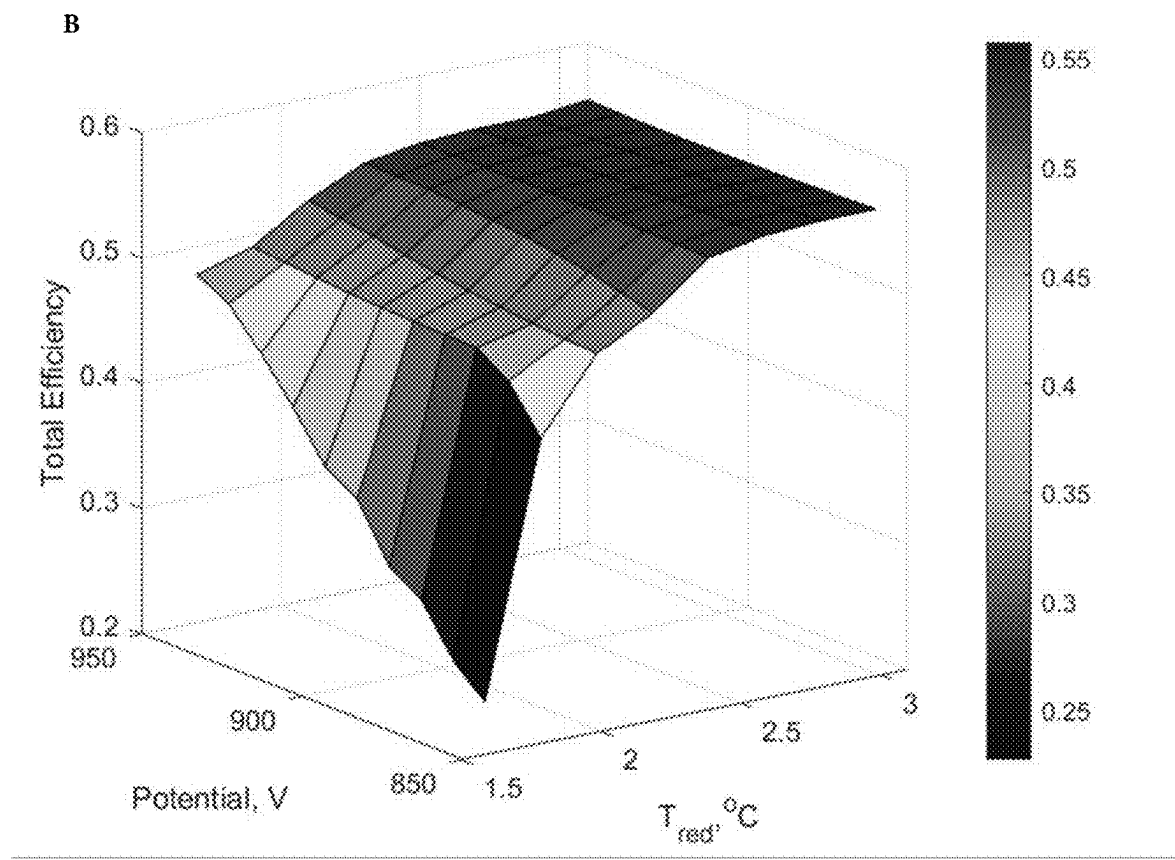


FIG. 19 (CONT.)

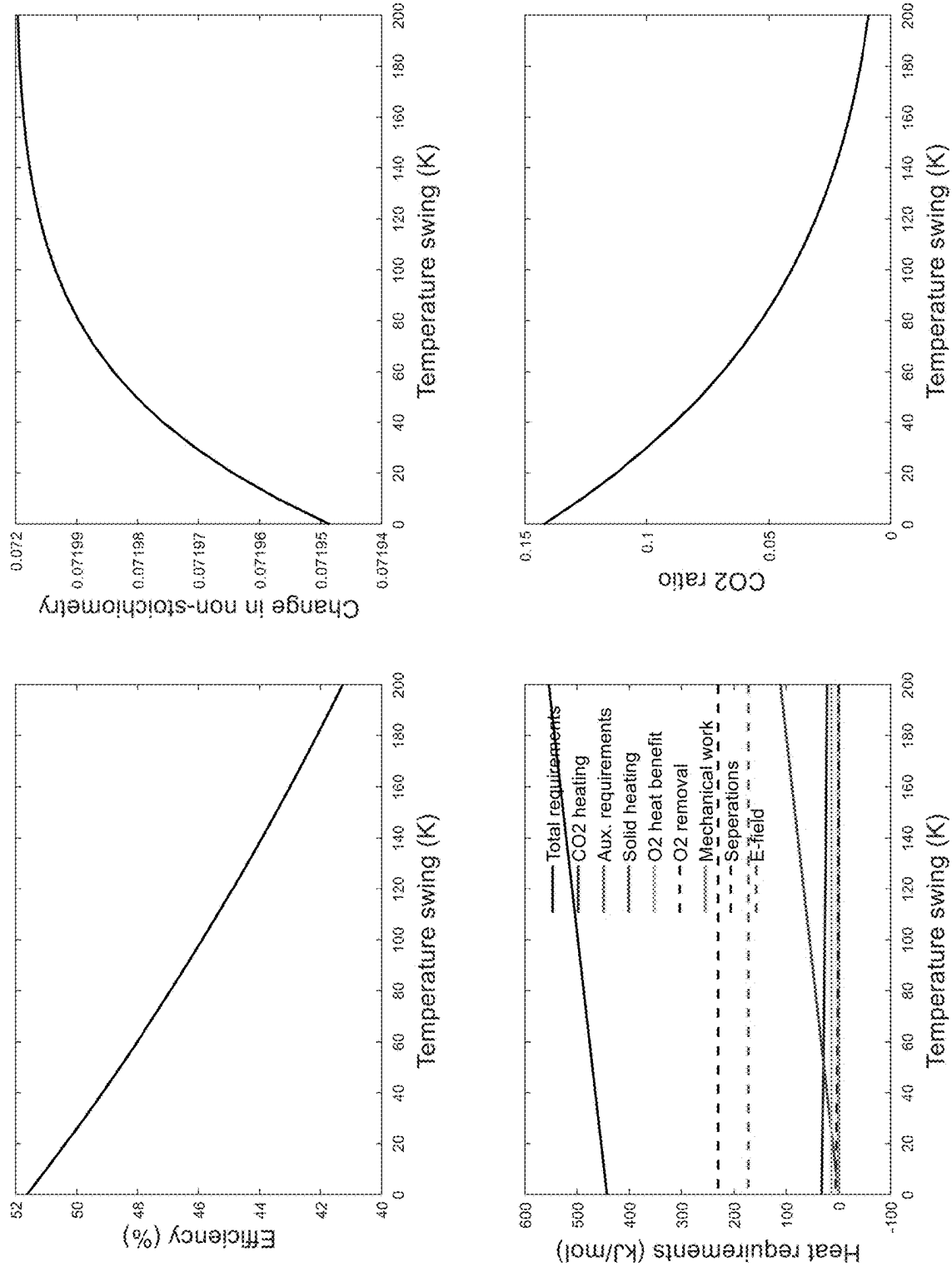


FIG. 20

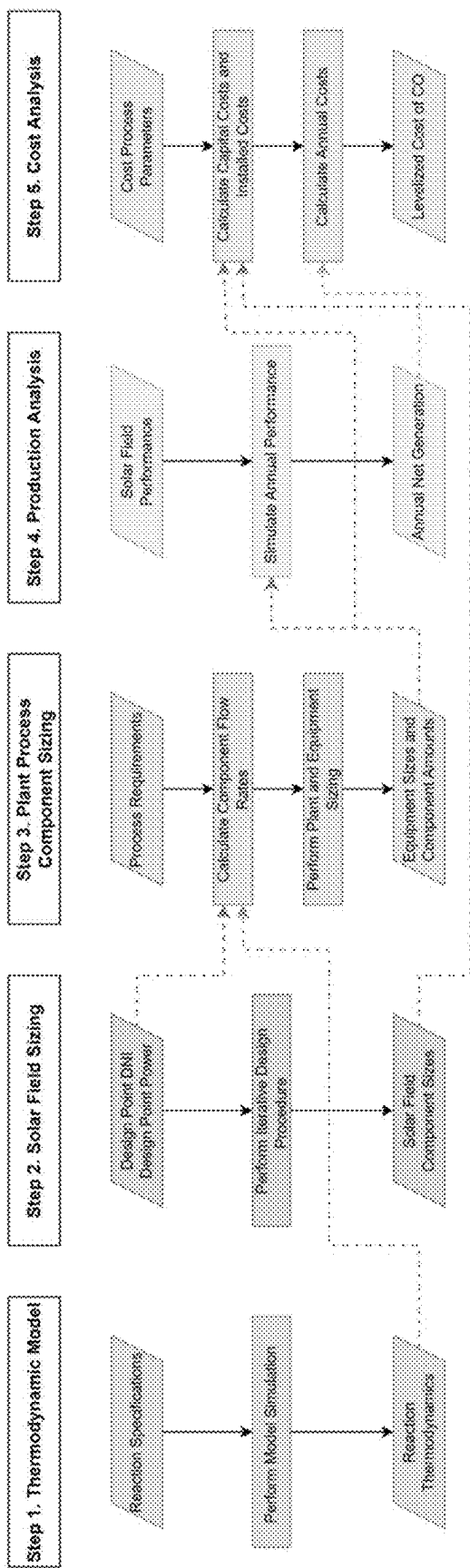


FIG. 21

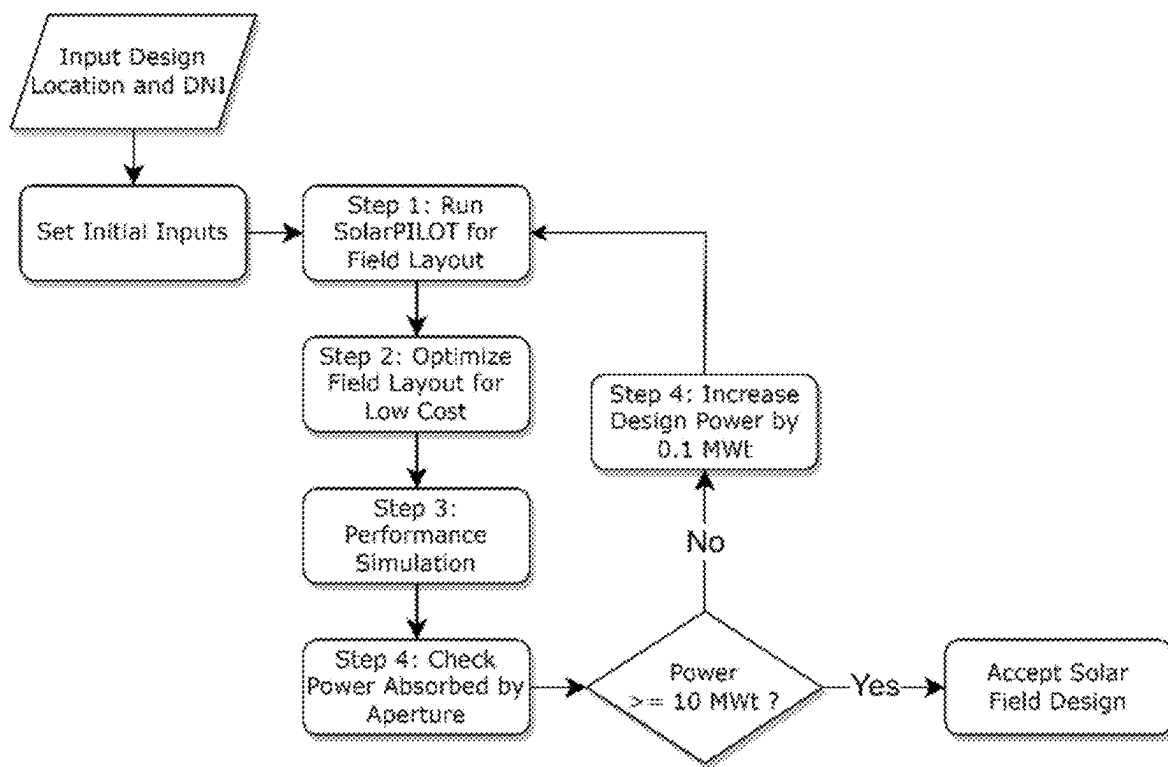


FIG. 22

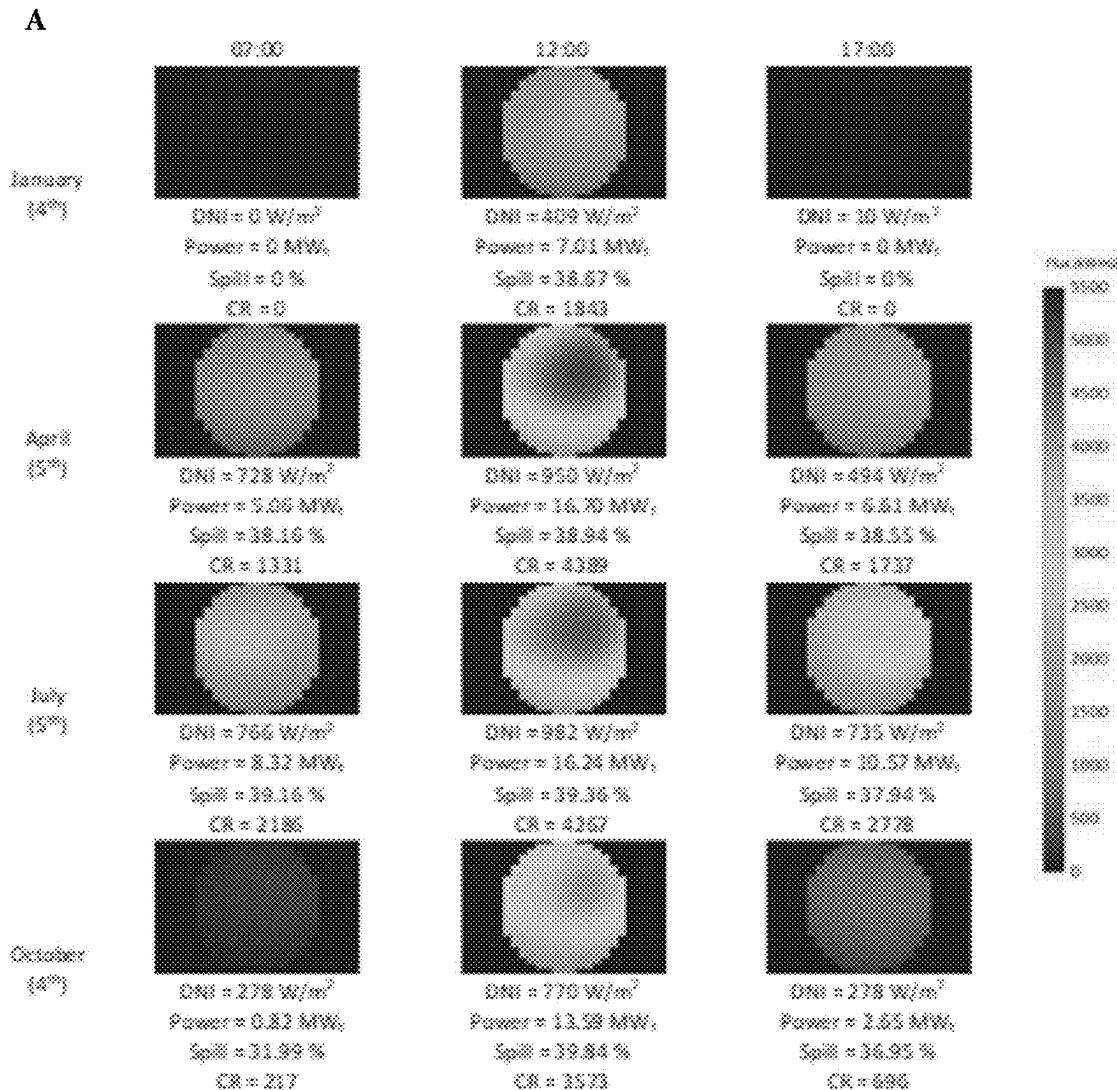


FIG. 23

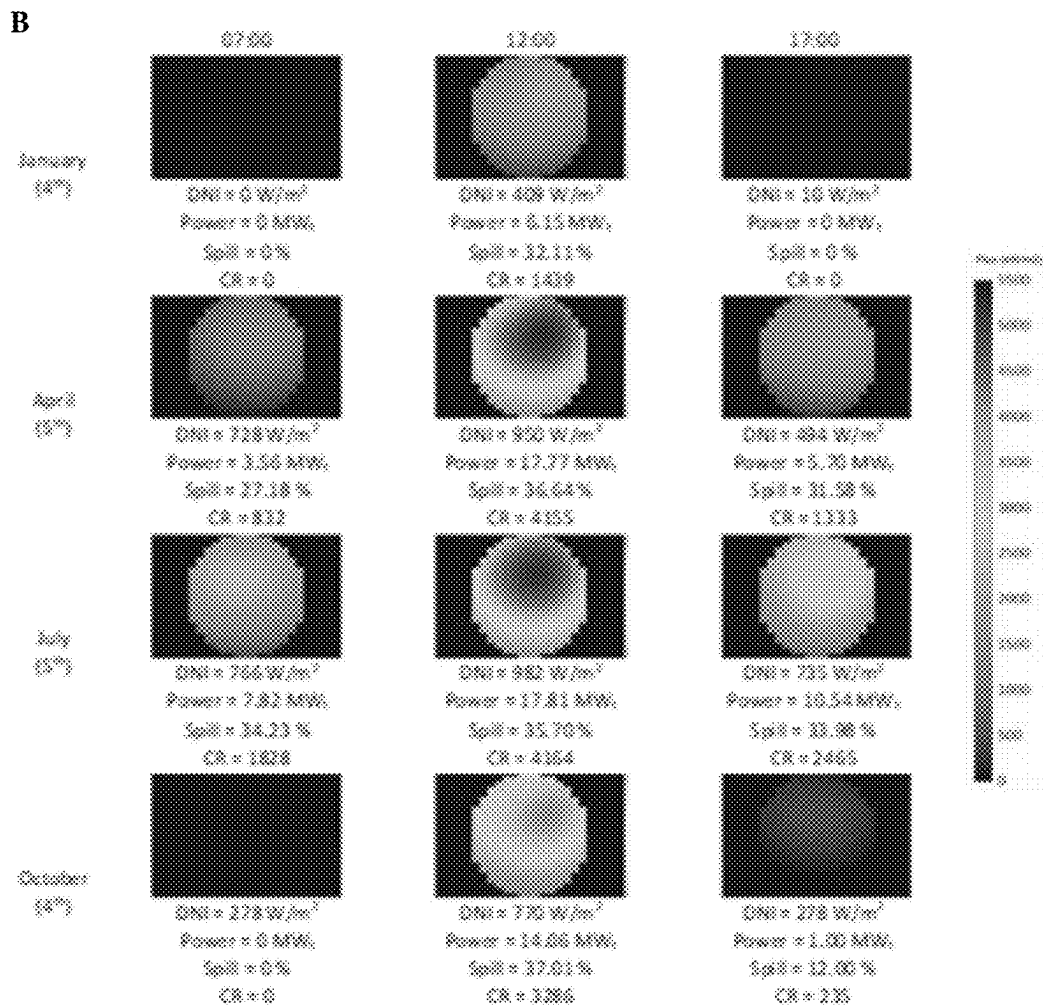


FIG 23 (CONT.)

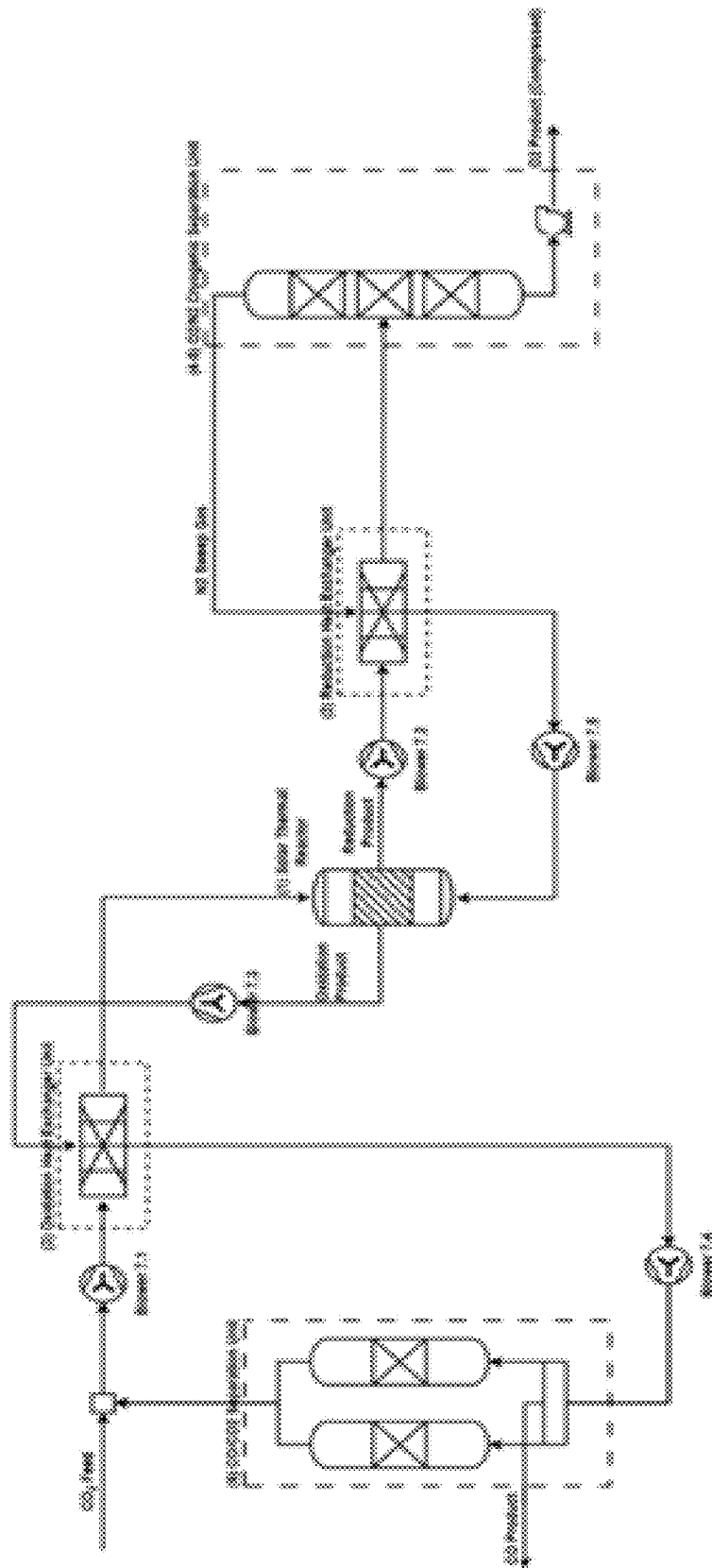


FIG. 24

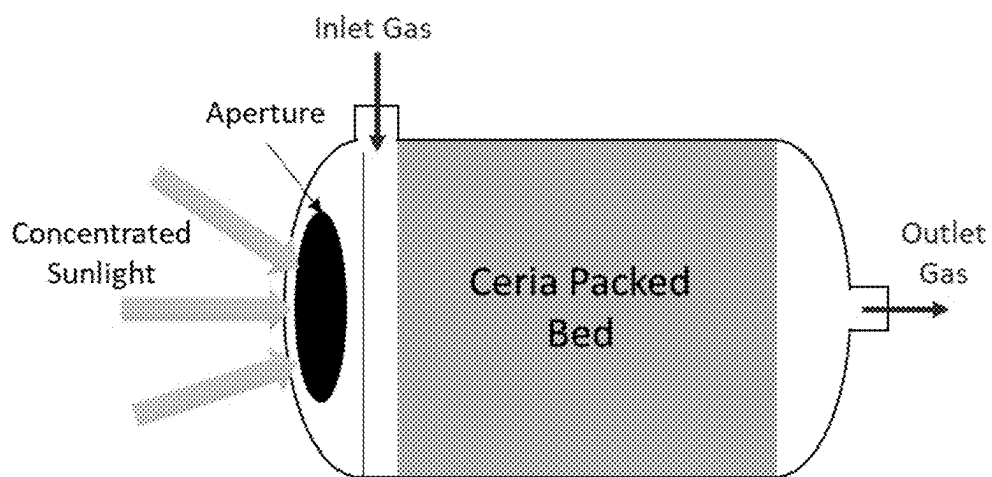


FIG. 25

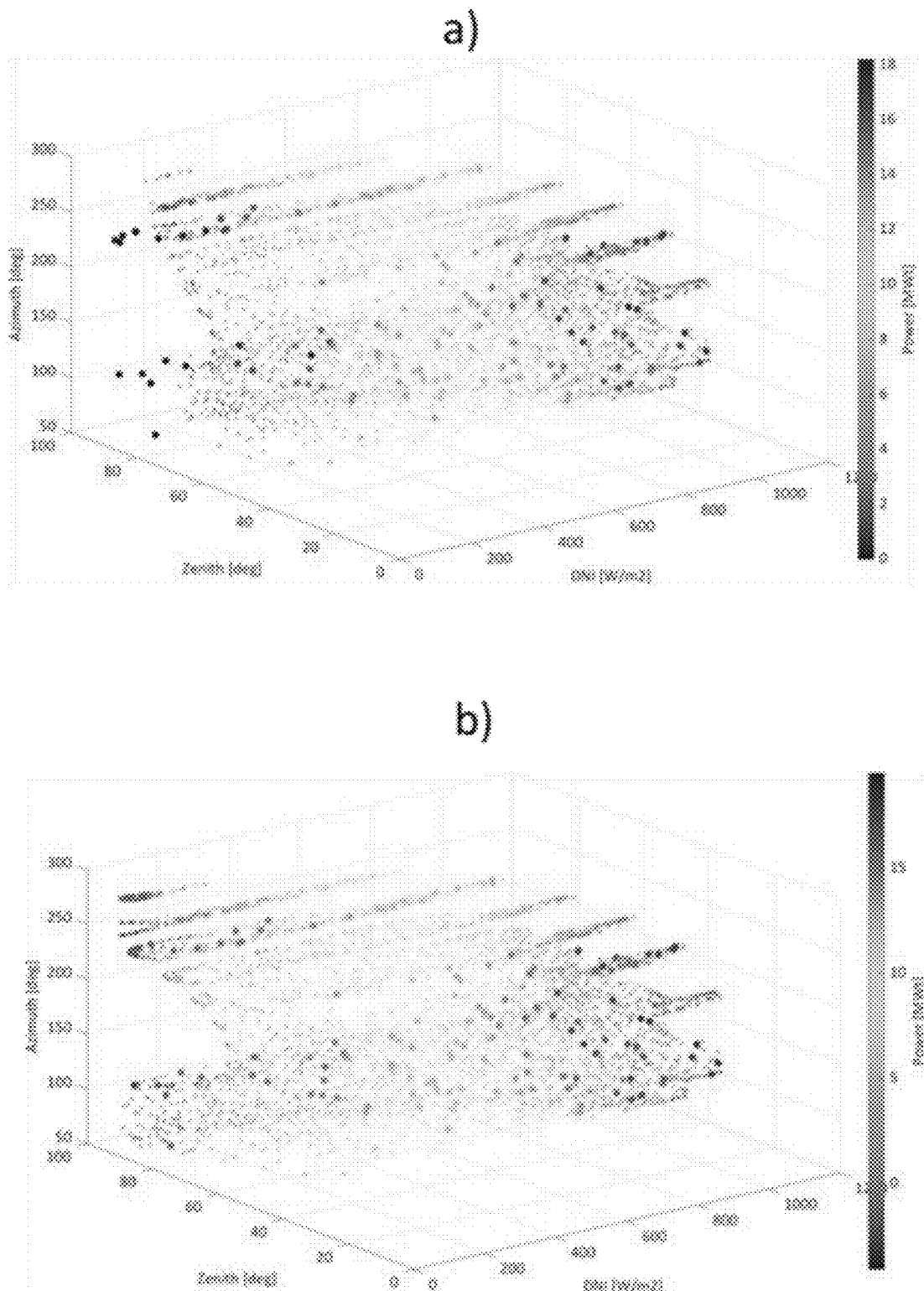


FIG. 26

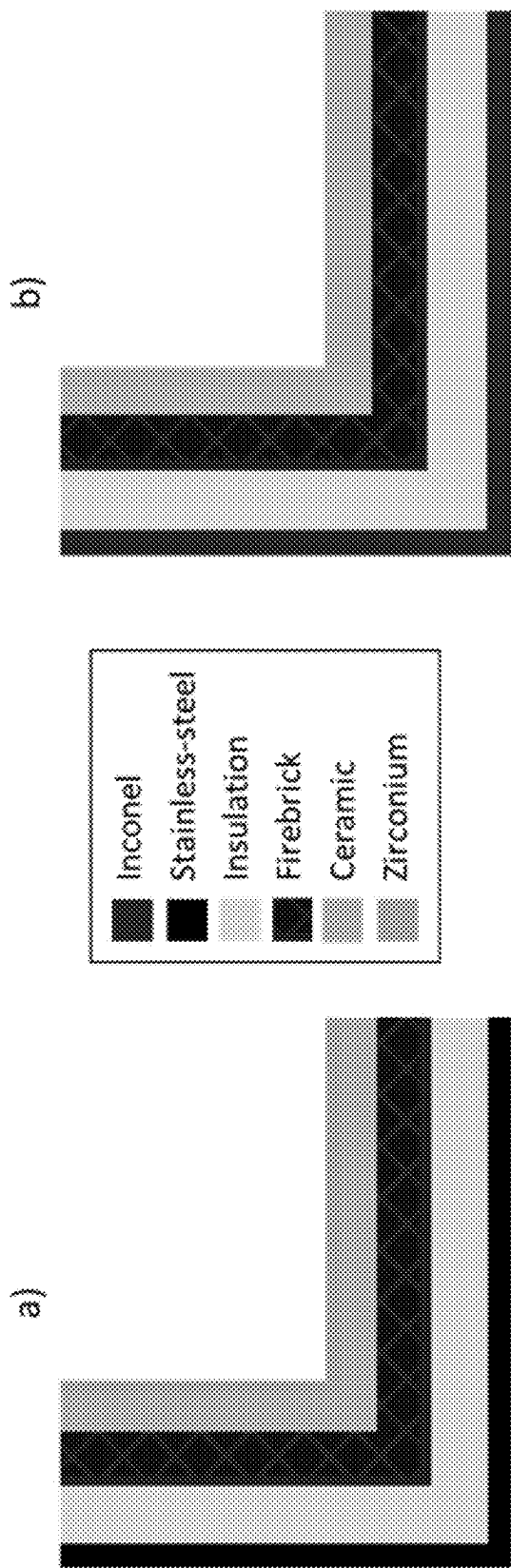


FIG. 27

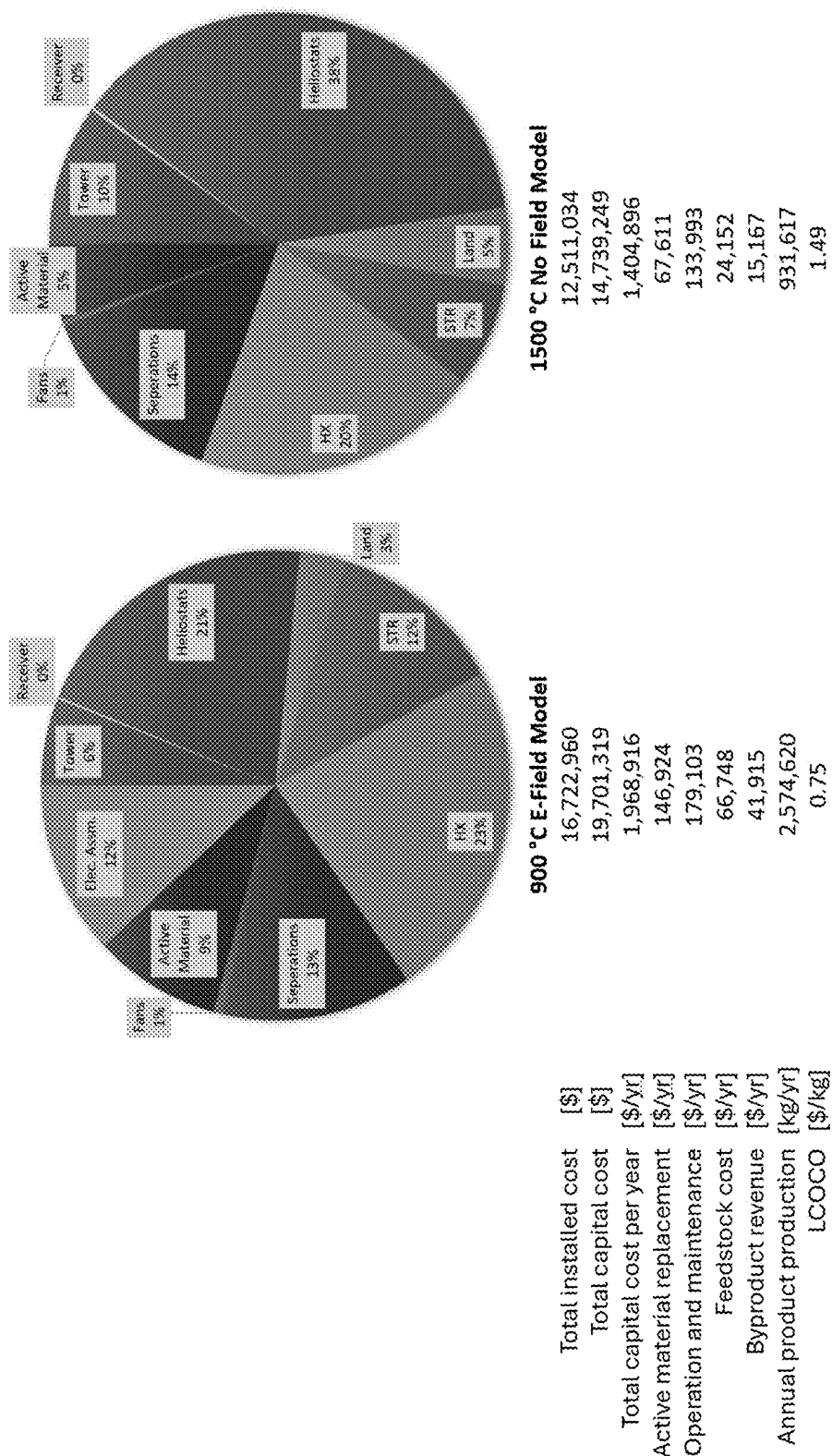


FIG. 28

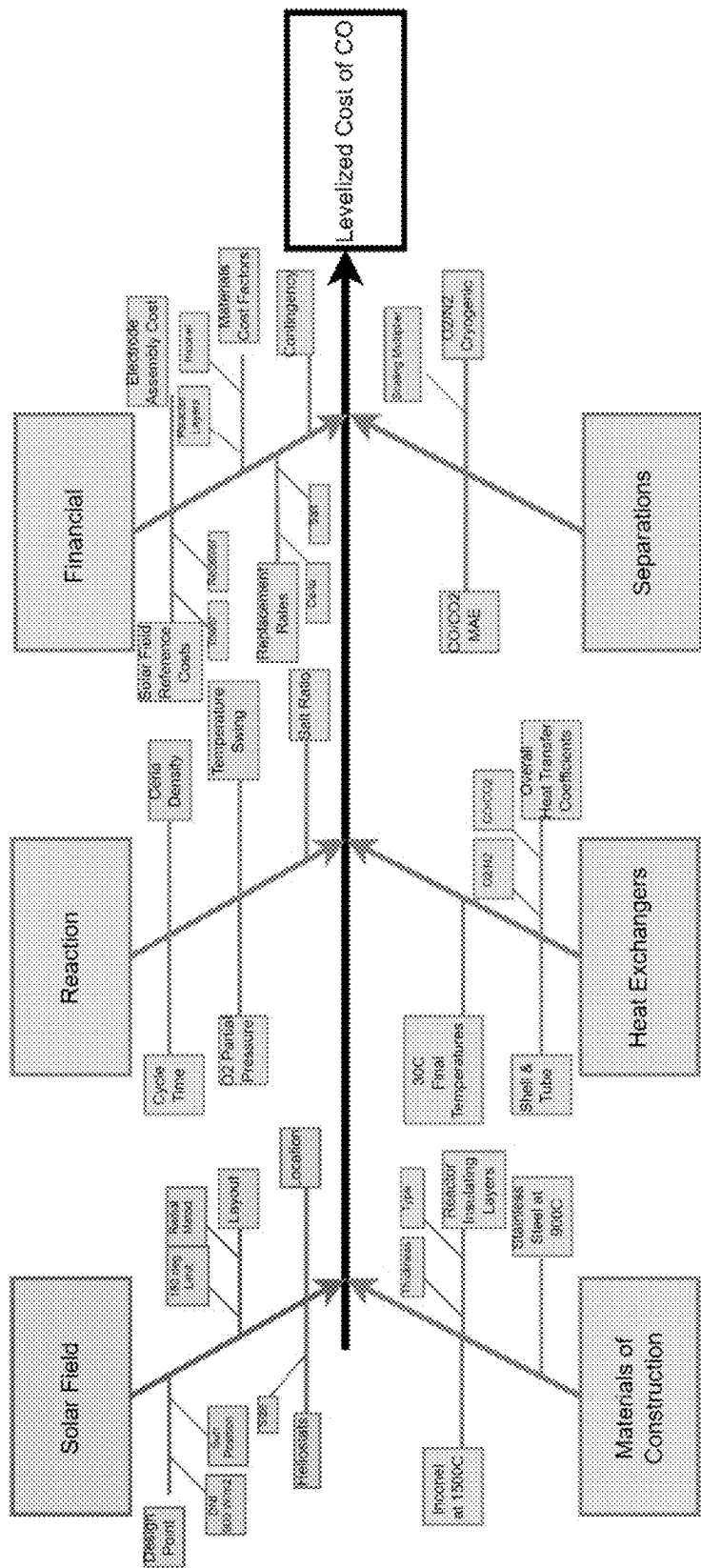


FIG. 29

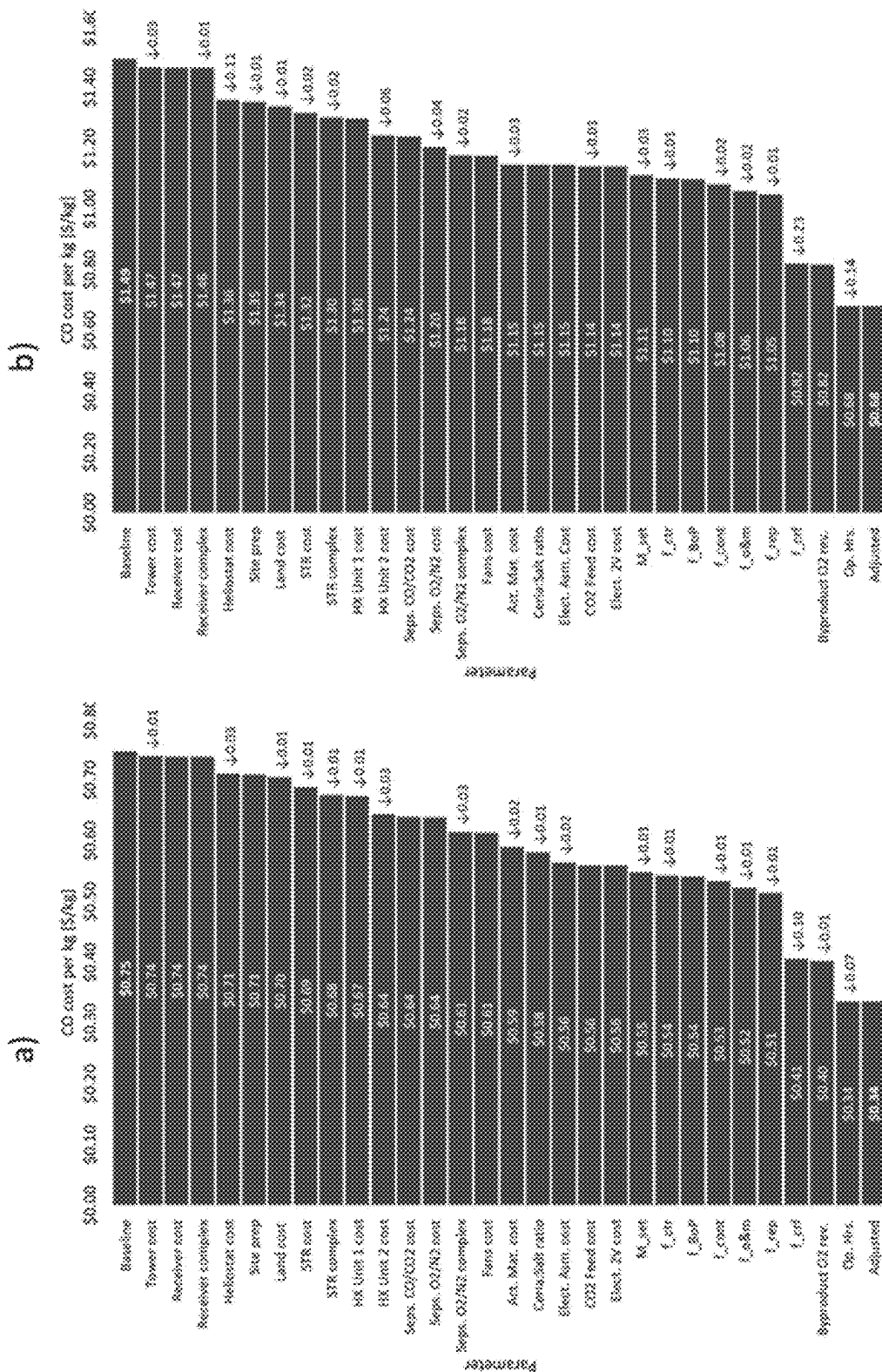


FIG. 30

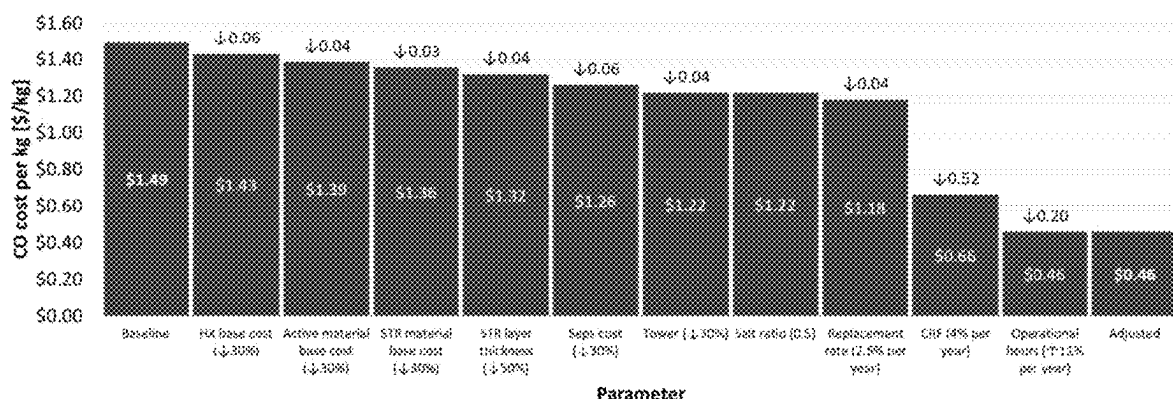
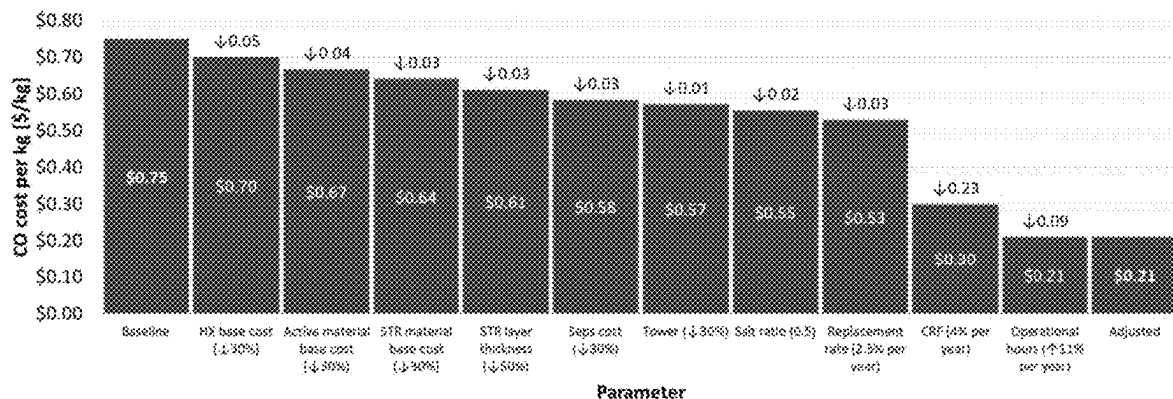


FIG. 31

SOLAR THERMOCHEMICAL FUEL PRODUCTION SYSTEM AND METHODS OF USE THEREOF

[0001] This application claims priority to U.S. Provisional Application No. 63/554,702 filed on Feb. 16, 2024, the entire contents of which are incorporated herein by reference.

[0002] All patents, patent applications and publications cited herein are hereby incorporated by reference in their entirety. The disclosures of these publications in their entireties are hereby incorporated by reference into this application in order to more fully describe the state of the art as known to those skilled therein as of the date of the invention described and claimed herein.

[0003] This patent disclosure contains material that is subject to copyright protection. The copyright owner has no objection to the facsimile reproduction by anyone of the patent document or the patent disclosure as it appears in the U.S. Patent and Trademark Office patent file or records, but otherwise reserves any and all copyright rights.

GOVERNMENT INTERESTS

[0004] This invention was made with government support under DE-EE0009817 awarded by the Department of Energy. The government has certain rights in the invention.

FIELD OF THE INVENTION

[0005] The invention relates to solar thermochemical fuel production systems and methods of use thereof.

BACKGROUND OF THE INVENTION

[0006] In conventional solar thermochemical CO₂ splitting (STCS), a metal oxide is heated to its reduction temperature using concentrated solar thermal energy, liberating O₂, and in a subsequent step, the reduced material is exposed to CO₂ which re-oxidizes the active material releasing the desired carbon monoxide (CO). Conventional solar thermal CO₂ splitting systems are costly as they operate at high temperatures in the range of 1200-1500° C.

SUMMARY OF THE INVENTION

[0007] Aspects of the invention are drawn towards a method of performing thermochemical gas splitting at a reduced operating temperature, the method comprising: connecting a metal oxide (M_yO_x) to a first electrode connected to a power source; placing a second electrode connected to the power source in an electrolyte; submerging the M_yO_x connected to the first electrode in the electrolyte and subjecting the M_yO_x and electrolyte to an increased temperature; applying a potential to the M_yO_x and electrolyte, thereby eliciting an electronic double layer at the M_yO_x/electrolyte interface and reducing the (M_yO_x) to form a non-stoichiometric oxide (M_yO_{x-δ}) or a stoichiometric metal oxide (M_yO_{x-1}); and oxidizing the M_yO_{x-δ} or the M_yO_{x-1} with an oxidizing agent to regenerate the M_yO_x, thereby generating a gas product, heat, or a combination thereof. In embodiment, submerging comprises submerging about 25% to about 75% of the metal oxide. In embodiments, the electrolyte is selected from an ionic liquid, a molten salt, or a combination thereof. In embodiments, the ionic liquid or molten salt is selected from sodium, potassium, lithium, calcium, and magnesium carbonates, chlorides, sulphates, phosphates, or a mixture thereof.

In embodiments, the molten salt is selected from NaCl, KCl, MgCl₂, CaCl₂, LiCl, Na₂SO₄, K₂SO₄, Li₂SO₄, CaCO₃, Li₂CO₃, K₂CO₃, or a combination thereof. In embodiments, the metal oxide (M_yO_x) is selected from ceria (CeO₂), SrLaMnO₃, BaFeO₃, Fe₃O₄, FeAl₂O₄, CoFe₂O₄, CoFeAl₂O₄, perovskites, ceria derivatives, spinel ferrites, or a combination thereof. In embodiments, the increased temperature is selected from a temperature of about 1375° C., about 1350° C., about 1325° C., about 1300° C., about 1275° C., about 1250° C., about 1225° C., about 1200° C., about 1175° C., about 1150° C., about 1125° C., about 1100° C., about 1075° C., about 1050° C., about 1025° C., about 1000° C., about 975° C., about 950° C., about 925° C., about 900° C., about 875° C., about 850° C., about 825° C., about 800° C., about 775° C., about 750° C., about 725° C., about 700° C., about 675° C., about 650° C., about 625° C., about 600° C., about 575° C., about 550° C., about 500° C., or below about 500° C. In embodiments, the potential is selected from less than about 0.25V, about 0.25V, about 0.5V, about 0.75V, about 1.0V, about 1.25V, about 1.50V, about 1.75V, about 2.0V, about 2.25V, about 2.5V, about 2.75V, about 3.0V, about 3.5V, about 4.0V, about 4.25V, about 4.5V, about 4.75V, about 5.0V, about 5.25V, about 5.5V, about 5.75V, about 6.0V, or greater than about 6.0V. In embodiments, the gas product is selected from H₂, CO, or a combination thereof. In embodiments, the method is performed at a partial pressure of about 1 Pa, about 10 Pa, about 50 Pa, about 100 Pa, about 200 Pa, about 250 Pa, about 300 Pa, about 350 Pa, about 400 Pa, about 450 Pa, about 500 Pa, about 550 Pa, about 600 Pa, about 650 Pa, about 700 Pa, about 750 Pa, about 800 Pa, about 850 Pa, about 900 Pa, about 950 Pa, about 1000 Pa, or greater than about 1000 Pa. In embodiments, the method has an O₂ Faradaic efficiency of about 100%, about 125%, about 150%, about 175%, about 200%, or greater than about 200%. In embodiments, the electronic double layer produces an E-field of about 5 V/nm or greater than 5 V/nm. In embodiments, the method has a gas production capability of about 100 to about 500 μmol gas/g metal oxide.

[0008] Aspects of the disclosure are drawn towards an electric field enhanced CO₂ splitting system comprising: a reactor comprising a metal oxide, a molten salt or ionic liquid, and an electrode; and a heat source. In embodiments, the system further comprises a reduction heat exchanger unit, an oxidation heat exchanger unit, a reduction production separation unit, an oxidation production separation unit, heat storage tanks, a solar furnace, a turbine, one or more blowers, or a combination thereof. In embodiments, the ionic liquid or molten salt comprises sodium, potassium, lithium, calcium, and magnesium carbonates, chlorides, sulphates, phosphates, or a mixture thereof. In embodiments, the molten salt comprises NaCl, KCl, MgCl₂, CaCl₂, LiCl, Na₂SO₄, Li₂SO₄, K₂SO₄, CaCO₃, Li₂CO₃, K₂CO₃, or a combination thereof. In embodiments, the metal oxide (M_yO_x) comprises ceria (CeO₂), SrLaMnO₃, BaFeO₃, Fe₃O₄, FeAl₂O₄, CoFe₂O₄, CoFeAl₂O₄, perovskites, ceria derivatives, spinel ferrites, or a combination thereof. In embodiments, the system is an industrial system further comprising a reduction production separation unit, an oxidation production separation unit, heat storage tanks, a solar furnace, a turbine, one or more blowers, or a combination thereof. In embodiments, the industrial system comprises the process flow diagram of FIG. 24.

[0009] Other objects and advantages of this invention will become readily apparent from the ensuing description.

BRIEF DESCRIPTION OF THE FIGURES

[0010] FIG. 1 shows an exemplary (Left) Solar thermal E-field Reduction. During on-sun operating and in the presence of an applied potential, an EDL forms at the CeO₂-ionic liquid interface, creating a large E-field reducing CeO₂, releasing O₂. (Right) Thermochemical CO₂ splitting. With no added potential or solar thermal input, reduced ceria is dosed with CO₂, oxidized CeO_{2-δ}, and forming CO.

[0011] FIG. 2 shows exemplary pictures of Decomposed molten salts, (left) MgCl₂, (middle) CaCO₃, (right) Li₂CO₃ and (far right) K₂CO₃ after 48 hour dwell, in air, at 900° C.

[0012] FIG. 3 shows non-limiting, exemplary XRD patterns of CeO₂ and Na₂SO₄ before and after holds in air, inert and 1V applied potential showing no changes in behavior.

[0013] FIG. 4 shows a non-limiting, exemplary (top) Experimental setup for E-field enhanced CeO₂ reduction for CO₂ splitting. (bottom) Measured current, I, for a constant applied voltage of 1V on Na₂SO₄.

[0014] FIG. 5 shows a non-limiting, exemplary data from cyclic voltammetry experiments of the pure salt and the salt/CeO₂ combined system.

[0015] FIG. 6 shows a non-limiting, exemplary SEM images of Pore morphology before (top) and after cycling (bottom).

[0016] FIG. 7 shows a non-limiting, exemplar EDS of Na₂SO₄—CeO₂ after exposure to 1V.

[0017] FIG. 8 shows a non-limiting, exemplary schematic and picture of E-field thermochemical CO₂ splitting reactor and furnace.

[0018] FIG. 9 shows non-limiting, exemplary results from reactor cycles. Electrically enhanced CO₂ splitting over CeO₂ using molten salt, Na₂SO₄. The system remains isothermal at 900° C. (purple) with a constant stream of Ar inert. The system cycles between inducing reduction by applying 4V (green) to from the EDL, purging with an inert, and oxidation by dosing CO₂ (blue). O₂ (red) is generated under only the influence of the applied potential as the system is reduced, and CO is produced as CeO₂ oxidizes, splitting CO₂.

[0019] FIG. 10 shows a non-limiting, exemplary sample ceria cells shown from a) top view schematic, b) side view schematic, c) real sample cell. With ZrO₂ coated-Al₂O₃ crucibles (gray) filled with ~2 g Na₂SO₄ (pink). One Pt electrode (dark gray) is immersed in the salt, the second is attached to the ceria pellet (yellow).

[0020] FIG. 11 shows a non-limiting, exemplary graphs of data described here. (Top) Densities of porous ceria materials, (bottom) O₂ generation for different ceria-to-carbon ratio pellets FIG. 12 shows a non-limiting, exemplary SEM pore morphologies.

[0021] FIG. 13 shows a non-limiting, exemplary pictures of electrode materials and shape tests.

[0022] FIG. 14 shows a non-limiting, exemplary graphs of O₂ generation for 10 redox cycles.

[0023] FIG. 15 shows a non-limiting, exemplary mass and flow diagram in the solar thermochemical CO₂ splitting model described herein.

[0024] FIG. 16 shows a non-limiting, exemplary system model results for conventional solar thermochemical CO₂ splitting at 1500° C. Top left: system efficiency as a function of temperature swing between reduction and oxidation tem-

perature. Top right: change in CeO₂ non-stoichiometry between reduction and oxidation steps, indicating how much CO is produced per mol CeO₂ per loop. Bottom Left, the heat requirements for various flows as a function of temperature swing. Bottom right: the molar ratio of CO₂ flowing through the system for each mol of CO produced.

[0025] FIG. 17 shows a non-limiting, exemplary system model results for conventional solar thermochemical CO₂ splitting at 900° C. Top left: system efficiency as a function of temperature swing between reduction and oxidation temperature. Top right: change in CeO₂ non-stoichiometry between reduction and oxidation steps, indicating how much CO is produced per mol CeO₂ per loop. Bottom Left, the heat requirements for various flows as a function of temperature swing. Bottom right: the molar ratio of CO₂ flowing through the system for each mol of CO produced.

[0026] FIG. 18 shows a non-limiting, exemplary thermodynamic analysis of E-field solar thermochemical CO₂ splitting at 900° C. Top left: system efficiency as a function of temperature swing. Top right: change in CeO₂ non-stoichiometry Bottom Left, the heat requirements for various flows. Bottom right: the molar ratio of CO₂ flowing through the system for each mol of CO produced.

[0027] FIG. 19 shows a non-limiting, exemplary sensitivity analysis results. Top: Cross sensitivity analysis looking at pairs of variables that deviate from the base case of T_{red}=900° C., P_{red}=10 Pa (10⁻⁴ bar), V=2 V, e_{ss}=e_{gg}=50%, and n_{pump}=5%. Bottom: close of exemplary important pairs.

[0028] FIG. 20 shows a non-limiting, exemplary solar to CO efficiency based on the experimental CO production performance.

[0029] FIG. 21 shows a non-limiting, exemplary schematic of a workflow from thermodynamic system level model to economic cost analysis.

[0030] FIG. 22 shows a non-limiting, exemplary flowchart of Solar Field Design and Optimization Process.

[0031] FIG. 23 shows a non-limiting, exemplary solar field receiver aperture results for (left) 900° C. E-field model, and (right) 1500° C. No field model.

[0032] FIG. 24 shows a non-limiting, exemplary process flow diagram. In non-limiting embodiments, the plant process flow diagram includes 1) reactor, 2) reduction heat exchanger unit, 3) oxidation heat exchanger unit, 4) reduction product separation unit, 5) oxidation product separation unit, and 7.1-7.4) fans.

[0033] FIG. 25 shows a non-limiting, exemplary solar thermal reactor design for E-field and no field models described herein.

[0034] FIG. 26 shows a non-limiting, exemplary performance model power prediction for every hour of the year for a) 900° C. E-field model and b) 1500° C. no field model.

[0035] FIG. 27 shows a non-limiting, exemplary schematic of reactor insulating layers for a) 900° C. E-field model and b) 1500° C. E-field model.

[0036] FIG. 28 shows a non-limiting, exemplary schematic of the cost breakdown for the a) 900° C. e-field model and b) 1500° C. no field model.

[0037] FIG. 29 shows a non-limiting, exemplary fishbone diagram of general model parameters to vary for decreasing costs.

[0038] FIG. 30 shows non-limiting, exemplary tornado charts for a 20% adjustment to model parameters to achieve lower LCOCO for the a) e-field model and b) no field model.

[0039] FIG. 31 shows non-limiting, exemplary Waterfall charts indicating a path to \$0.21/kg CO for panel a) e-field model and what the equivalent resulting cost of the panel b) no field model.

DESCRIPTION OF THE INVENTION

[0040] Non-limiting descriptions of one or more embodiments are provided herein. It is to be understood, however, that the invention can be embodied in various forms. Therefore, specific details disclosed herein are not to be interpreted as limiting, but rather as a basis for the claims and as a representative basis for teaching one skilled in the art to employ the invention in any appropriate manner.

[0041] The singular forms “a”, “an” and “the” include plural reference unless the context clearly dictates otherwise. The use of the word “a” or “an” when used in conjunction with the term “comprising” in the claims and/or the specification can mean “one,” but it is also consistent with the meaning of “one or more,” “at least one,” and “one or more than one.”

[0042] Wherever any of the phrases “for example,” “such as,” “including” and the like are used herein, the phrase “and without limitation” is understood to follow unless explicitly stated otherwise. Similarly, “an example,” “exemplary” and the like are understood to be nonlimiting.

[0043] The term “substantially” allows for deviations from the descriptor that do not negatively impact the intended purpose. Descriptive terms are understood to be modified by the term “substantially” even if the word “substantially” is not explicitly recited.

[0044] The terms “comprising” and “including” and “having” and “involving” (and similarly “comprises”, “includes,” “has,” and “involves”) and the like are used interchangeably and have the same meaning. Specifically, each of the terms is defined consistent with the common United States patent law definition of “comprising” and is therefore interpreted to be an open term meaning “at least the following,” and is also interpreted not to exclude additional features, limitations, aspects, etc. Thus, for example, “a process involving steps a, b, and c” means that the process includes at least steps a, b and c. Wherever the terms “a” or “an” are used, “one or more” is understood, unless such interpretation is nonsensical in context.

[0045] As used herein, the term “about” can refer to approximately, roughly, around, or in the region of. When the term “about” is used in conjunction with a numerical range, it modifies that range by extending the boundaries above and below the numerical values set forth. In general, the term “about” is used herein to modify a numerical value above and below the stated value by a variance of 20 percent up or down (higher or lower). In embodiments, the term “about” can be denoted by “~”

[0046] As used herein, the term “substantially the same” or “substantially” can refer to variability typical for a particular method is taken into account.

[0047] The terms “sufficient” and “effective”, as used interchangeably herein, can refer to an amount (e.g., mass, volume, dosage, concentration, and/or time period) needed to achieve one or more result(s).

[0048] Before explaining at least one embodiment of the disclosure in detail, it is to be understood that the disclosure is not necessarily limited in its application to the details set forth in the following description or exemplified by the examples. The disclosure can be used for other embodiments

or of being practiced or carried out in various ways. Other compositions, compounds, methods, features, and advantages of the disclosure will be or become apparent to one having ordinary skill in the art upon examination of the following drawings, detailed description, and examples. All such additional compositions, compounds, methods, features, and advantages can be included within this description, and be within the scope of the disclosure.

[0049] In some embodiments, the disclosure is drawn towards a method of performing thermochemical gas splitting at a reduced operating temperature, the method comprising: connecting a metal oxide (M_yO_x) to a first electrode connected to a power source; placing a second electrode connected to the power source in an electrolyte; submerging the M_yO_x connected to the first electrode in the electrolyte and subjecting the M_yO_x and electrolyte to an increased temperature; applying a potential to the M_yO_x and electrolyte, thereby eliciting an electronic double layer at the M_yO_x /electrolyte interface and reducing the (M_yO_x) to form a non-stoichiometric oxide ($M_yO_{x-\delta}$) or a stoichiometric metal oxide (M_yO_{x-1}); and oxidizing $M_yO_{x-\delta}$ or M_yO_{x-1} with an oxidizing agent to regenerate the M_yO_x , thereby generating a gas product, heat, or a combination thereof.

[0050] In embodiments, the electrode is submerged about 5% to about 100%. For example, the electrode is submerged about 25% to about 50%. For example, the electrode is submerged about 2.5%, about 5%, about 7.5%, about 10%, about 12.5%, about 15%, about 17.5%, about 20%, about 22.5%, about 25%, about 27.5%, about 30%, about 35%, about 40%, about 45%, about 50%, about 55%, about 60%, about 65%, about 70%, about 75%, about 80%, about 85%, about 90%, about 95%, or about 100%.

[0051] As used herein, the term metal oxide can refer to a composition comprising one or more metals and one or more oxygens. For example, the metal oxide can comprise a metal cation and an oxide anion. For example, as used herein, in some embodiments, the term metal oxide can refer to a composition comprising an oxide anion (O^{2-}) that is bound to one or more metal or metal alloys. For example, as used herein, the term metal oxide can refer to an oxide mineral, perovskites, ceria derivatives, spinel ferrites, or a combination thereof. For example, the metal oxide can comprise CeO_2 , $SrLaMnO_3$, $BaFeO_3$, Fe_3O_4 , $FeAl_2O_4$, $CoFe_2O_4$, $CoFeAl_2O_4$, perovskites, ceria derivatives, spinel ferrites, or a combination thereof. For example, the disclosure can encompass any metal oxide, oxide mineral, perovskite, ceria derivative, or spinel ferrite known in the art. In embodiments, the metal oxide is CeO_2 .

[0052] In embodiments, the metal oxide can comprise a general formula of M_yO_x whereby M_y can refer to one or more metals, metal alloys, or a combination thereof. For example, M_y can refer to “ Fe_2 ” in Fe_2O_3 or M_y can refer to “ $MgAl_2$ ” in $MgAl_2O_4$.

[0053] In embodiments, the electrolyte comprises an ionic liquid or a molten salt. As used herein, the terms “ionic liquid” and “molten salt” can be used interchangeably. In embodiments, the term “ionic liquid” can refer to a salt which is in the liquid state at ambient temperature and pressure. In embodiments, the term “molten salt” can refer to a salt that is solid at ambient temperature and pressure but can become a liquid when thermal energy is applied.

[0054] In embodiments, the ionic liquid or molten salt can comprise any ionic liquid or molten salt known in the art. For example, the ionic liquid or molten salt can comprise

sodium, potassium, lithium, calcium, and magnesium carbonates, chlorides, sulphates, phosphates, or a mixture thereof. For example, the ionic liquid or molten salt can be selected from NaCl, KCl, MgCl₂, CaCl₂, LiCl, Na₂SO₄, K₂SO₄, Li₂SO₄, CaCO₃, Li₂CO₃, K₂CO₃, or a combination thereof. In some embodiments, the ionic liquid or molten salt can be Na₂SO₄, K₂SO₄, Li₂SO₄, or a combination thereof.

[0055] In embodiments, the reduced operating temperature can comprise a temperature of about 1400° C. or below. For example about 1375° C., about 1350° C., about 1325° C., about 1300° C., about 1275° C., about 1250° C., about 1225° C., about 1200° C., about 1175° C., about 1150° C., about 1125° C., about 1100° C., about 1075° C., about 1050° C., about 1025° C., about 1000° C., about 975° C., about 950° C., about 925° C., about 900° C., about 875° C., about 850° C., about 825° C., about 800° C., about 775° C., about 750° C., about 725° C., about 700° C., about 675° C., about 650° C., about 625° C., about 600° C., about 575° C., about 550° C., about 500° C., or below about 500° C.

[0056] In embodiments, the potential applied to the system comprises less than about 0.25V, about 0.25V, about 0.5V, about 0.75V, about 1.0V, about 1.25V, about 1.50V, about 1.75V, about 2.0V, about 2.25V, about 2.5V, about 2.75V, about 3.0V, about 3.5V, about 4.0V, about 4.25V, about 4.5V, about 4.75V, about 5.0V, about 5.25V, about 5.5V, about 5.75V, about 6.0V, or greater than about 6.0V.

[0057] In embodiments, the power source comprises a nuclear energy source, a fossil energy source, or a renewable energy source. For example, the power source comprises electrical grid power, turbine power, or generator power. In embodiments, the renewable energy source comprises solar energy, wind energy, geothermal energy, hydropower, ocean energy, or bioenergy.

[0058] In embodiments, the system can produce a reduced gas product. For example, the gas produce can comprise H₂, CO, or a combination thereof.

[0059] In embodiments, the oxidizing agent can comprise any oxygen containing organic compound known in the art. For example, the oxygen containing organic compound comprises H₂O, CO₂, O₂, O₃, H₂O₂, HNO₃, KClO₃, H₂S₂O₈, KMnO₄, (NH₄)₂S₂O₈, or a combination thereof.

[0060] In embodiments, the method can be performed at a partial pressure of about 1 Pa, about 10 Pa, about 50 Pa, about 100 Pa, about 200 Pa, about 250 Pa, about 300 Pa, about 350 Pa, about 400 Pa, about 450 Pa, about 500 Pa, about 550 Pa, about 600 Pa, about 650 Pa, about 700 Pa, about 750 Pa, about 800 Pa, about 850 Pa, about 900 Pa, about 950 Pa, about 1000 Pa, or greater than about 1000 Pa.

[0061] As used herein, the term Faradaic efficiency can refer to the efficiency of the supplied electrons from the E-field to the electrons of the generated species (i.e., O₂ or CO). In embodiments, the method can have an O₂ Faradaic efficiency of about 100%, about 125%, about 150%, about 175%, about 200%, or greater than about 200%.

[0062] In embodiments, the electronic double layer can produce an E-field of about 5 V/nm or greater than 5 V/nm.

[0063] As used herein, the term "gas production" capability can refer to the production of a gas from the splitting of another gas using the reduced metal oxide. For example, gas production capability can refer to the production of CO from splitting CO₂ using the reduced CeO₂-delta material. In embodiments, the methods described have a gas production capability of about 100 μmol gas/g metal oxide to about 500

μmol gas/g metal oxide. For example, the methods described herein have a gas production capability of about 50, about 75, about 100, about 125, about 150, about 175, about 200, about 225, about 250, about 275, about 300, about 325, about 350, about 375, about 400, about 425, about 450, about 500, about 525, about 550, about 575, about 600, about 625, about 650, about 675, about 700, about 725, about 750, about 775, about 800, about 850, about 900, about 950, about 1000, or greater than about 1000 μmol gas/g metal oxide. For example, the gas production capability can comprise about 150 μmol CO/g CeO₂ to about 500 μmol CO/g CeO₂. For example, the gas production capability can comprise about 150 μmol H₂/g CeO₂ to about 500 μmol H₂/g CeO₂.

[0064] Aspects of the disclosure are drawn towards an electric field enhanced CO₂ splitting system comprising: a reactor comprising a metal oxide, a molten salt or ionic liquid, and an electrode; and a heat source.

[0065] In some embodiments, the system further comprises a reduction heat exchanger unit, an oxidation heat exchanger unit, a reduction production separation unit, an oxidation production separation unit, heat storage tanks, a solar furnace, a turbine, one or more blowers, or a combination thereof.

[0066] In embodiments, the heat source can be a furnace, a solar furnace, or a heat storage system.

[0067] In embodiments, the ionic liquid or molten salt comprises sodium, potassium, lithium, calcium, and magnesium carbonates, chlorides, sulphates, phosphates, or a mixture thereof.

[0068] The method of claim 15, wherein the molten salt comprises NaCl, KCl, MgCl₂, CaCl₂, LiCl, Na₂SO₄, K₂SO₄, Li₂SO₄, CaCO₃, Li₂CO₃, K₂CO₃, or a combination thereof.

[0069] In embodiments, the metal oxide (M_yO_x) comprises ceria (CeO₂), SrLaMnO₃, BaFeO₃, Fe₃O₄, FeAl₂O₄, CoFe₂O₄, CoFeAl₂O₄, perovskites, ceria derivatives, spinel ferrites, or a combination thereof. In some embodiments, the metal oxide is CeO₂.

[0070] In embodiments, the system is an industrial system further comprising a reduction production separation unit, an oxidation production separation unit, heat storage tanks, a solar furnace, a turbine, one or more blowers, or a combination thereof.

[0071] In embodiments, the industrial system comprises the process flow diagram of FIG. 24.

Example 1

Brief Non-Limiting Summation

[0072] This disclosure describes a new electric field (E-field) enhancement to enable low temperature, 2-step thermochemical gas splitting which decreases the operating temperatures and thus cost of solar thermochemical CO production from CO₂ reduction. In conventional solar thermochemical CO₂ splitting, STCS, a metal oxide is heated to its reduction temperature using concentrated solar thermal energy, liberating O₂; in a subsequent step, the reduced material is exposed to CO₂ which reoxidizes the active material releasing CO. Typically, STCS has high costs due to the high solar field necessary to achieve the high reduction temperatures of metal oxide reduction. We have developed a new technique that allows for the reduction of a metal oxide at significantly lowered temperatures, demonstrated

by reducing ceria at temperatures below 1000° C., approximately 400-600° C. lower than the traditional approach. By inducing an electronic double layer between the metal oxide and a high temperature electrolyte, a small applied voltage is amplified and provides the an ultra-high electric field that drives the reduction of the metal oxide through temporary changes in material thermodynamics. The electric field is removed, and the reduced metal oxide is then oxidized with CO₂, regenerating the starting material, and producing the desired CO. Lowering the reduction temperature allows for possible isothermal STCS operation, raising the efficiency of the system significantly due to removing the need for a temperature swing between reduction and oxidation steps.

Introduction/Background

[0073] Solar thermochemical gas splitting consists of two steps. The first is a thermal reduction of the active material producing an oxygen deficient material, which is then oxidized with either CO₂ or H₂O to regenerate the active material and produce either CO or H₂. Ceria is the current state of the art material due to its fast oxidation kinetics, high crystal stability, and repeated cyclability. The TCGS cycle using ceria is outlined below:



[0074] However, CeO₂ STGS is plagued by necessary high reduction temperatures (1200-1500° C.), which is accompanied by extraordinarily high solar field costs. Common methods of reducing reduction temperature, via lowering reduction energy, includes doping and co-doping the active material. However, these modifications can negatively impact the gas production efficiency by lowering the reaction energy making the oxidation less favorable.

[0075] Electrically driven reduction of CeO₂ has shown the ability to reduce ceria at lower temperatures on a microscale, Gao et al. The E-field induced reduction of ceria temporarily lower the oxygen vacancy formation, by inducing changes in the chemical potential of lattice oxygen. Using this phenomena, Gao et al. was able to reduce ceria at room temperature under the influence of only an E-field. Additionally, Li et al. showed that the electrical reduction of CeO₂ is reversible, by the “seesaw” behavior where the material is readily able to return to its original state by removing the applied potential. Because the change in the reduction enthalpy is temporary, under only the application of the E-field, and the underlying high reduction enthalpy of ceria is still present, the oxidation of ceria retains its thermodynamic favorability. However, these experiments were conducted in devices which are not scalable or applicable at the high temperatures needed, for example in tunneling electron microscopes, and on silicon wafers.

[0076] To generate the needed electric field, we utilize a molten salt facilitated electronic double layer. This electronic double layer is created due to the electrochemical mechanism of electrolyte gating. Where upon application of a potential to the electrolyte creates a build-up of positive charges in the electrolyte at the electrolyte-metal oxide interface. This induces a build up of negative charge in the metal oxide at the interface, completing the electronic double layer (EDL). The EDL acts as a parallel plate

capacitor, where the dielectric constant is on the order of nanometers, allowing for large specific capacitances, illustrated in Eq. 4,

$$C = \frac{\epsilon_0 A}{d}, \quad \text{Eq. 4}$$

[0077] Where C is the specific capacitance [F], ε₀ is permittivity of free space [8.85×10⁻¹² F/m], A is the area of the plates [m], and d is the distance [m] between them.

[0078] We can illicit high E-field strengths utilizing an electronic double layer (EDL), in order to temporarily lower the thermodynamics allowing for ceria reduction at lower temperatures, while not compromising its ability to split oxidizing gases into desirable products. By applying this E-field we can perform isothermal CO₂ splitting cycles at significantly reduced temperatures.

Non-Limiting Innovations

[0079] Non-limiting innovations are:

[0080] 1. The use of an applied potential to decrease the reduction temperature of solar thermochemical gas splitting materials;

[0081] 2. The generation of an electronic double layer to facilitate the charging of the active material and formation of a high strength electric field;

[0082] 3. The use of high temperature ionic liquids, including molten salts, as the medium for formation of the electronic double layer;

[0083] 4. Use of an electrode to facilitate charging;

[0084] 5. Decreasing the reduction onset temperature of solar thermal gas splitting to below 1000° C.

[0085] 6. Generation of O₂ from the redox active material with more than 1 mole of oxygen produced per 4 moles of electrons from the applied charge.

[0086] For the E-field enhanced CO₂ splitting system a metal oxide, such as porous ceria pellets are synthesized. The porous ceria material is made by ball milling CeO₂ with 20 wt % activated carbon, ethanol, and paraffin wax, 5 wt %, for 24 hours. After milling, the slurry is transferred to a crystallizer and the solvent is evaporated. Once dry, the material is ground, pressed into pellets and calcined at 1200° C. for 5 hours. After the porous pellets are synthesized, they are transferred into ZrO₂ coated Al₂O₃ crucibles. The pellets are submerged in molten salt. The electrical assembly is as follows: one electrode is submerged in the salt, the second is connected to the solid ceria material. Both electrodes are connected to a power source, such as a potentiostat. The crucible is loaded into a furnace, such as a high flux solar furnace or electrically heated tube furnace, where an inert purge gas can be used. The gas exhaust is connected to a CO/CO₂ separation system, such as a CO₂ trap and a cold trap, before reaching a mass spectrometer for composition analysis.

[0087] The cycles are performed first by heating the furnace to 900° C. with an Ar purge, then the potential, 0-4 V, is applied. During this step, if sufficient voltage is applied to the system, O₂ is released as the metal oxide is reduced. Then, once the material is fully reduced, the electric field is removed by withdrawing the potential, and the material is oxidized by charging the reactor with CO₂. In this step, the CO production initially spikes, as seen in a mass spectrometer confirming the production of CO. CO₂ dosing continues

until the CO measured returns to 0 indicating the material is fully oxidized, and then the material can be cycled again to repeat the reduction-oxidation cycle.

[0088] In embodiments, this disclosure comprises an electric field into the thermochemical cycle, and the utilization of the molten salt to facilitate the formation of the electronic double layer.

Non-Limiting Summation

[0089] Electrical enhancements of two-step thermochemical gas splitting are a new means to improve the performance of thermochemical gas splitting cycles by lowering the operational temperature to below 1000 C. In the process, the active metal oxide, MO_x , undergoes thermal reduction, at high temperatures under an applied potential, to form a non-stoichiometric oxide, $\text{MO}_{x-\delta}$; then the material is oxidized with H_2O , or CO_2 to regenerate the MO_x and generate high value products like H_2 or CO. The active material is submerged in an ionic liquid or molten salt enabling the formation of an electric double layer upon application of an applied potential and connection to an electrode in the liquid. Our electrical enhancement decreases reduction temperatures while maintaining high product conversion. The use of an electric field drives the reduction of metal oxides at temperatures below 1000° C.; further this approach facilitates the application of electric fields to induce solar thermal gas splitting at a macro scale necessary for solar thermochemical processes.

Non-Limiting New Aspects of the Disclosure

[0090] While modifications to metal oxides have been studied, the research has investigated means of altering active metal oxide materials using compositional or morphological effects. That is, introducing one or more additional element, through doping, into the metal oxide and changing the chemical formula or adjusting the morphology of active material to reduce diffusion and other transport mechanism effects. A non-limiting innovative aspect described herein is the ability to temporarily induce changes to the system's thermodynamics that favors the reducibility of the material by the application of an electric field. Additionally, as this behavior is a result of the applied potential, upon removal of the external stimulus the material maintains its original thermodynamics, eliminating the concern of lowering reduction enthalpy too far to provide insufficient energy to split H_2O or CO_2 .

[0091] Additionally, utilization of the molten salt induced electric double layer is also new as an addition to the thermochemical cycle. The use of an ionic liquid/molten salt allows for the entire thermochemical cycle to be performed isothermally or near isothermally, reducing the time and energy for the temperature swing.

Non-Limiting Advantages Over Technology

[0092] With our new E-field enhanced thermochemical cycle, thermal reduction of metal oxides can occur at temperatures well-below thermal only operation. We have demonstrated this through the reduction of cerium oxide at about 900° C., hundreds of degrees below the typical thermal only operating temperature range of 1200-1500° C. Additionally as the E-field enhancement affects only the reduction step, the active material maintains its high gas splitting performance. By providing a method to reducing the metal oxide

reduction energy while retaining the gas splitting efficiency allow for lower cost systems due to lower temperatures and materials of construction.

Non-Limiting Commercial Use

[0093] A non-limiting commercial application of this technology can be the ability to lower the reduction temperature of two-step thermochemical gas splitting while maintaining the high product conversion. By lowering reaction temperatures, the cost of the solar field can be significantly reduced, as well as the component cost due to lowered restrictions on construction materials. By lowering the reduction temperature, the overall solar to fuel efficiency is raised as a smaller temperature swing is needed, and even holds potential for isothermal operation.

[0094] Alternative methods to achieving lowering temperature two-step thermochemical fuel production includes materials alternation typically through the use of doped active materials with lower reduction energies. However, these materials suffer lowered oxidation efficiency as a result.

REFERENCES

- [0095]** 1. P. Gao, Z. Kang, W. Fu, W. Wang, X. Bai, E. Wang. *J. Am. Chem. Soc.* 2010, 132 (12), 4197-4201, DOI: 10.1021/ja9086616
- [0096]** 2. X. Li, K. Qi, M. Sun, Q. Huang, J. Wei, Z. Xu, W. Wang, X. Bai. *ChemCatChem* 2016, 8 (21), 3326-3329, DOI: 10.1002/cctc.201600974.
- [0097]** 3. R. Sharma, P. A. Crozier, Z. C. Kang, L. Eyring. *Philos. Mag.* 2004, 84 (25-26), 2731-2747, DOI: 10.1080/14786430410001671467

Example 2

Non-Limiting Disclosure Summary

[0098] The technology is a method to lower the operating temperature of solar thermochemical CO_2 splitting using an applied electric field. In conventional solar thermochemical CO_2 splitting (STCS), a metal oxide is heated to its reduction temperature using concentrated solar thermal energy, liberating O_2 , and in a subsequent step, the reduced material is exposed to CO_2 which re-oxidizes the active material releasing the desired carbon monoxide (CO). Conventional solar thermal CO_2 splitting systems are costly as they operate at high temperatures in the range of 1200-1500° C. This technology applies an electric field to an STCS system that uses ceria (CeO_2) as the metal oxide. By inducing an electronic double layer between the metal oxide and a high temperature electrolyte, a small applied voltage is amplified and provides an ultra-high electric field that drives the reduction of the CeO_2 through temporary changes in material thermodynamics. The electric field is removed and the reduced CeO_2 is then oxidized with CO_2 , regenerating the starting material, and producing the desired CO. The system has shown to reduce the CeO_2 at about 900° C. which is 300-600° C. below conventional STCS systems.

Non-Limiting Innovations

[0099] Use of an applied potential to decrease the reduction temperature of solar thermochemical gas splitting materials.

[0100] Decreasing the reduction onset temperature of solar thermal gas splitting to below 1000° C.

[0101] Generation of O₂ from the redox active material with more than 1 mole of oxygen produced per 4 moles of electrons from the applied charge.

Example 3

Non-Limiting, Exemplary Summary

[0102] Solar thermochemical CO₂ splitting (STCS) is plagued by high solar field costs due to the extraordinarily high temperatures (~1500° C.) required. In STCS, a reduction/oxidation active material, CeO₂, is thermally reduced to CeO_{2-δ} generating O₂ at ~1500° C.; then CeO_{2-δ} is re-oxidized by CO₂ to re-form CeO₂ and CO, a precursor to liquid fuels. Prior to this disclosure, there were no known methods to decrease the reduction temperature while maintaining high conversion of the CO₂ to CO; thus, projected solar thermal CO costs had stagnated.

[0103] This project describes the use of an electric field (E-Field) enhancement to lower the temperature of 2-step, STCS from >1400° C. to below about 1000° C. at a Faradaic efficiency of >100% where FE is defined as mol CO generated per 2 mol of electrons through the circuit, and to determine if the process is more cost effective than traditional STCS. Non-limiting new and surprising aspects described herein are as follows: (1) Optimize molten salt composition to enable E-field enhanced thermochemical CO₂ splitting below 1000° C., (2) Determine CO productivity and CeO₂ stability as a function of temperature, voltage, and partial pressure operating conditions, (3) Model the thermodynamics and efficiency of an industrial scale plant, and (4) Perform techno-economic analysis of a commercial plant.

Non-Limiting Technical Achievements

[0104] Described herein is the thermochemical CO production from CO₂ splitting at about 900° C. enabled by electronic double layer facilitated E-fields. This represents an unprecedented low temperature for solar thermochemical cycles. Na₂SO₄ and K₂SO₄/Na₂SO₄ eutectics were identified as promising molten salts. E-field enhanced CO₂ splitting experiments produced 397±6 µmol CO/g CeO₂ with an O₂ faradaic efficiency of 168±5% at 900° C. and a 95% confidence interval. Thermodynamic models described an increase in solar to CO efficiencies from ~0% in thermal only paradigm to ~40% in the E-field operation under reasonable system assumptions. Similarly, technoeconomic models described the use of the E-field would decrease CO production costs by ~50%, from \$1.49/kg CO to \$0.75/kg CO.

[0105] The results of this project provide a pathway to drastically decrease the cost of STCS. This mainly arises from the decreased onset reduction temperature for solar thermochemical CO₂ splitting from 1500° C. to below 1000° C. The decreased reduction temperature of E-field enhanced CO₂ splitting drastically decreases overall costs by driving down the number of heliostats required, the most expensive part of the CSP system, and the component identified by DOE to be the most critical in achieving price targets. Based on the detailed system thermodynamic and technoeconomic models, the use of E-field enhancement decreases the cost by 50%. Further, the lower temperature relaxes constraints on

construction materials required for operation above 1400° C., allowing less exotic and inexpensive ceramics and alloys to be used. Thus, this project successfully demonstrated the significant energy and economic efficiency improvements of the E-field enhanced STCS process.

BACKGROUND

[0106] The Solar Energy Technology Office has set a target of reducing the solar field cost of concentrated solar thermal industrial heat (STIH) systems by ~20% to achieve cost competitiveness with legacy and alternative energy technologies.^[1] Solar thermochemical CO₂ splitting (STCS) is a STIH process plagued by high solar field costs due to extraordinarily high temperatures (~1500° C.) required;^[2] in the processes CeO₂ is thermally reduced to CeO_{2-δ} generating O₂ in a high temperature thermal reduction step; then CeO_{2-δ} is oxidized by CO₂ to re-form CeO₂ and generate desired CO,^[3] which can be mixed with H₂ to produce liquid fuels.^[4] Prior to this disclosure, there were no known methods to decrease the reduction temperature while maintaining high conversion of CO₂ to CO on a macroscopic scale; thus, projected solar field costs have stagnated despite decades of research.^[5]

[0107] This project describes new electric field (E-Field) enhancement to low temperature, 2-step, solar thermochemical CO₂ splitting. In this process, described some embodiments in FIG. 1, a localized electric field (E-field) drives CeO₂ reduction at temperatures 100's of degrees below the thermal only process. An E-field can increase the reduction extent of CeO₂ at a microscopic scale.^{[6]-[8]} A non-limiting, surprising aspect of this disclosure is its application at the macroscale for STCS and the method for applying sufficiently large E-fields to alter system thermodynamics on the macro-scale at high temperatures.

[0108] An E-field in the electronic double layer between CeO₂ and molten salt under applied bias can increase the chemical potential of the O anions in CeO₂, driving the reduction reaction forward. In the investigated process, CeO₂ is immersed in a molten salt under a low positive voltage (~1 V), generating a massive E-field (>5 V/nm) in the resulting electronic double layer, similarly to a double layer capacitor. Thus, reduction driving high strength E-fields can be generated in large, macroscopic systems at low voltages. This is NOT an electrolytic process as limited current passes through the system; the only electrical energy input is that required to generate the double layer capacitor, which can potentially be recouped when the capacitor is discharged before the CO₂ splitting reaction. The applied voltage is selected to be below the electrochemical potential of the ionic liquid, preventing salt decomposition and parasitic energy loss.^[9]

[0109] Described herein is a process that is more cost effective than traditional STCS through. The described herein is the accomplishment of at least the following objectives: (1) Optimization molten salt composition to enable E-field enhanced thermochemical CO₂ splitting below 1000° C. (2) Determination of CO productivity and CeO₂ stability as a function of temperature, voltage, and partial pressure operating conditions. (3) Modeling of the thermodynamics and efficiency of an industrial scale plant. (4) Techno-economic analysis of a commercial plant.

Salt Composition Optimization (Section 1.0)

[0110] Described herein are non-limiting examples of the optimization of molten salt compositions, operation tem-

peratures, and voltage limits based on stability of the salt. In embodiments, Na, K, Li, Ca, and Mg carbonates, chlorides, sulphates, and their mixtures were considered. We identified Na_2SO_4 and as being well-suited for E-field CO_2 splitting. We were able to identify a salt composition which is stable under E-field conditions. We were able to identify a salt composition that is stable at operating temperatures, does not dissolve CeO_2 , and results in less than 10 mg/day/m² loss of CeO_2 .

Determine CeO_2 Stability in Salt Mixtures at Temperature (Section 1.1)

[0111] Non-limiting summation: CeO_2 pellets were synthesized and submerged in a matrix of salt mixtures at 900° C. for 48 hours and the mass loss of the CeO_2 was determined after the holding time. The following salts were examined: NaCl , KCl , MgCl_2 , CaCl_2 , LiCl , Na_2SO_4 , Li_2SO_4 , CaCO_3 , Li_2CO_3 , K_2CO_3 .

[0112] Non-limiting, exciting embodiments: Mass loss of CeO_2 in molten salt Na_2SO_4 was 17±18 mg/m²/day with no applied potential and 9±5 mg/m²/day with applied potential of 1 V. There was no detectable Ce in Na_2SO_4 melt via ICP-OES.

Results and Analysis

[0113] Ten different Na, K, Li, Mg, and Ca carbonate, chloride, and sulphate molten salts were investigated to identify a compatible salt- CeO_2 matrix for the E-field enhanced gas splitting process. These molten salt- CeO_2 combinations were evaluated based on the stability of the salt itself (e.g. volatilization, decomposition, and melting point compatibility with target operating conditions), in addition to interactions between the salt and CeO_2 active material (e.g. dissolution of CeO_2 and/or unfavorable reactions between CeO_2 and salt ions). In some embodiments, Na_2SO_4 was determined to be the most stable molten salt. Non-limiting, procedures and results are described below. One of ordinary skill in the art will be able to vary aspects by methods known in the art (e.g., for scaling, etc.).

CeO_2 Pellet Preparation and Stability in Ar

[0114] CeO_2 pellets were synthesized by ball milling CeO_2 and activated carbon (pore former) in 5:1 molar ratio with 5 wt % (binder) in ethanol for 24 hour. The CeO_2 mix is then dried and pressed into pellets (6.0±0.5 mm×3.0±0.5 mm) and calcined at 1200° C. for 6 hours. As a reference, a calcined pellet was held at 900° C. for 48 hours under air in a box furnace and had a measured mass loss of 0.00073 g or 1.2 mg/day/m². The slight mass loss is attributed to minor degassing and desorption of adsorbed water on the pellet. There were no visual changes to the pellet after the temperature dwell.

Salt Stability Under Air in Al_2O_3 (Alumina)

[0115] The stability of each molten salt and the molten salt- CeO_2 matrix was tested after prolonged hold at 900° C. Ten neat salts were tested: NaCl , KCl , MgCl_2 , CaCl_2 , Na_2SO_4 , Li_2SO_4 , CaCO_3 , Li_2CO_3 , and K_2CO_3 . The stability experiments were conducted as follows: 3 g of salt was dehydrated for ~24 hours, CeO_2 pellets were placed in alumina crucibles and embedded into the dehydrated salt and placed in a furnace for the temperature dwell. The furnace was heated from room temperature to 900° C. at a ramp rate of 10° C./min and held for 48 hours. After removal

of the samples from the furnace, the crucibles were weighed and the mass loss of the salt due to the temperature dwell is calculated. These salt experiments were conducted in triplicate, and the results of the mass loss of the salt are summarized in Table 1.

TABLE 1

Salt	Salt Mass Loss		
	Salt Mass Loss in air, %	Salt Mass Loss in inert, %	Salt Degradation
NaCl	-99.34 ± 0.06	-83.49	
KCl	-99.5 ± 0.2	-71.34	
MgCl_2	-59 ± 4	—	Yes, MgO
CaCl_2	-42 ± 5	—	
LiCl	-99.8 ± 0.1	—	
Na_2SO_4	-19 ± 40	-2.18	
Li_2SO_4	-28 ± 20	—	
CaCO_3	-43.58 ± 0.09	—	Yes, CaO
Li_2CO_3	-30 ± 4	—	Yes
K_2CO_3	-86 ± 20	—	

[0116] Of the ten salts investigated Na_2SO_4 , Li_2SO_4 , and CaCl_2 indicated reasonable stability in air, 19%, 28%, and 42%, respectively. Four of the salts had significant mass loss, NaCl , KCl , LiCl , and K_2CO_3 , lost at 99.34%, 99.5%, 99.8%, and 86% respectively, due to volatilization. Due to the possibility of unfavorable reactions in the presence of an oxidizer, O_2 , two chlorides underwent the same temperature procedure in an inert environment, more similar to the actual conditions of the gas splitting experiments. The results for these inert tests will be discussed herein. Three molten salt samples showed obvious signs of decomposition and/or the formation of unfavorable products; MgCl_2 , CaCO_3 and Li_2CO_3 . Examples of these three salts are shown in FIG. 2. MgCl_2 decomposed into what is believed to be MgO due to the thermal decomposition of hydrated MgCl_2 . CaCO_3 decomposed into CaO , as this decomposition occurs at 600-700° C., well below the dwell temperature. Li_2CO_3 decomposes into a blue solid. We note that K_2SO_4 does not melt at 900° C. and thus, while stable, is not suitable for the desired operating conditions.

Salt Stability in Inert (Argon)

[0117] As mentioned herein, based on the calculated mass loss of salts in experiments done in air, side reactions can be occurring in the high concentrations of O_2 causing the high mass loss of NaCl , KCl , LiCl , and K_2CO_3 . Additionally, because Na_2SO_4 had the lowest mass loss and, as will be discussed and the lowest CeO_2 loss, it was also examined. To test this, the 900° C., 48-hour dwell was performed again in a tube furnace under a purge stream of Ar. NaCl and KCl again experienced significant mass loss after the 48-hour temperature dwell of 83.49 and 71.3%, respectively. Na_2SO_4 was determined to have only 2.17% mass loss of the salt after the temperature dwell. K_2CO_3 was excluded from tests as previous preliminary results showed that K_2CO_3 continues to decompose into the blue solid even in an inert environment.

Mass Loss of CeO_2 in Molten Salt- CeO_2 Matrix

[0118] The mass loss of CeO_2 pellets following the 48 hour, 900° C. temperature dwell as also measured. The Na_2SO_4 - CeO_2 matrix experienced low levels of CeO_2 and Na_2SO_4 mass loss, 12±75 mg/day/m², and was identified as the best performing molten salt in Section 1.1.

[0119] The procedure to evaluate the mass loss of CeO₂ required the removal of ceria from the recrystallized molten salt to determine the final mass of ceria, and determine the mass loss of CeO₂ to the melt. After removing the Na₂SO₄—CeO₂ samples from the furnace, the CeO₂ is encapsulated in the recrystallized salt. The permeation of Na₂SO₄ into the pore space in porous CeO₂ pellets and subsequent solidification compromises the pellet structural integrity, after submerging in water to dissolve the Na₂SO₄ and remove the ceria from the crucibles. Therefore, upon removal from the furnace, the crucible-CeO₂—Na₂SO₄ sample is placed in a beaker of water until the salt surrounding the ceria is dissolved, allowing the ceria to be removed. Then, the pellet was placed in a volume of DI water, the pellet was allowed to fully dissolve, and the solution filtered to recover the ceria. The ceria and filter paper were dried and the resulting mass of ceria measured. Thus, the mass loss of ceria due to the Na₂SO₄ melt was determined based on the recovered ceria. Additionally, studies were performed by submerging uncycled CeO₂ pellets into an aqueous Na₂SO₄ solution for several days. The ceria pellets from these experiments showed no degradation from prolonged contact with the aqueous salt, indicating that the Na₂SO₄ affects only the structural integrity due to the salt permeation into pore space and recrystallization, not chemical changes. The mass loss of ceria, mg/m²/day are indicated in Table 2.

[0120] Temperatures above and below the target operating temperature of 900° C. were also examined. At 800° C., there was no melting of the salt, therefore, the salt would not be able to facilitate the formation of an electric double layer, so temperatures below 900° C. were not studied further. However, this does not mean that other, eutectic compositions which may be developed in the future could not facilitate this process. At 1000° C., there were high levels of salt loss after the 48-hour dwell, with an average of approximately 60% of Na₂SO₄ lost during the temperature dwells. This mass loss is attributed to salt vaporization. Due to this high level of salt loss, temperatures above 900° C. were also not investigated further.

TABLE 2

CeO ₂ Mass Loss, mg/m ² /day at temperatures in range 800-1100° C. with and without an applied potential				
	800° C.	900° C.	1000° C.	1100° C.
No Applied Voltage	No melt	17 ± 18 mg/m ² /day	9 ± 5 mg/m ² /day (*2/3 samples)	High decomp. expected
Applied Voltage of 1 V	No melt	16 ± 6 mg/m ² /day	High decomp. expected	High decomp. expected

[0121] Changes in pore size and morphology were conducted E-field experiments, as described in Section 1.2. The results from ICP indicate that there were no detectable levels of Ce in the melt corroborating the minimal loss of CeO₂ into the Na₂SO₄ melt.

[0122] The ceria mass loss of 17±18 mg/m²/day at the 95% confidence interval satisfies the target metric of 10 mg/m²/day. Therefore, we show a molten salt that has a sufficiently low degradation of CeO₂ at 900° C. with no applied potential.

System Stability Under Applied Voltages (Section 1.2)

[0123] The onset decomposition voltage of CeO₂/molten salt in molten salts at 800, 900, 1000 and 1100° C. were evaluated to identify salt and temperature combinations which are stable at 1V or higher from the stable salts described in some embodiments herein. CeO₂ stability analysis was repeated as described in Section 1.1 at the applied voltage of 1 V.

[0124] We evaluated salt compositions which cause less than 10 mg/day/m² loss into melt under applied voltage and cause minimal pore expansion under applied voltage compared to the non-voltage case.

[0125] Non-limiting, exciting embodiments: Mass loss of CeO₂ in Na₂SO₄ of 16±6 mg/m²/day at 900° C. with an applied potential of 1 V, this is equivalent to the target 10 mg/m²/day target at the 95% confidence level. There was no detectable Ce in Na₂SO₄ melt via ICP-OES

Results and Analysis

[0126] Na₂SO₄, was tested for voltage stability to complete the stability of the molten salt-CeO₂ matrix at temperature (900° C.) with an applied voltage. At 900° C. under an applied voltage of 1 V, CeO₂ had a mass loss of 16±6 mg/m²/day, summarized in Table 2.

[0127] Na₂SO₄ voltage stability at 900° C. and 1 V

[0128] Three 48 hour dwells, at 900° C. with an applied voltage of 1V, with ceria submerged in Na₂SO₄ were completed. A ZrO₂-coated Al₂O₃ boat was packed with ~1 g of Na₂SO₄ and a CeO₂ pellet. One Pt electrode was buried in the salt, and a second Pt wire was connected to the CeO₂ pellet. The crucible was then installed inside a horizontal tube furnace, with the electrodes connected to a potentiostat. The furnace was heated to 900° C. and held at temperature for 48 hours, while the potentiostat applied a voltage of 1 V. After the 48 dwell was complete, the furnace was cooled, the crucible removed, and the CeO₂ recovered as described in Section 1.1.

[0129] Under the applied potential, the mass loss of ceria was calculated to be 16±6 mg/m²/day to a 95% confidence interval, as shown in Table 2. Current, I (mA), is presented as a function of time under a constant applied voltage of 1 V shown in FIG. 4. The behavior of the measured current, initially high with a very rapid decrease, is characteristic of the charging of a capacitor, as expected. The peaks in the measured current are attributed to a shift in the wires during the experiment due to small laboratory vibrations. Mass loss of ceria was determined by recovering the pellets after testing, removing salt from the pellets, and determining the final mass of ceria that remained.

[0130] Cyclic voltammetry was also performed to investigate the electrochemical stability of Na₂SO₄ individually and the Na₂SO₄—CeO₂ system. The two systems were scanned from -2 to +2 V, recording the current as a function of the applied potential. The CV trace for Na₂SO₄ shows significant faradaic characteristics, specifically the high magnitude peaks around -2, -1, 1, and 2 V. The trace for Na₂SO₄+CeO₂ does not have the high faradaic peaks and has an overall lower current magnitude. While not exactly matching the rectangular characteristic shape of electronic double layer or pseudo-capacitor CV traces, the salt-ceria system looks more similar to those systems than the salt only pattern. The lack of peaks in the CV trace of the salt-ceria system indicates that the CeO₂ is not conducive for the

Na_2SO_4 decomposition reaction. Thus, a kinetic barrier is likely present preventing decomposition and extending the operational range.

[0131] The ceria mass loss of $16 \pm 6 \text{ mg/m}^2/\text{day}$ at the 95% confidence interval satisfies the target metric of $10 \text{ mg/m}^2/\text{day}$. Thus, these findings indicate the identification of a molten salt that has a sufficiently low degradation of CeO_2 at 900° C . with an applied potential of 1 V. ICP-OES was used to evaluate whether Ce dissolved into the Na_2SO_4 melt. The Ce content was below the detection limit of the instrument, validating that there was very low mass dissolution of CeO_2 into the salt, further demonstrating the stability of the system.

Changes in Pore Size and Morphology Characterized by SEM

[0132] To determine the effects of salt on pore size and morphology due to the applied voltage during experiments, pellet morphology was investigated using scanning electron microscopy. The highly porous structure of the CeO_2 pellets required stabilization by an epoxy encapsulation before imaging to allow the pellets to be cut without destroying the pore structure. This was done with both the pre- and post-cycling pellets. After encapsulation and curing, the epoxy pucks were polished to expose a cross-section of the pellets by removing surface layers from the ceria pellets. After polishing, the epoxy- CeO_2 pucks were carbon coated to prevent charging and imaged using scanning electron microscopy (SEM). A comparison of the pore structures before and after an applied potential are shown in FIG. 6. Ceria is visible as light gray with the epoxy or void space composing the darker gray regions. After the applied potential and submersion in Na_2SO_4 , cerium oxide forms spherical CeO_2 particles/regions while the salt recrystallizes within the pellet material. This is shown via EDS, FIG. 7, showing light gray sphere consisting of only Ce and O, and the darker gray recrystallized structures containing Na, S, and O.

[0133] The ceria mass loss of $16 \pm 6 \text{ mg/m}^2/\text{day}$ at the 95% confidence interval achieved the target metric of $10 \text{ mg/m}^2/\text{day}$. Additionally, the EDS images corroborates that the effects on structural integrity due to the Na_2SO_4 recrystallizing within the pore structure when the materials are cooled. Combined with the in-situ stability results, e.g. stable electrochemical behavior, and the absence of CeO_2 in the melt, these results indicate the identification of a molten salt that has a low degradation of CeO_2 at 900° C . with an applied potential.

CO Productivity and Selectivity (Section 2.0)

[0134] Described herein is the evaluation of CO production capacity of the E-field enhanced CO_2 splitting of CeO_2 with the molten salt identified herein. We obtained repeatable O_2 and CO production at 900° C . with a Faradaic efficiency of >118%.

[0135] We also evaluated CO produced from CeO_2 after reduction at $<1,000^\circ \text{ C}$. with a goal of achieving overall faradic efficiency of >100% and identified operating conditions for CO production of $>150 \mu\text{mol/g}$ CeO_2 after reduction at $<1000^\circ \text{ C}$. with a Faradaic efficiency of >100%.

[0136] Construct E-field thermochemical CO_2 splitting reactor (Section 2.1)-designing and constructing an E-field reactor including gas dosing manifold, furnace, sample

holder, potentiostat, gas analytics, and data acquisition system. We designed and constructed a dedicated reactor to perform the electrically enhanced CO_2 splitting reactions.

[0137] Non-limiting exciting aspects: Experimental reactor constructed and successfully demonstrated. Reactor couples the ability to measure O_2 and CO generation, allowing for measurement of reduction and oxidation, and supports electrical measurements, cyclic voltammetry and applied electric fields via potentiostat to characterize electrochemical behavior and operational performance.

Results and Discussion

[0138] The dedicated E-field enhanced CO_2 splitting reactor design has been completed, as shown for example in FIG. 8. The system includes an automated gas dosing manifold, tube furnace reactor, and an in-line Residual Gas Analyzer (RGA) mass spectrometer to measure the composition of the exhaust gas.

[0139] To perform gas splitting experiments, a 1 in OD alumina work tube is housed in a high temperature, horizontal tube furnace. The tube furnace allows for a closed gas environment to be maintained, which is crucial to both driving the redox reactions forward, and analysis of the exhaust gas. The constructed cells are loaded into the work tube, and electrode leads are attached to Pt wires to connect to the electrochemical workstation. The Pt wires are contained in a double bore alumina tube to prevent a short-circuit. Once connected to the electrical leads, the samples cells are loaded into the tube furnace and centered into the middle of the heating zone. The workstation is used on the potentiostat settings to apply a constant voltage for the duration of the reduction phase.

[0140] Feedstock gases are supplied via compressed gas cylinders. Ultra high purity Ar (UHP Ar) and CO_2 are used to supply the CO_2 splitting experiments, and a 1% O_2 /1% He/98% N_2 (1% (2) and CO— CO_2 mix (0.01% CO, balance CO_2) are used to calibrate the O_2 and CO signals for analysis. The gases are controlled by an automated gas handling system of MFCs, upstream pressure controller, and data acquisition system. Exhaust gases are passed through a CO_2 trap before reaching an MKS Cirrus 2 Mass Spectrometer or SRS100 RGA. The CO_2 trap removes unreacted CO_2 before reaching the detector such that the quantity of CO produced is not obfuscated by CO_2 fragmentation. The cold trap is used to condense any volatilized compounds from the reactor so as not to obstruct downstream lines.

[0141] FIG. 9 shows the different parameters that are maintained during the experiment. The experiments were performed by first heating the furnace to 900° C . under an inert purge gas, then the potential is applied via potentiostat, inducing the electric field. During this step, with sufficient voltage applied to the system, the formation of O_2 is observed as the metal oxide reduced. Then, to reoxidize the material and form CO, the applied potential is removed, and the system is dosed with CO_2 . In this step, the CO signal spikes, indicating the production of CO. Once the material has been reoxidized, the material was be cycled again. FIG. 9 shows the results from 4 consecutive cycles as a demonstration of the reactor.

E-Field Thermochemical CO_2 Splitting Capacity (Section 2.2)

[0142] We show the quantity of O_2 and CO produced at 800, 900, and 1000° C ., and applied voltages of 0, 0.5, 1, 1.5

and 2 V in stable salt mixtures and demonstrate O₂ faradaic efficiency of greater than 100%. Voltage was applied by a potentiostat, which concomitantly measured any current. O₂/CO production was measured by an in line residual gas analyzer mass spectrometer. Faradaic efficiency was calculated from the current and the CO and O₂ generated.

[0143] We determined the CO production as function of reduction temperature, oxidation temperature, reduction p_{O₂}, and applied voltage.

[0144] Non-limiting, exciting embodiments: (1) Repeatable ceria reduction and oxidation by CO₂ under application of applied voltage and (2) CO production after 2 V reduction.

Results and Analysis

[0145] Gas splitting experiments were performed to determine the reduction of ceria at 900° C., characterized by the evolution of O₂, and its capabilities to split CO₂ into CO with an applied potential of 1-2 V.

Experimental Setup

[0146] CO₂ splitting experiments were performed in reactor described in the previous section. Like previous experiments, sample cells were built as follows: a ZrO₂-coated Al₂O₃ boat was filled with 1-2 g of Na₂SO₄ and a CeO₂ pellet. The electrode, Pt foil connected to Pt wire, was buried in the salt, and a second Pt wire was connected to the CeO₂ pellet using Pt foil and a conductive Pt adhesive. The ceria cells are illustrated in FIG. 10. The crucible was housed inside the reactor described herein.

CeO₂ Reduction (O₂ Generation) and Re-Oxidation (CO₂ Splitting)

[0147] The procedure of the experiments were as follows: after loading the crucible into the furnace, the system was

leak tested with Ar, then the reactor, CO₂ trap, and CO₂ trap bypass are purged of air using an Ar purge gas. Next a calibration curve was generated using mixtures of O₂ from a 1% O_{2/1}% He/balance N₂ gas mix. Finally, the system was heated to 900° C. in Ar. After reaching temperature, the exhaust was switched from a bypass to the CO₂ trap. The workstation was connected to the electrodes. The E-field was generated with the application of 1-4 V to the system using the potentiostat, such that the resulting current of the system is measured as a function of time.

[0148] Table 3 shows the results of the 900 and 950° C. isothermal and non-isothermal redox cycles conducted with 1-4 V of applied potential. While the condition of each redox cycle varies, the procedure remained the same. The furnace is heated to reduction temperature either 900 or 950° C., the field is applied with 1-4 V for 60 minutes, the system is then purged with Ar, and the furnace is heated/cooled to the oxidation temperature and CO₂ is dosed in for another 60 minutes. The system is then purged again, and the next condition is tested. As seen in Table 3, temperatures below 900° C. are not suitable for using the Na₂SO₄ electrolyte as this is below the salt's melting point. Temperatures above 950° C., the in Table 7, are also not usable, as high levels of salt decomposition were observed, as mentioned Section 1.1. Using the restrictions on the operating temperatures, four different combinations of reduction temperature, T_{red}, and oxidation temperature, T_{ox}, have been identified as possible working conditions. Applied potentials of 1, 2, 3, and 4 V were tested at the four different temperature regions, and the resulting O₂ and CO production and faradaic efficiencies are listed. At all four temperature conditions, an applied potential of 1 V is insufficient to induce the necessary electric field needed to reduce ceria at T<1,000° C.

TABLE 3

O ₂ evolution at voltages 1-3 and variable T _{red} and T _{ox} .					
T _{red} = 800° C. T _{red} = 850° C. T _{red} = 900° C. T _{red} = 950° C. T _{red} = 1000° C.					
T _{ox} = 800° C.	T _{red} < T _{m,Na₂SO₄}	T _{red} < T _{m,Na₂SO₄}	T _{ox} < T _{m,Na₂SO₄}	T _{ox} < T _{m,Na₂SO₄}	T _{red} > T _{decomp}
T _{ox} = 850° C.	T _{red} < T _{m,Na₂SO₄}	T _{red} < T _{m,Na₂SO₄}	T _{ox} < T _{m,Na₂SO₄}	T _{ox} < T _{m,Na₂SO₄}	T _{red} > T _{decomp}
T _{ox} = 900° C.	T _{red} < T _{m,Na₂SO₄}	T _{red} < T _{m,Na₂SO₄}	1 V insufficient voltage	1 V insufficient voltage	T _{red} > T _{decomp}
			2 V: 560 μmol O ₂ /g CeO ₂ , FE = 186%	2 V: insufficient voltage*	
			3 V: 1094 μmol O ₂ , FE = NA	3 V: 590 μmol O ₂ /g CeO ₂ , FE = NA	
			4 V: 3880 μmol O ₂ /g CeO ₂ , FE = 168%, 397 μmol CO/g CeO ₂ , FE = 9%	4 V: 3060 μmol O ₂ /g CeO ₂ , FE = 172%, 469 μmol CO/g CeO ₂ , FE = 5%	
T _{ox} = 950° C. T _{red} < T _{m,Na₂SO₄}	T _{red} < T _{m,Na₂SO₄}	1 V insufficient voltage	1 V: insufficient voltage	1 V: insufficient voltage	T _{red} > T _{decomp}
		2 V: 330 μmol O ₂ /g CeO ₂ , FE = 118%	2 V: 397 μmol O ₂ , FE = 132%		
		3 V: 447 μmol O ₂ /g CeO ₂ , FE = NA	3 V: insufficient voltage*		

TABLE 3-continued

O ₂ evolution at voltages 1-3 and variable T _{red} and T _{ox}				
T _{red} = 800° C.	T _{red} = 850° C.	T _{red} = 900° C.	T _{red} = 950° C.	T _{red} = 1000° C.
T _{ox} = 1000° C.	T _{red} < T _{m,Na₂SO₄}	T _{red} < T _{m,Na₂SO₄}	T _{ox} > T _{decomp}	T _{ox} > T _{decomp}

Faradaic Efficiency:

[0149] Faradaic efficiency (FE) is calculated for the reaction that generates O₂. FE is calculated according to:

$$FE = \frac{nFm}{Q} = \frac{nFm}{I \times t} \quad \text{equation 1}$$

where n is the number of electrons transferred to produce one mole of product, F is Faraday's constant, 9.65×10⁴ C mol⁻¹, m is the moles of product formed, Q is the total charge, which can be found for this system by integrating the measured current over time of the reaction. The FE for O₂ generation is >100% and for CO generation is >0% for all conditions where reduction/oxidation were observed and measured.

[0150] An important finding from the numerous experiments was the significant impact caused by the aging of the electrical components, specifically the Pt electrodes. With repeated use, the Pt wires are reacting with the salt and develop a higher resistance over time affecting the applied voltage that is eventually delivered to the system. Therefore, a larger voltage needed to be applied with older components compared to newer Pt wires and electrodes. This need for higher applied voltages appeared to have a negative effect on the stability of the Na₂SO₄, in some cases causing salt decomposition, evolving some O₂ from the salt itself. However, with the early experiments showing the successful reduction at low voltages, the salt stability tests, and the successful CO production, the ceria is likely the key participant in the electrically enhanced reduction and as the sole participant in the CO₂ splitting reaction even if some O₂ has evolved from the NaSO₄.

Optimization of CeO₂ Morphology (Section 2.3)

[0151] Summary: This subtask evaluated the morphological effects of the active CeO₂ and the electrode and including three different CeO₂ porosity, electrode size, and material. All examinations were conducted at the conditions from Section 2.2 which provided the maximum CO production. We evaluated optimal pellet morphology and electrode morphology.

[0152] Non-limiting, exciting aspects: Higher porosity results in higher CO and O₂ production and efficiency

Results and Analysis

[0153] The performance of five different porous ceria materials were synthesized. Increasing the porosity improves the gas splitting performance of the material. In tests of the electrode, a square Pd foil of approximately 0.5-1 cm showed the best performance. It is noteworthy that this was the largest electrode tested, suggesting that even large electrodes may further improve performance as capacitors are limited by the size of the smallest electrode.

Synthesis

[0154] Five different porous ceria materials were synthesized using a solid-state ball mill process. Activated carbon was mixed with CeO₂ in various ratios to increase the porosity of the final CeO₂ pellets. CeO₂ and carbon were mixed in ratios of 1:0, 7:1, 5:1, 4:1, and 3:1. All batches were mixed with 5% wt. binder (paraffin wax) and ethanol as a milling solvent, and were ball milled for 24 hours with ZrO₂ and YSZ (yttrium stabilized zirconia) milling media. After milling, the material was transferred to clean crystallizers to evaporate the solvent before being ground and pressed into 0.6×3 mm (diameter by height) pellets. The pellets were calcined at 1200° C. for 5 hours.

Porous CeO₂ Pellet Densities

[0155] As an initial method of characterizing the different ceria materials, the densities were determined for all five materials, as shown in FIG. 11. A trend emerges that as the quantity of carbon (pore former) increases, the density decreases. The 3:1 presents an interesting deviation from the trend by having a density larger than that of the 4:1. Without wishing to be bound by theory, the presence of too much pore former is unable to support the pore structure during annealing, and thus it collapses before the particles sinter.

[0156] The examination of performance of the different CeO₂ pellets was completed by comparing the quantity of oxygen they produce. FIG. 12 shows that the more porous CeO₂ material (5:1) outperformed the pure CeO₂ material, by increasing the quantity of O₂ evolved by 51.1 μmol O₂/g CeO₂. The improved performance is attributed to the fact that oxygen vacancies form at the CeO₂-molten salt interface, and higher porosity creates more available surface area for this interface. Due to aging of the platinum electrodes, as discussed in Section 2.2 experimental conditions were changed between testing the pure CeO₂ and the 3:1 CeO₂:C ratio. Comparing the 5:1 and 3:1 porous materials at consistent voltages, e.g. 4V, we can conclude that the more porous 3:1 material was capable of more O₂ reduction, as expected with the higher levels of surface area. Note, the high levels of O₂ measured, is partly due to O₂ produced from the decomposition of Na₂SO₄ at the 4V level, as discussed in Section 2.2. While the more porous ceria pellets are capable of higher levels of reduction and therefore, oxidation, the difficulties associated with synthesizing stable pellets makes the 5:1 a preferred material.

SEM Imaging of Different Pore Morphologies

[0157] In order to investigate the pore morphologies of the different porosity materials, the pore structures were characterized as a function of ceria to pore former ratios. The synthesized pellets were encapsulated in epoxy to stabilize the pore structure during polishing. After polishing, the epoxy-CeO₂ pucks were carbon coated and imaged using scanning electron microscopy (SEM). A comparison of the

various porosity materials pore structure is shown in FIG. 12. Ceria is depicted in light gray with the epoxy or void space (pores) making up the darker gray regions. As the ratio of CeO₂ to pore former decreases (CeO₂>7:1>5:1>4:1>3:1) the expected porosity of the final pellets increases. This is confirmed by visual inspection of the pellets where as the CeO₂:C ratio decreases, more dark gray areas are visible and are larger.

Electrode Composition and Geometry

[0158] The material and geometry of the electrode were also examined. To select the composition of the electrode material, the material must sustain the operating temperatures (900° C.), have good electrical conductivity, and withstand the corrosivity of molten Na₂SO₄. Based on the first two criteria platinum, nickel, and nichrome were studied due to their high melting points and good electrical conductivity. To test the chemical inertness of the different electrode materials, pieces of Pt, Ni, and nichrome were submerged in Na₂SO₄ at 900° C. for 24 hours. As shown in FIG. 13, the Pt in both forms emerged from the corrosion test with no visual damage; however, both the Ni and nichrome experienced obvious corrosion due to the molten salt.

[0159] To determine the best form of Pt electrodes to use, several factors were compared including: electrochemical performance, and quality and ease of cell construction. The larger Pt foil electrodes afford easier cell construction, and a sturdier cell, i.e. the electrode remains submerged in the salt during sample loading. The larger electrodes also yield better cyclic voltammograms, with fewer peaks and a more consistent curve. The size of the electronic double layer (EDL) is also determined by the surface area of the electrode submerged in the salt, so a larger surface area is favorable to create a larger field effect.

Stability of CeO₂ Under Cycling (Section 2.4)

[0160] Non-limiting Summation: This subtask successfully demonstrated 10 redox cycles of E-field enhanced thermochemical CO₂ splitting, and determined CO production capacity. Cyclability was determined by measuring CO produced and faradaic efficiency using similar techniques as outlined in Section 2.2.

[0161] We show 10 redox cycles and determination of cyclability based on faradaic efficiency and generated CO production capability.

[0162] Non-limiting, exciting aspects: Production of 397±6 μmol CO/g CeO₂ at 900° C. and 4V and O₂ faradaic efficiency of 168±5% at 900° C. and 4V.

10 Redox Cycle Experiment

[0163] A 10-cycle demonstration was undertaken to investigate the cyclic performance of the electrically enhanced CO₂ splitting. The redox cycles occurred as follows: the sample was synthesized and loaded into the reactor as described previously; then the furnace was heated to 900° C. and held at a constant temperature for the duration of the experiment. Each redox cycle began with an applied potential of 4 V being applied to the system for 60 minutes with an Ar purge flowing through the system. Then a 60 minute purge of Ar was used to remove any evolved O₂, then the CO₂ was dosed into the system at 20 sccm for 60 minutes, followed by a 60 minute Ar purge. The cycle was then

repeated, beginning with the application of the E-field. FIG. 14 shows the O₂ and CO generation for 10 cycles. The O₂ generation is continuous over the 10 cycles. The first 6 cycles are excluded from analysis to remove the break-in period of the thermochemical material. After 6 cycles, the system reaches an average of 3,880 μmol O₂/g CeO₂ and 397 μmol CO/g CeO₂ over the last 4 cycles. The material also shows sustained oxidation capabilities with CO generation over all cycles. The first cycle is believed to be inflated due to N₂ gas present in the lines. Without wishing to be bound by theory, the non-closer of the mass balance, which would predict a 1:2 O₂:CO ratio, arises from gas transport limitations as the reactor does not allow for good CO₂ contact with the CeO₂. However, more advanced reactor designs can remedy this issue, such as CO₂ bubbling in the melt or periodic removal of the CeO₂ from the melt during reoxidation. This demonstration shows that the electrically enhanced ceria reduction can be performed repeatedly.

Faradaic Efficiency:

[0164] Faradaic efficiency (FE) was calculated for the reaction that generates O₂. FE is calculated according to:

$$FE = \frac{nFm}{Q} = \frac{nFm}{\int I dt} \quad \text{Equation 2}$$

[0165] where n is the number of electrons transferred to produce one mole of product, F is Faraday's constant, 9.65×10⁴ C mol⁻¹, m is the moles of product formed, Q is the total charge, which can be found for this system by integrating the measured current over time of the reaction. Using this equation, the FE for O₂ generation for the 10 redox cycles is calculated and shown in FIG. 14. As the faradaic efficiency is dependent on the quantity of O₂/CO produced, the first 6 cycles have been excluded. Cycles 7-10 show an average FE_{O₂} of 169% and FE_{CO} of 9%.

System Level Model (Section 3.0)

[0166] A thermodynamic system model of a 10 MW_{th} plant based on E-field enhanced solar thermochemical CO₂ splitting was constructed and evaluated to determine the thermochemical efficiencies of the process and the most efficient operating points.

[0167] We constructed a system model of E-field Solar thermochemical CO₂ splitting plant; and identified thermodynamic optimal operating points necessary to achieve >25% thermodynamic efficiency.

Construct System Model of E-Field Solar Thermal Plant

[0168] Non-limiting Summary: A thermodynamic system model of E-field solar thermal plant based on ceria/molten salt was constructed. It accounted for heliostat field efficiency, e-field reactor, heat exchangers, gas separation, and E-field enhanced CO₂ splitting thermodynamics.

[0169] Non-limiting, exciting aspects: MATLAB thermodynamic model of the non-E-field system constructed; Demonstrated ~25% efficiency for CeO₂ CO₂ splitting after reduction at 1500° C. but ~0% after reduction at 900° C. in thermal only mode; Demonstrated high, >25% solar to CO efficiency when using E-field at 900° C.; T_{red}; P_{red}; and

potential have the most significant impact on the overall total efficiency. However, at sufficiently high voltages (>2 V) the effect of T_{red} and P_{red} and less pronounced.

Results and Analysis

MATLAB Code Overview

[0170] A thermodynamic system model was constructed of a conventional (i.e. non-E-field) and E-field modified solar thermochemical plant in MATLAB. A mass and energy flow diagram of the system is shown in FIG. 15. The model takes in the partial molar entropies and enthalpies of the active material, i.e. CeO_2 , reduction temperatures, and assumptions about plant operation, i.e. solid/solid and gas/gas heat recuperation, optical efficiency, O_2 pumping efficiency etc., and uses mass and energy balances to calculate the solar heating requirements needed to produce 1 mol of CO. The material is assumed to move in a counter-current gas/solid contacting pattern, where the reduced solid entering the oxidation reactor is in thermodynamic equilibrium with the CO/CO_2 mixture exiting the oxidation reactor (thus maximizing the CO/CO_2 ratio) and the oxidized solid exiting the oxidation reactor is in equilibrium with the CO_2 enter the oxidation chamber. CO_2 thermolysis provides the effective O_2 partial pressure for establishing equilibria with the solids. The amount of solid which must be heated/cooled is scaled to achieve 1 mol of CO production. The E-field effects were accounted for by change in free energy of a polarizable material (CeO_2) in an electric field, which was then added to the thermochemical free energy. The E-field was modeled as a double-layer capacitor, where the double layer thickness was taken to be the diameter of Na_2SO_4 . A specific surface area of the material was assumed. The energy required to charge the double layer capacitor was calculated from the total material required to generate 1 mole of CO, the specific surface area and the applied potential. It was assumed that the energy of capacitor could not be recovered. It is noteworthy, however, that this assumption is a worst-case scenario.

[0171] The amount of CO_2 needed to move through the system can be calculated from the CO/CO_2 ratio exiting the oxidation reactor. The heat required to heat CO_2 from an assumed ambient CO/CO_2 separation system to the oxidation reactor is calculated, discounted for gas/gas heat exchange coming from the CO/CO_2 mix. CO/CO_2 separation is assumed to occur at room temperature, with a heat requirement calculated from the free energy of mixing and inflated by a heat to work efficiency (10%). On the solids side, the heat required to heat the oxidized CeO_2 to the reduction reactor is calculated from the heat capacity and discounted for solid-solid heat exchange. The reduction enthalpy is calculated from the partial molar enthalpy. Excess heat which is not recuperated is assumed to be available for CO_2 heating, and other auxiliary work, such as pumping and CO_2/CO separations. After accounting for all chemical plant heat requirements, we determine the solar input required assuming an optical efficiency (90%), solar irradiance, and concentration factor (3000), giving a final solar input. The solar to CO efficiency is calculated as the heating value of CO over the total solar input. For a given reduction temperature, the oxidation temperature is optimized to identify the most efficient operating point.

Thermodynamic Model Results

[0172] CeO_2 reaches a maximum solar to CO efficiency of ~24% after reduction at 1500° C. , but it achieves ~0% efficiency after reduction at 900° C. As shown in FIG. 16, the maximum efficiency after a 1500° C. reduction occurs at a reoxidation temperature where the auxiliary heat requirements are balanced with the axillary heat benefits. These results are unsurprising as it is known that CeO_2 performs well under high temperature reduction. The poor performance at 900° C. arises from the minuscule oxygen non-stoichiometry achieved. As shown in FIG. 17, the CeO_2 does not reduce at 900° C. and therefore cannot act as an O storage agent. This finding indicate that any CO generated in E-field experiments are not attributable to the inherent CO production capacity of CeO_2 without the E-field.

[0173] Unlike the conventional thermal only approach, the model predicts high theoretical solar to CO efficiency after reduction at 900° C. with 2V. Under these conditions, the efficiency reaches almost 50%, as shown in FIG. 18. The system can be best operated under isothermal conditions because the solid-solid heating becomes a significant energy penalty if a temperature swing is introduced and substantial change in the non-stoichiometry can be induced by the application/removal of the potential. Aside from the energy cost of reduction, the major energy inputs arise from O_2 removal (i.e. providing a low partial pressure) and generating the E-field.

Sensitivity Analysis

[0174] Sensitivity analysis of six model variables on the solar to CO efficiency has been performed to determine the most influential variables on E-field system. The six variables are as follows: reduction temperature and pressure (T_{red} and P_{red}), applied potential (V), solid-solid efficiency (e_{ss}), gas-gas efficiency (e_{gg}), and pump efficiency (n_{pump}). For the cross analysis, the base case was taken to be $T_{red}=900^\circ \text{ C.}$, $P_{red}=10 \text{ Pa}$ (10^{-4} bar), $V=2 \text{ V}$, $e_{ss}=e_{gg}=50\%$, and $n_{pump}=5\%$, which are the conditions shown in FIG. 18. Selected pairs of variables were varied according to a pre-selected range of conditions shown in Table 4. A selection of the sensitivity relationships are shown in FIG. 19. Highlights from this sensitivity analysis show the most influential variables are the T_{red} , P_{red} , and potential. At sufficiently high applied potentials, the effect of T_{red} and P_{red} decrease, as the total efficiency is very similar for $V > 2\text{V}$. Comparing the relationship between T_{red} and P_{red} at high temperatures and low pressures the impact of changing the conditions is significantly decreased. These results indicate that, unlike the conventional operation, heat recuperation is much less important, particularly solid-solid heat recuperation which is difficult to implement.

TABLE 4

Variables	Conditions for Sensitivity Analysis					
	T_{red} ($^\circ \text{C.}$)	800	850	900	950	1000
P_{red} (Pa)	1	10	50	100	200	2.53
Potential (V)	0	0.5	1	1.5	2	2.53
e_{ss} (%)	0	0.25	0.5	0.75	1	
e_{gg} (%)	0	0.25	0.5	0.75	1	
n_{pump} (%)	0.01	0.05	0.1	0.2	0.4	

Optimization of E-Field Solar Thermal Plant Based on Thermodynamic Model (Section 3.2)

[0175] Non-limiting Summary: The thermodynamic results from Section 2 were incorporated into the thermodynamic model. The thermal and electrical efficiency of the system were determined as a function of operating points (reduction and oxidation temperature) and system parameters (e.g. gas-gas heat exchanges). The optimal operating points were identified.

Results and Analysis:

[0176] The CO production capacity per cycle, ~400 $\mu\text{mol/g}$ CeO_2 were coded into the thermodynamic model. This was accomplished by setting the reduction extent of the CeO_2 to 0.072 based on the experimentally determined CO production capacity of Section 2. Here, 4 V of applied potential were used as this corresponded to the applied potential in the experiments. The results are shown in FIG. 20. The largest impact on solar to CO efficiency arises from the pumping efficiency. When the pumping efficiency decreases from the base case ($T_{red}=900^\circ \text{ C.}$, $P_{red}=10 \text{ Pa}$ (10-4 bar), $V=4 \text{ V}$, $e_{ss}=e_{gg}=50\%$, and $n_{pump}=5\%$) to only 1%, the efficiency dropped to ~21.5%. This is consistent with the findings from the previous sensitivity analysis. Overall, these results indicate the continued high solar efficiency provided by the E-field concept and the validity of the mechanisms employed in the fully theoretical analysis.

Techno-Economic Analysis (Section 4.0)

[0177] Non-limiting Summary: This Task completed techno-economic analysis of E-field enhanced CO_2 splitting at a commercial scale (10 MW_{th}) to determine the cost of CO per kilogram. The results were compared to the economics of a conventional solar thermal thermochemical CeO_2 cycle. Waterfall and sensitivity analysis identified which aspects will further decrease operational costs. We identified operating conditions which achieve <\$2.50/Kg CO costs.

TEA of E-Field CO Splitting (Section 4.1)

[0178] Non-limiting Summary: Using the system model from Section 3, this subtask built a TEA analysis for the E-field enhanced thermochemical CO_2 splitting system using CeO_2 as the active material. Component costs of the model were explored to examine the effects of various operating points and relative costs. The overall cost per kg of CO was determined. DOE projected costs for heliostat, depreciation, etc. were used as outlined in the DOE's H₂A analysis charts.

[0179] Non-Limiting, exciting aspects: Final predicted cost of \$0.75/kg CO with E-field enhanced process. Final predicted cost of \$1.49/kg CO in the conventional model

Results and Analysis

[0180] The progression from the thermodynamic system level model, completed in Section 3.0, to the leveledized cost of CO through an economic cost analysis is outlined in FIG. 21. Section 4.1 is divided into the following five steps: thermodynamic model, solar field sizing, plant process component sizing, production analysis, and cost analysis. The process was reviewed by an expert in solar thermal TEA, and deemed appropriate. Thermodynamic model output was taken from Section 3.0 and is therefore not repeated here.

Solar Field Sizing

[0181] Solar field design occurred in the opensource SolarPILOT software. The constant design points included: 10 MWt of power into the receiver aperture, 650 W/m² DNI, optimization using the sun position at the equinox, and site location in Phoenix, AZ. The simulations were run five days out of the year every fourth hour of the day over a one-year period utilizing DNI typical meteorological day (tmy2) data from Phoenix, Arizona, USA¹. Effects of shadowing/blocking are considered in the simulations. Heliostats are sorted for selection by the total power delivered to the receiver over the simulation set, laid out in a radial stagger method, and spaced to eliminate blocking. The solar field is composed of a central tower that has a receiver at the highest point and a semi-circular field of reflective heliostat mirrors. The heliostat layout was limited to 180 degrees to eliminate the need for multiple, rotating, or cylindrical receivers.

[0182] The receiver type was selected as a cavity with an elliptical acceptance shape. Sizing of the receiver absorptive surface (aperture) was based on the results of the thermodynamic model with a concentration ratio of 3,000, which included effects of re-radiation and convection. The calculated E-field and no field model aperture radii were 1.16 m and 1.23 m, respectively. SolarPILOT constructs a rectangular overall receiver target area, thus the input was of a square with sides of a length equal to the diameter of the calculated aperture, and a cavity radius equal to the radius of the calculated aperture. Thermal absorbance of the receiver material was assumed to be 95%, matching the thermodynamic model.

[0183] Individual heliostats were assumed to be close to the size of the aperture at a width of 2.2 m and height of 2.2 m and made of a single panel. Heliostat size was kept constant between the E-field and no field models. Larger heliostats would increase spillage as the focus would become larger than the aperture area of the receiver. The mirror performance was defined with a reflectivity of 95% and a soiling factor of 95% 2.

[0184] The variable parameters for the solar field optimization for each model included minimum and maximum heliostat distance, and tower height. The flux map of the receiver produced by SolarPILOT was analyzed for the actual power into the aperture and concentration ratio using Equations 3 and 4, where the power, P, is calculated over the aperture area, A.

$$P = \int \text{flux } dA \quad \text{equation 3}$$

$$C = \frac{P}{\int dA} \quad \text{equation 4}$$

[0185] The workflow for the solar field sizing is outlined in FIG. 22, and used an initial design point power input in SolarPILOT of 10 MWt, tower height at 100 m, maximum heliostat distance relative to the tower height at 10 m, and minimum at 0.5 m. SolarPILOT was first used to build a field layout and simulate the performance at each hour of the year that had a DNI of 650 W/m². Then the field layout was optimized using SolarPILOT's internal optimization tool, reducing overall cost. Only the tower height, the maximum

heliostat distance, and the minimum heliostat distance were allowed to vary for the optimization. The flux plots for each performance simulation was exported to a MATLAB code that calculates the actual power into the aperture and concentration ratio, and plots the flux into total receiver target area (rectangle) and the flux into the aperture area (circle). The code also included the effect of heat re-radiation, calculated from the Stefan-Boltzmann law, as a loss in the flux. For the E-field model at 900° C. and the no E-field model at 1500° C., the re-radiation was determined to be 102.0 kW/m² and 532.3 kW/m² respectively. The power into the aperture was then checked to ensure at least 10 MWt in each performance case; if not, the design point power was increased by 0.1 MWt and the optimization cycle repeated. The steps were repeated until the power into the aperture was at least 10 MWt for each hour of the year that had a DNI of 650 W/m². SolarPILOT's internal optimization tool was then used to ensure the field layout was optimal for reducing overall cost. Only the tower height, mirror locations, the maximum heliostat distance, and the minimum heliostat distance were allowed to vary for the optimization.

[0186] A non-limiting summary of the final solar field parameters for both models is outlined in Table 5. The E-field model reduced the total heliostat mirror area by 26.6%, or 3,835 heliostats. SolarPILOT optimizes the number and position of heliostats in the field layout, calculating total land areas of 53.0 acres and 67.4 acres for the E-field model and the no field model respectively. Due to the lower temperature requirement of the E-field system, and accounting for re-radiation loss, achieving 10 MWt of power into the aperture allowed for smaller sizes of the field components including: tower height, aperture area, heliostat area, and necessary incident power.

TABLE 5

Summary of Solar Field Components for E-field model (900° C.) and No field model (1500° C.)

	E-Field Model	No Field Model
Tower Height (m)	60.2	74.6
Aperture Area (m ²)	4.22	4.78
Total Receiver Area (m ²)	8.3	9.0
Heliostat Count	10,582	14,417
Heliostat Total Area (m ²)	49,681	67,685
Required Design Power (MWt)	17.3	20.6

[0187] FIG. 23 displays, for both models, the flux into the aperture at key representative days over the year and times during those days. Four days were selected from different months throughout the year and three times of the day with varying sun positions. The DNI for the day at the given time is noted and the calculated power into the aperture. As expected, with an increase in DNI, the power also increases. Power absorbed into the aperture peaks in the summer month (July) and is lowest in the winter month (January). The center focal point for the heliostats varies throughout the day, and the year, with sun position changes, but remains within the defined aperture. Aperture positioning on the receiver was optimized considering the focal point behavior, and the center positioning was confirmed to produce the highest power and yearly performance for both models.

Plant Process Component Scaling

[0188] Process flow diagrams from the thermodynamic system level model were converted to an overall plant

process flow diagram, e.g., FIG. 24, for a plant to evaluate the necessary process units for the 10 MW scale. This process can be replicated to evaluate the necessary process units for additional scales by one of ordinary skill in the art using methods known in the art. Included are (1) a main reactor for the redox reaction, (2) a train of heat exchangers for cooling the reduction product stream, (3) a train of heat exchangers for cooling the oxidation product stream, (4) a separation unit for the CO and CO₂, (5) a separation and unit for the O₂ and N₂, (6) a compression unit for the separated O₂, and (7.1-7.4) fans for gas transport. The process units required are the same between both the E-field and no field models as the reaction and material components are identical. The difference between the two models in the plant process arises from the flow rates due to the higher efficiency of the isothermal reaction with the E-field.

[0189] Component flow rates, including packed reactor components, were calculated utilizing the design point of 10 MW, the reaction thermodynamic information calculated from experiment from Section 3.0 (efficiency, CO₂ ratio, and change in 8), an assumed cycle time of 10 minutes, and assumed density of ceria as the bulk 7.25 g/cm³. The no field, 1500° C., model was assumed to have a temperature swing of 600° C., down to 900° C., for oxidation given the temperature of the comparing E-field model. The E-field model included a quantity for the molten sodium sulfate assuming a 1:1 molar ratio for ceria to salt and a density of 2.069 g/cm³. For the N₂ sweep gas flow rate calculation, the partial pressure of O₂ for the reaction was retrieved from experiment at 100 Pa and ideal gases were assumed.

[0190] The solar thermal reactor is assumed to sit at the top of the tower with one of the circular bases oriented as the aperture for direct collection of the thermal power for the reaction as shown in FIG. 25. Reactor size was calculated assuming a packed cylinder with a circular base with at least the radius of the receiver cavity determined from the thermodynamic model and the solar field design to achieve 10 MWt of power into the aperture and average concentration ratio of 3,000. This is consistent with the solarPILOT results. Reactor volume was calculated from a combination of the required packing in the reactor and excess scaled for gas flow from the component flow rates. Higher efficiency, i.e. increased ceria quantity, and space for the molten salt gave a larger volume for the E-field reactor vessel. The volume of the E-field and no field reactors were calculated as 21 m³ and 4 m³ respectively. Reactor height and diameter for the E-field and no field models are 1.73 m×2.14 m and 0.87 m×1.23 m respectively.

[0191] For the heat exchanger units that cool the oxidation product stream, the incoming CO₂ feed stream at ambient conditions is integrated as the crossing cooling fluid to reduce final energy costs. The same integration was applied to the heat exchanger unit for the reduction product stream by crossing it with the incoming, ambient temperature, N₂ sweep gas stream. A series of countercurrent shell and tube gas-gas heat exchangers are sized to bring each product stream down to 30° C., with intermediate temperature points between exchangers chosen to decrease the need for costly high temperature construction materials. The overall heat transfer coefficient, which accounts for the heat transfer due to conduction and convection, was assumed to be 40 W/m²*K for the oxidation exchanger unit and 1000 W/m²*K for the reduction exchanger unit in both models. All exchanger units were calculated to be a series from one

to five individual heat exchangers, and the lowest cost option was selected as the final exchanger unit set-up for the product stream in each model. The E-field oxidation product unit includes two individual heat exchangers of effective areas of (1) 112 m² and (2) 26 m², and the reduction product unit includes two exchangers of effective areas of (1) 7915 m², (2) 2664 m². The no E-field oxidation product unit includes one individual heat exchanger of effective areas of (1) 49 m² and (2) 13 m², and the reduction product unit includes three exchangers of effective areas of (1) 2897 m², (2) 1217 m², (3) 854 m². Effective areas of heat transfer in the E-field model are higher due to the larger flow rates from the more efficient reaction.

[0192] Oxidation product separation (CO and CO₂) was assumed to be an amine-based system to get a CO product and to recycle the separated CO₂ back into the initial CO₂ feed stream. Data was collected from a water gas shift modeled production and economic analysis that included a monoethanolamine (MAE) solution and two columns connected in series for separation of CO and CO₂³. The data, processing 95,500 kmol/day, became the reference case that was scaled to our models for estimated capital costs. The process rate for the E-field and no field models are 5,380 kmol/day and 1,699 kmol/day respectively.

[0193] Reduction product separation (O₂ and N₂) was assumed to be a cryogenic separation unit, which includes compression of the oxygen byproduct to allow for sale credit in the later economic analysis. Data was obtained from a cryogenic air separation which excludes argon separation and produces pressurized gaseous oxygen product at 95% purity and 40 bar⁴. The data, processing 23,276 Nm³/h of O₂, became the reference case that was scaled to our models for estimated capital costs. The E-field model has 1,052 Nm³/h of O₂, and the no field model has 991 Nm³/h of O₂ separated and compressed respectively.

[0194] Fans were included in the plant models to keep gas moving in the process. At least two units exist in each process stream loop, giving five total units for each model. The units were sized by capacity needed given the process stream flow rates that were calculated from the reaction thermodynamics. Table 6 and Table 7 summarizes the process stream calculated flow rate from reaction thermodynamics and the calculated capacity the unit of fans need to move, given the gases behave ideally.

TABLE 6

E-field model fans summary			
Stream	Capacity (m ³ /h)	#Units in Stream	# Fans in Unit
Feed	3,414	1	1
Reduction	4,072	2	1
Oxidation	11,209	1	1

TABLE 7

No field model fans summary			
Stream	Capacity (m ³ /h)	#Units in Stream	# Fans in Unit
Feed	974	1	1
Reduction	3,475	2	1
Oxidation	1,490	1	1

Production Analysis

[0195] Yearly performance of the solar fields was determined by building a performance model based on SolarPILOT simulations. The data included 144 SolarPILOT simulation results, which were over 2 days each month of the year at 6 times of day for each field model type. The performance model inputs included the solar azimuth and zenith angles, as well as the DNI for that hour of the year from tmy2 data, and the output was the predicted power for each hour of the year. The performance model for each field is shown in FIG. 26, where the solid points are the SolarPILOT data, and the 'x' points are the predicted performance from multiple linear regression. The number of hours at the minimum required power of 10 MWt was calculated to be 2173 h/yr and 2149 h/yr for the E-field and no field models respectively.

[0196] The reaction was assumed to only occur during the hours of the year the plant is in operation. With cycling from reduction to oxidation in equal amounts of time, only half of the total reaction hours produce CO, while the other half produce O₂. The amount of CO produced per year was 2,574,621 kg for the E-field model and 931,617 kg for the no E-field plant. Annual production of CO for the E-field model was 63.8% higher than the no-field model. Productivity rates were fed into the cost analysis to account for CO quantity produced by each design when comparing the estimated costs of each.

Cost Analysis

[0197] Given the differences in operation temperatures between process streams and models, appropriate materials of construction were included in the equipment cost calculations. The materials used in the process, corresponding continuous operating temperature ranges, and cost multipliers are in Table 8. Different equipment types have different factors considering the general size and design needed for varying parts. The heat exchanger column assumes the shell and tubes are made of the same material.

TABLE 8

Material cost factors summary			
Material	Fans	Other Equipment	Heat Exchanger
Carbon Steel (CS)	1.00	1.00	1.00
Stainless Steel 304 (SS)	1.70	2.70	2.73
Inconel 600/601 (IN)	3.33	3.60	3.73

[0198] Although individual costs are shown as a comparison between the two designs, final determination of cost per CO produced accounts for the productivity calculated above where the E-field was 63.8% higher. Therefore, individual costs for the E-field model are not disregarded if larger than the no field model given that final cost is scaled to the much higher productivity of the e-field.

[0199] The optimized solar field designs had four components to price: solar tower, solar receiver, heliostats, and land. For each component and both paradigms, the basis cost and final cost are presented in Table 9. Site improvements were considered as preparation of the area the heliostats occupy. The E-field model solar field was less expensive by \$1,313,271, or 24.4%.

TABLE 9

Summary of solar field components			
Solar Field Component	Cost Basis	E-Field STCS Costs (2016 USD)	No E-Field STCS Costs (2016 USD)
Tower	\$26,582*(H _{tower}) ^{0.95} [B. Gorman] 2400/m ² ⁵	783,541	959,877
Receiver	50/m ² ⁶	20,256	22,944
Heliostats	10% ^{2, 6}	2,484,020	3,384,245
Site Improvements	10,000/acre ⁶	248,402	338,425
Land		530,000	674,000
Total		4,066,219	5,379,491

[0200] The solar thermal reactor was assumed to have a basic design of a cylindrical vessel with insulating layers based on storage units used for high temperature hot storage⁷. One circular base of the reactor is assumed to be the receiver aperture as described above. Further design and materials consideration would need to be researched and tested for integrity in the novel E-field process. Reactors for each model were assumed to have a volume available for active materials and gas. The volume of each insulating layer scaled with the volume of space in the reactor needed with fixed layer thicknesses of 0.025 m of ceramic, 0.115 m of firebrick, 0.0575 m of Kaowool insulation, and 0.005 m of metallic shell. Due to the electric field, a compatibility layer on the interior of the reactor to prevent corrosion from the molten salt was necessary. The compatibility layer was assumed to be a zirconium-based paint that was applied and cured in four layers (thickness 0.004 m), as was done in the laboratory experiments of Sections 1 and 2. The metallic outer shell of the E-field model was stainless-steel, and the no E-field model was Inconel due to temperature considerations. FIG. 27 shows how the layers are proposed to be integrated relation to the reactor interior space. The costs of the reactor for the E-field and no E-field plants were determined to be \$837,948 and \$386,791. Due to the expected difficulty of design and construction for a solar thermal reactor, a complexity factor of 2 was multiplied to the calculated cost of each model's reactor. Final costs for the solar thermal reactors were \$1,704,984 and \$761,096 for the E-field and no E-field models respectively. The final purchase cost of the E-field reactor is higher due to the larger volume needed considering the reaction efficiency.

[0201] All heat exchangers in the plant process were assumed to be gas-gas, shell and tube exchangers and were costed using the calculated effective area for heat transfer, the materials of construction factors in Table 8, and the cost curves presented in the "Process Equipment Cost Estimation" report for performing cost estimates for proposed systems by Loh, H. P. et al.⁸. A summary of each heat exchanger unit in both models, including effective area, material of construction, and purchase cost, are presented in Table 10 and Table 11. The cost and material selections for the heat exchangers have been reviewed by Joshua Neveu, a licensed Professional Engineering (P.E.) of the Southwest Research Institute who is an expert in heat exchanger design and manufacturing.

[0202] The E-field model has a larger cost for heat exchangers than the no E-field plant due to the higher flow rates from higher productivity requiring larger effective areas for heat transfer. For Unit 1 in the E-field system, two

exchangers were chosen in series as it was cheaper with one low-cost material exchanger and one with higher cost material, than one larger exchanger made with the higher cost material. For Unit 1 in the no E-field model, the same was found to be true. The no E-field model has a higher reduction temperature at 1500°C., and thus requires materials that can withstand the higher temperature for construction in the reduction stream (Unit 2). The difference in Unit 1 cost between the two models was \$23,322 (23.8%) and the difference between Unit 2 cost was \$140,163 (5.2%). Although the E-field model heat exchanger cost was larger, it is only by 5.8% (\$163,485).

TABLE 10

E-field model heat exchanger units cost summary				
	Heat Exchanger	Material	Area (m ²)	Purchase Cost (2017 USD)
Heat Exchanger Unit 1	HX 1.1	CS	112	\$35,871
	HX 1.2	SS	26	\$53,164
Heat Exchanger Unit 2	Unit 1 Subtotal			\$89,035
	HX 2.1	CS	7915	\$1,523,591
	HX 2.2	SS	2664	\$1,426,248
	Unit 2 Subtotal			\$2,949,839
E-Field Total				\$3,038,874

TABLE 11

No field model heat exchanger units cost summary				
	Heat Exchanger	Material	Area (m ²)	Purchase Cost (2017 USD)
Heat Exchanger Unit 1	HX 1.1	CS	49	\$23,859
	HX 1.2	SS	13	\$46,398
Heat Exchanger Unit 2	Unit 1 Subtotal			\$70,257
	HX 2.1	CS	2897	\$566,859
	HX 2.2	SS	1217	\$673,082
	HX 2.3	IN	854	\$661,481
Unit 2 Subtotal				\$1,901,422
No E-Field Total				\$1,971,679

[0203] The cost for the CO separation from CO₂ was based on the reference case where a feed of 95,444 kmol/day had a capital cost of \$7,374,012. For the E-field CO separation unit, cost was found to be \$415,701, and the no E-field unit was \$131,283. The cost increase of \$284,417 (68.4%) for the E-field arises from the much higher flow rates in the model from the higher productivity.

[0204] For the cost of the O₂ separation from N₂ and subsequently compression, a cryogenic air separation unit was chosen as a reference case where 23,276 m³/h of O₂ is separated and compressed at a capital cost of \$18,000,000. Scaling for the O₂ amounts needed processed in the two models, the E-field unit cost was found to be \$813,542 and the no E-field unit cost was \$766,369. The E-field cost more by 5.8%, due to the higher O₂ production in the oxidation reaction. It was noted that cryogenic air separation has less economic value at smaller scales than large scales, so a

multiplier of 1.5 to the cost for each model was assumed. The final cost for the E-field O₂ separation unit was \$1,220,313 and the no E-field model O₂ separation unit was \$1,149,553. O₂ product from the process was assumed to be compressed, based on the reference case, and added as a profitable byproduct in the final economic analysis. We note that alternative plant designs for O₂ separation, such as vacuum pumping or a secondary thermochemical cycle, may decrease the overall plant costs, and thus increase the value proposition. However, at this point the use of well known unit operations provides a means for direct, even-handed, comparison of the two technologies of interest.

[0205] The plant design accounted for two units of fans per process stream loop. Process equipment for gas movement out of the air separation unit was assumed to be covered by the cost of the separation unit for the outputs of sweep N₂ and compressed O₂. All fans in the process are assumed to be gas centrifugal fans and cost estimated from the capacity needed for the flow rates and the curves for cost estimation⁸. Materials of construction of the fans were considered based on the process stream temperatures and the factors in Table 8 were used in scaling the purchase cost. Purchase costs of the fans are presented in Table 12 and Table 13 for the E-field and no E-field models, respectively. The E-field fan cost was \$43,216 more, or 53.4%, due to the larger capacities needed.

TABLE 12

E-field model fans summary				
Stream	Capacity (m ³ /h)	# Fans in Unit	Material of Construction	Purchase Cost (2017 USD)
	Conventional (1500° C.)			\$24,719
Feed (7.1)	974	1	CS	\$2,086
Oxidation product (7.4)	3,475	1	CS	\$7,019
Reduction Product (7.3)	1,490	1	IN	\$10,336
Reduction Product (7.2)	1,490	1	SS	\$5,277

TABLE 13

No field model fans summary				
	E-field (900° C.)			
Feed (7.1)	3,414	1	CS	\$6,899
Oxidation Product (7.4)	11,209	1	CS	\$22,274
Reduction Product (7.3)	4,072	1	SS	\$13,934
Reduction Product (7.2)	4,072	1	CS	\$8,197

[0206] Financial analysis requires the total installed costs for equipment, which are found by multiplying the purchase cost by an installation amount. Installation includes percentages of the purchase cost for setting (20%), electrical (8.4%), and piping (6%) as needed for each equipment type. Tables presented for cost estimation⁸ were used for determining installed costs for the appropriate common equipment in each model. The solar field components, separation units, and custom solar thermal reactors had installation costs determined from referencing works on solar systems [B. Gorman, V. Budama]. Installation costs for each model are summarized in Table 14.

TABLE 14

Summary installed equipment costs for both models		
Operational Unit	Conventional Model Installed Cost	E-field Model Installed Costs
Tower	1,232,482	1,006,067
Receiver	27,533	24,307
Heliostats	4,683,795	3,437,884
Land	674,000	530,000
Reactor	913,315	2,045,980
Heat Exchanger	2,531,636	3,901,915
Fans	33,222	68,952
Separations	1,721,419	2,198,744
Active Material	676,099	3,469,236
Total	12,511,034	16,722,959

[0207] Other costs for the models include the reaction materials. For the E-field, materials include the ceria, sodium sulfate, and an electrode assembly. The no E-field plant comparatively, has only the ceria cost. Table 15 summarizes the active material costs for the reactors in each model. All active materials for the reaction were assumed to not have any installation cost. The ceria and molten salt were assumed to have a replacement rate of 10% every year⁹. The electrode assembly was given an assumed overall purchase cost that includes the materials and set-up.

TABLE 15

Reaction active materials cost summary					
E-Field Model				Purchase	
Material	Reference Cost (2023 USD)	Quantity (kg/cycle)	Purchase Cost (2017 USD)	Quantity (kg/cycle)	Cost (2017 USD)
Ceria	\$30/1 kg	34,669	1,040,066	22,537	676,099
Sodium Sulfate	\$15/1 kg	28,611	429,170	—	—
Electrode Assembly	—	—	2,000,000	—	—
Total		6,781,337	Total		676,099

[0208] The total capital costs were \$19,701,319 and \$14,739,249 for the E-field and no E-field plants respectively, and the breakdown of the costs are shown in FIG. 28. The higher initial purchase costs of the equipment as well as the need for the molten salt and electrode assembly in the reaction materials in the E-field mode results in a higher capital cost. The 63.8% higher production of CO was not taken into consideration in this capital cost breakdown.

[0209] The leveled cost of CO for each model was calculated using equations presented by Brandon Gorman and Ellen Stechel [B. Gorman]. Modifications to the equations were made to encompass the cost of electricity in the E-field model, and the revenue coming from selling the byproduct O₂. The modified equations are presented as Equations 5-12: total installed component cost (3), controls cost (4), balance of plant cost (5), capital expenditure (6), operation and maintenance cost (7), annual capital expenditure (8), total annualized cost (9), and final leveled cost of CO (10). Individual installed costs and assumptions can be found in the above tables. All plant operation was

assumed to be during operable on-sun; thus, no operating electricity was required, except for the small amount needed for 2V E-field generation during reduction. The base cost for the electricity and O₂ byproduct revenue were taken from DOE H2A worksheet defaults from the 2017 reference case. Financial factors used in the cost equations are summarized in Table 16.

$$C_{comp} = \text{Equation 5}$$

$$C_{tow} + C_{rec} + C_{sol\ field} + C_{STR} + C_{HX} + C_{Seps} + C_{act\ mat} + c_{elec\ asm}$$

$$C_{ctr} = C_{comp} * f_{ctr} \quad \text{Equation 6}$$

$$C_{BoP} = (C_{comp} + C_{ctr}) * f_{BoP} \quad \text{Equation 7}$$

$$C_{CapEx} = (C_{comp} + C_{ctr} + C_{BoP}) * (1 + f_{cont}) \quad \text{Equation 8}$$

$$C_{O&M} = (C_{comp} + C_{ctr} + C_{BoP}) * f_{O&M} \quad \text{Equation 9}$$

$$C_{CapEx,yr} = (C_{CapEx} * f_{crf}) + C_{feed} + C_{elect} + (C_{act\ mat} * f_{rep}) \quad \text{Equation 10}$$

$$C_{tow} = C_{CapEx,yr} + C_{O&M} \quad \text{Equation 11}$$

$$C_{CO,kg} = \frac{C_{tow} - R_{O_2}}{P_{CO,kg}} \quad \text{Equation 12}$$

TABLE 16

Financial factors summary for leveled cost of CO calculation		
Parameter	Units	Value
Controls factor (f _{ctr})	[%]	5
Balance of plant factor (f _{BoP})	[%]	2
Contingency factor (f _{cont})	[%]	10
Operation and maintenance factor (f _{O&M})	[%/yr]	1
Capital recovery factor (f _{crf})	[%/yr]	8
Active material replacement rate (f _{rep})	[%/yr]	10

[0210] There was full consistency in selections between both models in how calculations were completed, and the references used for final values. Though there is expected uncertainty in the final leveled values, the comparison between the two models was accurate. The final leveled cost of CO for each model was \$0.75 per kg CO and \$1.49 per kg CO for the E-field and no E-field respectively. The E-field model provides a leveled cost of CO that is 66.4% lower than the traditional no field model.

Outline of Non-Limiting, Exemplary Scale-Up Project and Costs (Section 4.2)

[0211] Summary: This section outlines a non-limiting, exemplary path of scaling-up and associated costs. Based on the TEA and thermodynamic model from Sections 4.1 and 3.2, waterfall and fishbone analyses outline non-limiting, exemplary scale-up project steps.

[0212] Non-limiting, exciting aspects: The E-field enhanced STCS plant requires far fewer advancements to achieve DOE cost targets for CO production. An improvement can be heat storage enabling expanded operation time.

Results and Analysis

[0213] The leveled costs of CO calculated in Section 4.1, \$0.75 per kg CO for the E-field model and \$1.49 per kg CO for the no field model. A fishbone diagram was created to evaluate parameters that can affect the different categories

for cost adjustments. The diagram, which is the same for both models, is shown in FIG. 29, where the colors show what category adjustment to each parameter is predicted to affect: annual operating capacity (red), capital investment (blue), design production capacity (green).

[0214] A sensitivity analysis was done for each system model detailing how a 20% change to select parameters from the fishbone analysis can affect the cost to produce one kg of CO. The charts in FIG. 30 provide quantitative insight into how the design decisions and assumptions affect the final leveled cost for further consideration. The top contributing factors to the cost for the E-field plant were the financial capital recovery factor, the number of operational hours in the year, heliostat cost, and the cost of the active materials, ceria and salt. For the no E-field plant, the largest contributing factors were the financial capital recovery factor, operational hours per year, heliostat cost, and heat exchanger cost. The difference between the two models arises from the high efficiency of the E-field model that requires more active material, including molten salt, which has a larger effect on overall cost than the no E-field model.

[0215] With the information from the initial analysis there are numerous paths that can be taken to achieve the target cost. A waterfall chart was created as an example of one path towards demonstration of \$0.21 per kg CO for the E-field plant, as shown in FIG. 31 panel (a). The waterfall analysis includes the no field model with equivalent changes to each parameter (FIG. 31 panel (b)), demonstrating that a significant cost difference (68%) between the two models remains. Overall, fewer advancements to the E-field plant will be needed to achieve the target cost compared to the conventional thermal only plant, re-enforcing it as the most efficient and cost-effective option for CO₂ splitting. In order to achieve the STCS targets of DOE, the use of the E-field system is strongly suggested. Further, inclusion of heat storage which would enable higher operating capacities should be sought

Non-Limiting Conclusions

[0216] Described herein for first time is the use of an E-field in substantially lowering the required reduction temperature for solar thermochemical carbon dioxide splitting to <1000° C. which cuts the expected price for solar CO in half. Through careful selection, Na₂SO₄ was identified as a promising molten salt for constructing the electronic double layer. Using this molten salt, E-field enhanced CO₂ splitting experiments produced 397±6 μmol CO/g CeO₂ with an O₂ faradaic efficiency of 168±5% at 900° C. and 4V at a 95% confidence interval. Thermodynamic models predicted an increase in solar to CO efficiencies from ~0% in thermal only paradigm to ~40% in the E-field operation under reasonable system assumptions. This high solar efficiency held when the experimentally measured production was used in a thermodynamic plant model. Technoeconomic models indicate the use of the E-field can decrease CO production costs by ~50%, from \$1.49/kg CO to \$0.75/kg CO. The largest improvements which can be considered are to further lower the leveled cost of CO is an expansion of percent of operating time. Overall, this project successfully demonstrated the use of E-field enhanced solar thermochemical CO production through an electronic double layer effect at 900° C. and represents a significant advance in solar fuels production.

Recommendations

[0217] Based on the success of this project, without wishing to be bound by theory, we can improve costs by the following: Firstly, detailed reactor designs can be considered which maximize CO₂/CeO₂ contacting to increase CO production capacity and rates. This can include full reactor modeling including mass and heat flow as well as E-field effects. Secondly, means to integrate solar energy storage can be addressed, this is simplified in the current concept as only 900° C. are required, which are well within current heat storage capacities. Such an integration can increase the daily and seasonal operating capacity beyond times of high solar irradiance. Thirdly, because lower temperatures are possible, new avenues of reactor placement can be considered, such as ground based platforms, which can lower operating costs, however detailed thermodynamic and cost analysis of the trade-offs can be considered. Fourthly, long term stability test can be addressed. Overall, the results of this project position the E-field enhanced solar thermochemical CO₂ splitting technology in a great position for advancement.

REFERENCES CITED HEREIN

- [0218]** 1. Sengupta, M.; Xie, Y.; Lopez, A.; Habte, A.; Maclaurin, G.; Shelby, J., The national solar radiation data base (NSRDB). Renewable and sustainable energy reviews 2018, 89, 51-60.
- [0219]** 2. Ma, Z.; Davenport, P.; Saur, G., System and techno-economic analysis of solar thermochemical hydrogen production. Renewable Energy 2022, 190, 294-308.
- [0220]** 3. Kim, J.; Henao, C. A.; Johnson, T. A.; Dedrick, D. E.; Miller, J. E.; Stechel, E. B.; Maravelias, C. T., Methanol production from CO₂ using solar-thermal energy: process development and techno-economic analysis. Energy & Environmental Science 2011, 4 (9), 3122-3132.
- [0221]** 4. Ebrahimi, A.; Meratizaman, M.; Reyhani, H. A.; Pourali, O.; Amidpour, M., Energetic, exergetic and economic assessment of oxygen production from two columns cryogenic air separation unit. Energy 2015, 90, 1298-1316.
- [0222]** 5. Budama, V. K.; Johnson, N. G.; Ermanoski, I.; Stechel, E. B., Techno-economic analysis of thermochemical water-splitting system for Co-production of hydrogen and electricity. International Journal of Hydrogen Energy 2021, 46 (2), 1656-1670.
- [0223]** 6. US Department of Energy SunShot Vision Study; February 2012, 2012; pp 66-96.
- [0224]** 7. El-Leathy, A.; Jeter, S.; Al-Ansary, H.; Abdel-Khalik, S.; Roop, J.; Golob, M.; Danish, S.; Alrished, A.; Djajadiwinata, E.; Al-Suhaimani, Z., Thermal performance evaluation of two thermal energy storage tank design concepts for use with a solid particle receiver-based solar power tower. Energies 2014, 7 (12), 8201-8216.
- [0225]** 8. Loh, H.; Lyons, J.; White, C. W. Process equipment cost estimation, final report; National Energy Technology Lab. (NETL), Morgantown, WV (United States): 2002.
- [0226]** 9. Gorman, B. T.; Lanzarini-Lopes, M.; Johnson, N. G.; Miller, J. E.; Stechel, E. B., Techno-economic analysis of a concentrating solar power plant using redox-active metal oxides as heat transfer fluid and storage media. Frontiers in Energy Research 2021, 9, 734288.

TEA Calculation Details

- [0227]** Summary of component final design values for each model

Installed Cost			
		1500 C No Field	900 C E-Field
Solar Field			
Tower	height [m] area (8.3, 9)	\$1,232,482.21	\$1,006,067.20
Receiver	[m ²]	\$27,532.80	\$24,307.20
Heliostats	area [m ²]	\$4,683,795.08	\$3,437,883.68
Land	area [acres]	\$674,000.00	\$530,000.00
Plant Process Equipment			
Solar Thermal Reactor HX Unit 1	volume [m ³]	\$913,314.92	\$2,045,980.43
HX 1.1	area [m ²]	\$30,635.39	\$46,058.26
HX 1.2	area [m ²]	\$59,574.95	\$68,263.16
HX Unit 2			
HX 2.1	area [m ²]	\$727,846.98	\$1,956,290.72
HX 2.2	area [m ²]	\$864,237.42	\$1,831,302.70
HX 2.3	area [m ²]	\$849,341.07	\$0.00
Separation Unit 1 (CO/CO ₂)	[kmol co ₂ /day]	\$176,419.28	\$558,643.73
Separation Unit 2 (O ₂ /N ₂)	[Nm ³ o ₂ /h] capacity	\$1,544,999.48	\$1,640,100.36
Fan 1	[m ³ /h] capacity	\$2,803.94	\$9,272.15
Fan 2	[m ³ /h] capacity	\$9,433.86	\$29,935.96
Fan 3	[m ³ /h] capacity	\$13,892.13	\$11,016.45
Fan 4	[m ³ /h] capacity	\$7,092.08	\$18,727.96
Materials			
Ceria (particles)	mass [kg/yr]	\$676,110.00	\$1,040,070.00
Sodium Sulfate	mass [kg/yr]	\$0.00	\$429,165.00
Electrode Assembly	number []	\$0.00	\$2,000,000.00
CO ₂ Feedstock	mass [kg/yr]	\$24,152.35	\$66,747.56
O ₂ Byproduct	mass [kg/yr]	\$15,166.62	\$41,914.56
Electrical for 2V	power [kW]	\$0.00	\$36.51

- [0228]** Summary of the equations for determining the final installed cost of the models' components

Tower	$C_{tower} = C_{b,tower} H_{tower}^{flower} * (1 + M_s + M_e)$
Receiver	$C_{rec} = C_{b,rec} A_{rec} * M_{rec} * (1 + M_s)$
Heliostats	$C_{helio} = C_{b,helio} A_{helio} * (1 + f_{site\ prep}) * (1 + M_s)$
Land	$C_{land} = C_{b,land} A_{land}$
STR	$(\sum_i^4 V_{STR,i} - V_{STR,i-1}) * C_{in,mat,i} * M_{STR} * (1 + M_s)$
HX	$C_{HX} = (C_{a,HX} A_{HX} + C_{b,HX}) * MOC * (1 + M_s + M_e)$
Sep. CO/CO ₂	$C_{sep,CO_2} = C_{b,sep,CO_2} M_{CO_2} * (1 + M_s + M_e + M_p)$
Sep. O ₂ /N ₂	$C_{sep,O_2} = C_{b,sep,O_2} V_{O_2} * M_{sep} * (1 + M_s + M_e + M_p)$
Fans	$C_{fan} = (C_{a,fan} V + C_{b,fan}) * (1 + M_s + M_e + M_p)$
Electricity	$C_{elec} = \left(\frac{I * V}{1000} \right) * \left(\frac{t_{op,hr}}{2} \right) * C_{b,elec}$

- [0229]** Summary of the values for the factors used in component costing equations

	Units	Value
Component Constants		
$C_{b,tow}$	[\$/m]	26582
f_{low}		0.95
$C_{b,rec}$	[\$/m ²]	2400
M_{rec}		2
$C_{b,helio}$	[\$/m ²]	50
$f_{siteprep}$	[%]	10
$C_{b,land}$	[\$/acre]	10000
d_{STR}	[m]	2.467
l_{STR}	[m]	0.8368
t_{STR1}	[m]	0.004
t_{STR2}	[m]	0.025
t_{STR3}	[m]	0.115
t_{STR4}	[m]	0.0575
t_{STR5}	[m]	0.005
M_{STR}		2
$C_{b,HX}$	[\$/m ²]	14517
$C_{a,HX}$	[\$/m ²]	190.66
C_{ref,CO_2}	[\$/kmol/day]	77.26
C_{ref,O_2}	[\$/Nm ³ /h]	773.33
$M_{sep,air}$		1.5
$C_{b,fan}$	[\$/m ³ /h]	165.15
$C_{a,fan}$	[\$/m ³ /h]	1.9724
Material of Construction Factors (fan, other, heat exchanger)		
Carbon steel		1, 1, 1
Stainless steel		1.7, 2.7, 2.73
Inconel		3.33, 3.6, 3.73
Installation Multipliers		
M_s	[%]	20
M_e	[%]	8.4
M_p	[%]	6.0

EQUIVALENTS

[0230] Those skilled in the art will recognize, or be able to ascertain, using no more than routine experimentation, numerous equivalents to the specific substances and procedures described herein. Such equivalents are considered to be within the scope of this invention and are covered by the following claims.

What is claimed is:

1. A method of performing thermochemical gas splitting at a reduced operating temperature, the method comprising: connecting a metal oxide (M_yO_x) to a first electrode connected to a power source; placing a second electrode connected to the power source in an electrolyte; submerging the M_yO_x connected to the first electrode in the electrolyte and subjecting the M_yO_x and electrolyte to an increased temperature; applying a potential to the M_yO_x and electrolyte, thereby eliciting an electronic double layer at the M_yO_x /electrolyte interface and reducing the (M_yO_x) to form a non-stoichiometric oxide ($M_yO_{x-\delta}$) or a stoichiometric metal oxide (M_yO_{x-1}); and oxidizing the $M_yO_{x-\delta}$ or the M_yO_{x-1} with an oxidizing agent to regenerate the M_yO_x , thereby generating a gas product, heat, or a combination thereof.

2. The method of claim 1, wherein submerging comprises submerging about 25% to about 75% of the metal oxide.

3. The method of claim 1, wherein the electrolyte is selected from an ionic liquid, a molten salt, or a combination thereof.

4. The method of claim 3, wherein the ionic liquid or molten salt is selected from sodium, potassium, lithium, calcium, and magnesium carbonates, chlorides, sulphates, phosphates, or a mixture thereof.

5. The method of claim 4, wherein the molten salt is selected from NaCl, KCl, MgCl₂, CaCl₂, LiCl, Na₂SO₄, K₂SO₄, Li₂SO₄, CaCO₃, Li₂CO₃, K₂CO₃, or a combination thereof.

6. The method of claim 1, wherein the metal oxide (M_yO_x) is selected from ceria (CeO₂), SrLaMnO₃, BaFeO₃, Fe₃O₄, FeAl₂O₄, CoFe₂O₄, CoFeAl₂O₄, perovskites, ceria derivatives, spinel ferrites, or a combination thereof.

7. The method of claim 1, wherein the increased temperature is selected from a temperature of about 1375° C., about 1350° C., about 1325° C., about 1300° C., about 1275° C., about 1250° C., about 1225° C., about 1200° C., about 1175° C., about 1150° C., about 1125° C., about 1100° C., about 1075° C., about 1050° C., about 1025° C., about 1000° C., about 975° C., about 950° C., about 925° C., about 900° C., about 875° C., about 850° C., about 825° C., about 800° C., about 775° C., about 750° C., about 725° C., about 700° C., about 675° C., about 650° C., about 625° C., about 600° C., about 575° C., about 550° C., about 525° C., about 500° C., or below about 500° C.

8. The method of claim 1, wherein the potential is selected from less than about 0.25V, about 0.25V, about 0.5V, about 0.75V, about 1.0V, about 1.25V, about 1.50V, about 1.75V, about 2.0V, about 2.25V, about 2.5V, about 2.75V, about 3.0V, about 3.5V, about 4.0V, about 4.25V, about 4.5V, about 4.75V, about 5.0V, about 5.25V, about 5.5V, about 5.75V, about 6.0V, or greater than about 6.0V.

9. The method of claim 1, wherein the gas product is selected from H₂, CO, or a combination thereof.

10. The method of claim 1, wherein the method is performed at a partial pressure of about 1 Pa, about 10 Pa, about 50 Pa, about 100 Pa, about 200 Pa, about 250 Pa, about 300 Pa, about 350 Pa, about 400 Pa, about 450 Pa, about 500 Pa, about 550 Pa, about 600 Pa, about 650 Pa, about 700 Pa, about 750 Pa, about 800 Pa, about 850 Pa, about 900 Pa, about 950 Pa, about 1000 Pa, or greater than about 1000 Pa.

11. The method of claim 1, wherein the method has an O₂ Faradaic efficiency of about 100%, about 125%, about 150%, about 175%, about 200%, or greater than about 200%.

12. The method of claim 1, wherein the electronic double layer produces an E-field of about 5 V/nm or greater than 5 V/nm.

13. The method of claim 9, wherein the method has a gas production capability of about 100 to about 500 μmol gas/g metal oxide.

14. An electric field enhanced CO₂ splitting system comprising:

a reactor comprising a metal oxide, a molten salt or ionic liquid, and an electrode; and a heat source.

15. The system of claim 14, wherein the system further comprises a reduction heat exchanger unit, an oxidation heat exchanger unit, a reduction production separation unit, an oxidation production separation unit, heat storage tanks, a solar furnace, a turbine, one or more blowers, or a combination thereof.

16. The method of claim **14**, wherein the ionic liquid or molten salt comprises sodium, potassium, lithium, calcium, and magnesium carbonates, chlorides, sulphates, phosphates, or a mixture thereof.

17. The method of claim **14**, wherein the molten salt comprises NaCl, KCl, MgCl₂, CaCl₂, LiCl, Na₂SO₄, Li₂SO₄, K₂SO₄, CaCO₃, Li₂CO₃, K₂CO₃, or a combination thereof.

18. The method of claim **14**, wherein the metal oxide (M_xO_y) comprises ceria (CeO₂), SrLaMnO₃, BaFeO₃, Fe₃O₄, FeAl₂O₄, CoFe₂O₄, CoFeAl₂O₄, perovskites, ceria derivatives, spinel ferrites, or a combination thereof.

19. The system of claim **14**, wherein the system is an industrial system further comprising a reduction production separation unit, an oxidation production separation unit, heat storage tanks, a solar furnace, a turbine, one or more blowers, or a combination thereof.

20. The system of claim **14**, wherein the industrial system comprises the process flow diagram of FIG. **24**.

* * * * *